8-14-2000

Simulation and Analysis of Wing Rock Physics for a Generic Fighter Model with Three Degrees-of-Freedom

Ahmed Saad

SIMULATION AND ANALYSIS OF WING ROCK PHYSICS FOR A GENERIC FIGHTER MODEL WITH THREE DEGREES-OF-FREEDOM

DISSERTATION

Ahmed A. Saad, Major, Egyptian Air Force
AFIT/DS/ENY/00-01

DEPARTMENT OF THE AIR FORCE
AIR UNIVERSITY

AIR FORCE INSTITUTE OF TECHNOLOGY

Wright-Patterson Air Force Base, Dayton, Ohio

Disclaimer

The views expressed in this dissertation are those of the author and do not reflect the official policy or position of the Department of Defense, U. S. Government, or the Egyptian Ministry of Defense.

AFIT/DS/ENY/00-01

SIMULATION AND ANALYSIS OF WING ROCK PHYSICS FOR A GENERIC FIGHTER MODEL WITH THREE DEGREES-OF-FREEDOM

DISSERTATION

Presented to the Faculty

Graduate School of Engineering and Management

Air Force Institute of Technology

Air University

Air Education and Training Command

In Partial Fulfillment of the Requirements for the

Degree of Doctor of Philosophy

Ahmed A. Saad, B.S., M.S.

Major, Egyptian Air Force

July 2000

AFIT/DS/ENY/00-01

SIMULATION AND ANALYSIS OF WING ROCK PHYSICS FOR A GENERIC FIGHTER MODEL WITH THREE DEGREES-OF-FREEDOM

Ahmed A. Saad, B.S., M.S.
Major, Egyptian Air Force

Approved:

Brad S. Liebst (Chairman) — 7 Aug 00 — Date

Miguel R. Visbal (Member) — 7 Aug 00 — Date

Philip S. Beran (Member) — 7 Aug 00 — Date

William P. Baker (Member) — 7 Aug 00 — Date

Accepted:

Robert A. Calico, Jr. (Dean) — 14 Aug 00 — Date
Dean, Graduate School of Engineering and Management

Acknowledgments

All thanks are due to God, who has bestowed upon me a valuable opportunity that I have dreamed of for so long.

The project presented in this dissertation is the result of many contributions that I wish to acknowledge. I owe the greatest debt of gratitude to my advisor, Dr. Brad S. Liebst, for his continuous guidance, support, and motivation during the entire course of this project. I thank my committee members, Dr. Baker, Dr. Beran, and Dr. Visbal, for the time and concern they gave during all phases of this research. I also thank Dr. Visbal, from the Air Force Research Laboratories (*AFRL*), for providing the flow solver code (*fdl3di*), which has been utilized in this project. Special thanks goes to Dr. Ray Gordnier from the *AFRL*, who patiently guided me throughout the Computational Fluid Dynamics (*CFD*) course work in this project. I also thank Dr. Sam Naboulsi from *AFIT*, who helped me running the *PEGSUS* software, and getting started with the *UNIX* commands. I would like to express my appreciation to Mr. Dave Doak, system administrator at *AFIT*, who kindly provided the system support at many critical times.

I would like to express my appreciation and thanks for the Ohio Supercomputer Center (*OSC*) Columbus, Ohio for providing the CPU-time for this research on the *CRAY-T94*, grant number *PIS198*.

I also thank the National Aeronautics and Space Administration (*NASA*), for providing a free copy of the *CFD* post-processing software *FAST*.

Lastly, and mostly important, I thank my wife for her love and encouragement during these challenging years at *AFIT*.

Table of Contents

Page

List of Figures

Figure Page

List of Tables

List of Symbols

English Alphabet

$\vec{M}$	Total aerodynamic moment vector.
$\vec{a}$	Total acceleration vector.
$\vec{F}$	Total aerodynamic force vector.
$\vec{U}$	Velocity vector.
AR	Aspect Ratio.
C_l	Body-fixed rolling moment coefficient.
C_r	Wing root chord-length.
e	Specific internal energy (per unit mass).
F_x, F_y, *and* F_z	Aerodynamic force components in the X, Y, and Z directions respectively.
g	Gravity acceleration.
$\hat{i}$, $\hat{j}$, *and* $\hat{k}$	Unit normal vectors in the X, Y, *and* Z directions respectively.
I, J, *and* K	Computational coordinates indices in the ξ, η, and ζ directions respectively.
I_x	Moment of inertia about the body-fixed X-axis.
J	Jacobian of the coordinate transformation.
L_b	Body-fixed rolling moment.
M	Mach number.
m	Mass of aircraft.
M_x, M_y, *and* M_z	Aerodynamic moment components about the center of gravity in the X, Y, and Z directions respectively.
p	Body-fixed rolling rate.
P	Static pressure.
$\vec{r}$	Position vector in the inertial frame-of-reference.
Re	Reynolds number.

S	Arc length.
T	Static temperature.
t	Time.
u, v, *and* w	Velocity components in the X, Y, and Z directions respectively.
X, Y, *and* Z	Cartesian coordinates in the inertial frame-of-reference.

Greek Alphabet

α	Angle of attack.
ρ	Air density.
φ	Roll angle.
ξ, η, *and* ζ	Computational coordinates in the axial, normal, and wrap-around directions respectively.
$\vec{\omega}$	Angular acceleration vector.
$\vec{\tau}$	Stress tensor.
β	Sideslip angle.
σ	Surface area.
μs	Micro-seconds.
Δt	Time step.

Subscripts

o	Denotes wings-leveled position.
∞	Denotes free-stream conditions.
b	Denotes body.
cg	Denotes center of gravity.
n	Denotes normal.

Second subscript level denotes partial derivative.

Example:

$$C_{l_\beta} \equiv \frac{\partial C_l}{\partial \beta}$$

Superscripts

.	Time derivative.
o	Initial conditions (time level $n = 0$).
n	Time level (index).
*	Denotes nondimensional variables.

Abbreviations

AFIT	Air Force Institute of Technology.
AFRL	Air Force Research Laboratories.
AGARD	Advisory Group for Aerospace Research & Development.
AOA	Angle of Attack.
B. Cs.	Boundary Conditions.
CFD	Computational Fluid Dynamics.
c.g.	Center of Gravity.
CPU	Central Processing Unit.
DoF	Degree(s)-of-Freedom.
EPDE	Elliptic Partial Differential Equation(s).
GFLOPS	Giga Floating Point Operations per Second.
L.E.	Leading Edge.
LaRC	Langley Research Center.
MHz	Mega Hertz.
NASA	National Aeronautics and Space Administration.

ODE	Ordinary Differential Equation.
OSC	Ohio Supercomputer Center.
PIO	Pilot-Induced Oscillations.
RANS	Reynolds-Averaged Navier-Stokes.
RCDMT	Radio-Controlled Drop-Model Technique.

Abstract

Modern fighter designs have been associated with lateral self-excited oscillations known as "Wing Rock". Simulations of wing rock by flow visualization utilities have been encouraged to develop a complete understanding of the fluid mechanism that drives the motion as well as for prediction purposes. Previous wind/water tunnel simulations have been limited to a single degree-of-freedom (DoF) in roll. Numerical simulations utilizing computational fluid dynamics (CFD) have also been limited to a single DoF in roll and applied to simple flying delta-wing configurations. The loss of simulation accuracy due to reducing the actual wing rock six DoF to a single roll-only DoF has not as yet been fully investigated. In this study, for the first time, wing rock is computationally simulated in three DoF: roll, sideslip, and vertical motion to study the effect of adding the sideslip and vertical motion. The results are for a generic fighter model consisting of a fore-body, a cropped delta wing, and a vertical fin. The effect of including the vertical fin is also studied.

Computational simulation of wing rock in three DoF for a full generic fighter model is a multidisciplinary problem involving grid generation (which requires the utilization of the multi-overset mesh technique), aerodynamics, and rigid-body dynamics. The coupling of the flow governing equations and the rigid-body dynamics equations has been done utilizing an innovative sub-iterative scheme that works on the coupled set of equations. The advantage of implementing this sub-iterative scheme is to reduce the inherent time lag between the solutions of the aerodynamics and rigid-body dynamics.

The interaction of aerodynamics and rigid-body dynamics during a single DoF wing rock for the wing-body configuration has been studied via snap shots of a cross-plane stagnation pressure distribution and tracing the instantaneous locations of vortex burst for an entire cycle of wing

rock. An innovative explanation of the fluid mechanism that drives and sustains the motion has been introduced.

The effect of adding the sideslip and vertical motion DoF to the simulations of the wing-body configuration was found to delay the onset and to reduce the amplitude of wing rock by about 50% with surprisingly no change in frequency. In an effort to correlate the variation of the rolling moment coefficient with the associated sideslip for a full cycle of wing rock, a pseudo dihedral derivative was found to have a clearly stable mean value (-0.0591 rad^{-1}).

The wing rock simulation in three DoF was repeated for the full generic fighter model with the fin included. The aerodynamic effect of the fin was found to significantly delay the vortex burst on the upper surface of the wing. The net effect of the fin was found to augment the damping of the oscillations with significant increase in frequency.

SIMULATION AND ANALYSIS OF WING ROCK PHYSICS FOR A GENERIC FIGHTER MODEL WITH THREE DEGREES-OF-FREEDOM

Chapter 1- Introduction and Background

1.1 Introduction

Present-day fighters are tailored specifically to operate at high speeds and high angles of attack to meet the demands for air superiority. A configuration consisting of thin, low aspect ratio, highly swept-back or delta wing and a long slender fuselage has been adopted in most modern fighters. Also, aerodynamic features and control systems have been devised to provide a significant increase in the operational angle of attack range. The employing of these modern configurations led to a high reduction in drag, especially in the transonic and supersonic regions, and consequently a considerable increase of the maximum attainable speeds. The concentration of mass around the longitudinal axis has significantly reduced the rolling-axis moment of inertia, and thus augmented the maximum attainable roll rates. Two key-elements of air superiority, speed and maneuverability, have been dramatically improved in these modern configurations. However, on the downside, the low-speed aerodynamic characteristics have generally deteriorated. Flying these configurations at low speeds requires relatively high values of angle of attack, which promotes a typical three-dimensional vortical flow. Highly swept-back or delta wing configurations are known to have stronger directional stability compared with its lateral one. This reduction in lateral stability together with the reduction in the rolling inertia increases the susceptibility of modern configurations to rock under any lateral perturbations. Once a lateral

perturbation is triggered, the vortical flow starts to interact with the body leading to oscillations, primarily in roll, that vary in nature according to the value of angle of attack. At low angles of attack the resulting oscillations are damped, but at higher angles of attack the damping is reduced and a limit cycle may be reached. The limit cycle condition is commonly referred to as "Wing Rock", which has been investigated through intensive research in the past two decades.

Lateral position precision is of prime importance for handling quality assurance of a modern fighter, and thus it's rating. Target tracking (Roll-and-Hold), air refueling (receiver), and landing in a crosswind condition are examples of maneuvers where stable lateral position control is vital. For example, in the takeoff/landing of the F-14A, at 28-deg angle of attack, the stall is characterized by divergent wing rock that can reach 90 degrees within 6 seconds if the stick is held back [2:876]. Moreover, high-frequency wing rock can lead to a phenomenon known as "Pilot-Induced Oscillations" or PIO, if the pilot's response to control (or suppress) the oscillations is slower than the motion.

One of the research interests in the area of wing rock is simulation, which provides useful information in the preliminary design phases about limit cycle characteristics and the onset angle of attack. Moreover, simulation can be used in the analysis and study of the physical mechanism that drives the motion. Simulations of wing rock began experimentally in wind/water tunnels for a simple delta wing [24,31,43] with a single degree-of-freedom (DoF) in roll and later were extended to full-fighter models with a single DoF [4,42]. With the computer revolution of the 80's, numerical simulations of wing rock have been encouraged. Computational simulations have been shown to provide results that agree well with experimental data. The developments in the computational resources have led to considerable improvements in the accuracy of the computational simulations. Generally though, computational simulations have been limited to delta-wing configurations with a single DoF in roll.

The aircraft degrees-of-freedom are in general coupled; where the degree of coupling depends on the nature of the maneuver and flight conditions. One of the most useful studies in

flight dynamics is to determine for a particular maneuver, either theoretically or experimentally, the dominant degrees-of-freedom, or equivalently a reduced order model (ROM). The use of a ROM provides a very close response to the original model at lower computational or experimental efforts. In complex maneuvers, it is hard or even impossible to theoretically prove that the ROM is adequately representing the original model. So, for most of the complex maneuvers, experiments are used to prove the reliability of the ROM. In the latest reviews on wing rock, Katz [27] and Mabey [37] have reported (results of which will be presented in detail in Chapter-2 that previous simulations of wing rock have been conducted with only a single DoF in roll. Also, the delta wing has only been modeled to represent the aerodynamics of the full aircraft configuration. The reliability of the computational and experimental simulations based on this ROM has not as yet been fully investigated.

In previous work by Liebst [33,34,35] on the F-15, the sideslip has been shown as the second major contributing DoF after roll. In a study by Saad and Liebst [48] on the F-15, the dihedral derivative, and hence the sideslip, has been shown as the major contributing derivative that controls the value of wing rock onset.

In the present study, the accuracy of the prediction of the onset angle of attack and the limit cycle characteristics based on a simple delta-wing with a single DoF in roll will be analyzed. The simulations of the wing rock oscillations for a generic wing-body configuration modeled with a single DoF in roll will be compared and analyzed with that corresponding to three DoF modeled with roll, sideslip, and vertical motion. Also the simulations will be done for the wing-body with and without the vertical fin to study the effect of including the fin in the prediction studies.

1.2 Various Types of Wing Rock

Vortical flow over highly swept-back or delta wings at high angles of attack is highly nonlinear due to vortex asymmetry, streamwise and cross-flow separation, and/or vortex breakdown. Due to the complexity of the interaction of one or more of these phenomena with the rigid-body motion, many studies have been conducted to thoroughly understand the physics of the phenomena.

Previous research [4,9,11,13,14] shows that, the driving fluid mechanism of wing rock is not unique but rather is greatly dependent on the model geometry and configuration. In the following, the various sources of wing rock will be discussed based on the experimental and computational results provided in [4,7,22,29], and the analysis reported in [9,10,11,12,13,14,21,27,37].

1.2.1 Slender Wing Rock. This is the case of wing rock of highly swept-back delta wings and limited cases of blended wing-bodies. Slender wing rock is triggered at sufficiently large angle of attack by an asymmetric leading edge (L.E.) vortex shedding. Asymmetric vortex shedding could be the result of flying situations such as, the failure of the pilot to recognize minute incomplete wing leveling when he pulls up on the stick. Also, flying at large angle of attack in asymmetric flow conditions (typical landing in a cross-wind) or induced lateral oscillations due to unsteady flow over the wing and/or control surfaces could lead to the shedding of an asymmetric vortex.

To completely understand the fluid mechanism of the motion, let us assume a slender delta wing (sweep angle > 76 degrees) in an asymmetric flow condition represented by a slight positive sideslip. As a result, the L.E. leeward vortex shifts outboard, and the L.E. windward vortex shifts inboard causing the wing to initially roll in the positive roll direction. The sudden roll movement causes the leeward vortex on the up-going wing to compress and the windward vortex on the down-going wing to stretch, which increase the initiated rolling moment. As the roll angle increases, the kinematic-coupling between the angle of attack and the sideslip causes

the effective angle of attack on the wing to decrease and the effective sideslip angle to increase. The increased sideslip on the wing during roll causes the windward vortex on the down-going wing to move inboard and toward the surface, and the leeward vortex on the up-going wing to move outboard and lifted off. The convective time lag associated with the motion of the lifted off vortex causes the right wing to continue dipping until the lifted vortex takes its final position. Then the lift on the down-going wing is increased, while that on the up-going wing is decreased. The previous effect of vortex lift-off together with the reduction of vortex strength due to the decrease of the effective angle of attack causes the wing to stop at a finite roll angle (the limit cycle amplitude), and then reverses its motion. As the wing reverses its motion, the effective angle of sideslip decreases and the lifted vortex starts to reattach. The convective time lag of the vortex motion helps the rolling moment to build up in the reversed direction until the vortex is completely reattached to the leeward side of the left wing. What remains to be explained is how the wing overshoots its initial equilibrium (bank zero). This is due to the hysteresis associated with the structure and location of the L.E. vortices over the two wing halves during the oscillation as shown in figure 1-1.

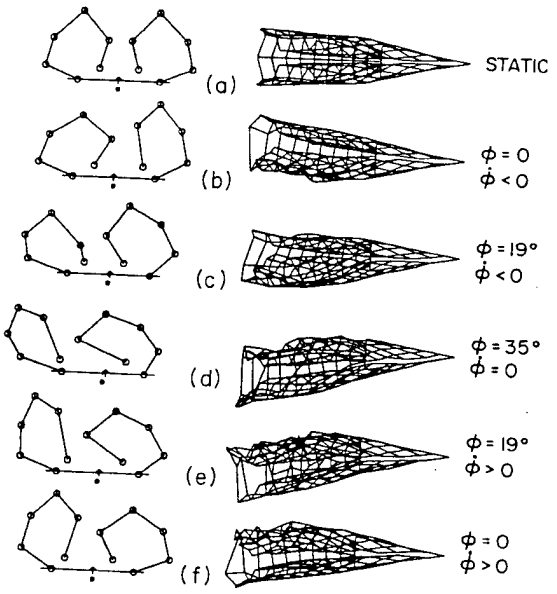

Figure 1-1. Vortex structure at the trailing edge during rolling, generated by the *Vortex-Lattice* method [29].

1.2.2 Conventional-Wing Rock. This is the wing rock associated with aircraft of straight or moderately swept wings, and moderate to high aspect ratio. In other words, the case in which the aerodynamics of the wing is dominated by the two dimensional streamwise flow, and wing rock is closely related to dynamic stall [11].

The fluid mechanism of this type of wing rock is best understood by considering the analysis of plunging oscillations of airfoils. This analysis is very similar to that of the well-known dynamic stall phenomenon associated with a nonzero pitching airfoil [14]. Simply, if an airfoil is perturbed in plunge when flying close to stall, the down-rolling wing-half will experience an upstream movement of the viscous wall effect, which promotes separation on its windward side, and hence reduces lift over the static one (figure 1-2-A). On the other hand the up-rolling wing half will experience a downstream movement of the wall effect, which will delay the separation on its leeward side, and hence increases lift over the static one (figure 1-2-B). This dynamic stall effect produces the driving rolling moment for the wing. As the rolling angle increases, the kinematic-coupling between angle of attack and angle of sideslip reduces the effective angle of attack. At a sufficient rolling angle, the value of the effective angle of attack goes below the stall angle of attack, which causes the flow to reattach on the windward side of the down-stroking airfoil. This generates the required restoring rolling moment, which stops the roll and turns it in the reverse direction.

At high subsonic Mach numbers, the plunging effect makes little difference from the previously discussed case. The flow separation in this case is driven by the shock-boundary layer interaction. The boundary layer transition by itself causes divergent wing bending oscillations. The moving wall effect on the plunging airfoil of the bending wing will promote the transition on the topside during up stroke, and will delay the transition on the bottom side during down stroke, which results in a similar effect like the one previously discussed.

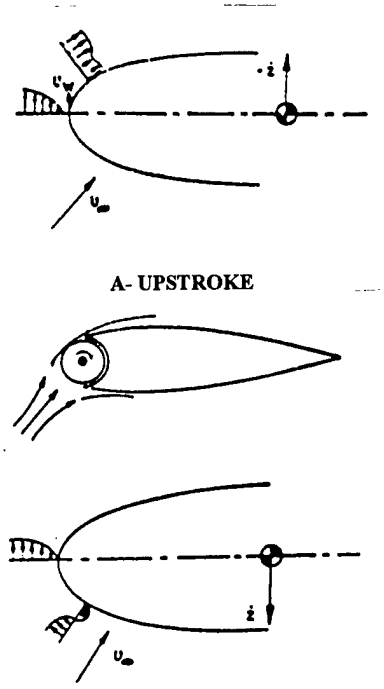

Figure 1-2. Wall effect on an airfoil undergoing plunging motion [14].

1.2.3 Wing-Body Rock. This type of wing rock is very important because, it is obviously the most consistent configuration encountered in real flying vehicles. Also, experimental results indicated that the wing rock induced by fore-body vortices is more violent than the one induced by the leading edge of a flying wing alone [4,13,21]. Typical results on a generic fighter model [4] show a build-up to 30-40 degrees of limit cycle amplitude over less than 3 cycles. This is very dangerous in the sense that it doesn't permit enough time for the pilot to recover before the development of the limit cycle.

According to the flow visualization pictures taken during the wing rock, an asymmetry-switching mechanism of the fore-body vortices was encountered in the same fashion to that of the slender delta wing leading edge vortices [4,13].

The following discussion on the effect of the fore-body cross-section geometry on the wing rock characteristic is referred to Brandon and Nguyen [4]. Different fore-body cross-sections (vertical ellipse, hemispherical, chine, circular, and horizontal ellipse) are mounted on a generic fighter model (a flat-plate trapezoidal wing of 26 degrees sweep, flat-plate horizontal and vertical tails, and fore-body of horizontal ellipse cross-section). The most violent oscillations were found for the horizontal ellipse (>30 degrees amplitude), the moderate oscillation (20-25 degrees amplitude) for the hemispherical and circular, and surprisingly the mild oscillations (<10 degrees amplitude) for the vertical ellipse and chine (see figure 1-3).

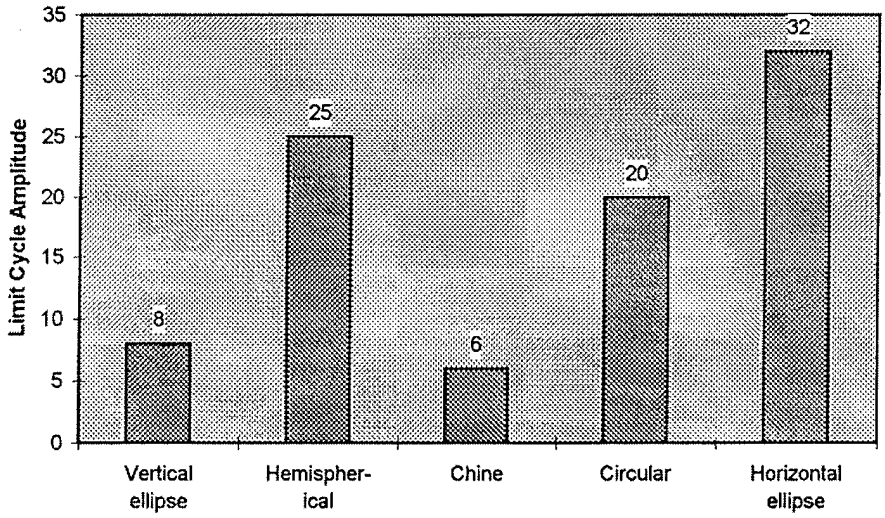

Figure 1-3. Effect of various fore-body configurations on the limit cycle amplitude [4].

1.3 Overview

The remainder of this study consists of six chapters. In Chapter-2, the previous research on wing rock simulations, experimentally and computationally, is reviewed and presented. In Chapter-3, the computational model and the methodology adopted in the solution are described in detail. Chapter-4 is devoted to the illustration of the model geometry and the grid generation process. The analysis and results are presented in Chapter-5, with the conclusions and recommendations presented separately in Chapter-6. Also, the study includes four appendices, appendix-A and B contain typical input and output for the *PEGSUS 4.0* code [51]. A complete

derivation for the Euler boundary conditions is found in appendix-C, and the derivation for the computation of the aerodynamic forces and moments is presented in appendix-D.

Chapter 2- Review of Previous Work

This chapter is devoted to the review of previous work on the experimental and computational simulation of wing rock. The focus in the review is centered on the geometry and configuration of the tested models, the utilized degrees of freedom, and a summary of the concluding results.

2.1 Experimental Simulations

The earliest observations of the wing rock phenomena were reported in the late 40's, and since then numerous studies on wing rock have been conducted and reported in the literature. However, the understanding of the fundamental flow mechanisms that drive wing rock has remained limited. The advancements in wind tunnel testing techniques, flow visualization technology, and computational fluid dynamics (CFD) have made the 80's and 90's an era of recognized intensive experimental and computational research on wing rock.

In an early effort to clearly understand the aerodynamic mechanism that causes slender delta wings to rock, the NASA Langley Research Center (LaRC) conducted a study authored by Nguyen, Yip, and Chambers in 1981 [42]. The study comprised experiments conducted in three low-speed wind-tunnel facilities to provide four kinds of testing, standard static-force, forced-oscillation, rotary, and free-to-roll tests. An 80°-sweep flat-plate delta wing, constructed of wood and sharply beveled at the leading edges was tested. An important feature of the model was that the roll-axis laid in the plane of symmetry parallel to the x-body axis but shifted below by 2 inches. The research provided groundbreaking results for the slender delta-wing rock with single degree-of-freedom (DoF) in roll. The model started to rock at angle of attack (AOA) of 25 degrees, while vortex bursting was not observed below 30 degrees. These early observations demonstrated that slender wing rock is usually triggered by leading-edge vortex asymmetry,

while vortex burst (if encountered) affects the value of the amplitude and frequency of the limit cycle. Static tests for various sideslip angles showed that the vortex burst location on the windward side moves toward the leading edge and the leeward vortex core is lifted-off the wing. That is, sideslip is responsible for driving one of the two major aerodynamic mechanisms that control the wing rock motion. Dynamically speaking, one can say that wing rock is sustained by the dependence of the aerodynamic damping in roll on sideslip such that it is positive (unstable) for small sideslip during the onset of wing rock and negative (stable) for large sideslip during the fully-developed wing rock. This idea was actually the initial motivation for the present research to determine the significance of including the sideslip DoF on the limit cycle characteristics of wing rock.

Subsequently in 1982, Levin and Katz [31] conducted a similar experiment. The model geometry was very much similar to Nguyen's model except for the roll axis, which coincided with the body axis. The shifting of the roll axis in the Nguyen's experiment was a source of slightly increased sideslip (one can easily prove that, $\Delta\beta \cong pd/U_\infty$, where p is the roll rate, d is the shifted distance, and U_∞ is the free-stream velocity). The authors were able to construct boundaries for the slender wing rock, which were correlated to the initial combination of AOA and sideslip [31:36].

In 1986 NASA LaRC sponsored research aimed at investigating the effect of forebody geometry on the static and dynamic stability of aircraft at high angles of attack. The research was conducted by Brandon and Nguyen [4], and the results were previously demonstrated in Subsection 1.2.3.

In 1986 Hall and Del Frate [21] conducted a water-tunnel study on the interaction between the forebody and wing primary vortices. The authors selected three common fuselage cross-sections, circular, chine of 90°-included angle, and chine with 7.5^{0}-included angle that produce weak, medium, and strong forebody vortex strengths respectively. This analysis of the effect of

three forebody cross-sections concluded that the stronger the forebody vortex, the more energy is imparted to the wing vortex system, and consequently the more resistance to vortex burst. The results for the three forebodies mounted on a 55°-sweep cropped delta wing model in zero sideslip showed a burst onset of 22.5° in AOA for the circular, 40° for the 90°-chine, and 45° for the 7.5°-chine. In sideslip, large differences in the burst locations between the windward and leeward wing sides were clearly distinguished, which in turn increases the asymmetry tendency in sideslip.

Jun and Nelson [24] in 1987 conducted experiments on an 80°-sweep delta wing similar to the experiments found in [31,42]. With only slight differences in the model installation, which was mounted on a sting that permits free roll of the model about a bearing system located in the sting support. The experimental results confirmed the early results in [31,42] that the dynamic vortex trajectories differ from the static trajectories and depend on the direction of roll. Differences were also observed in the location of vortex breakdown between the static and dynamic cases.

In 1993, Straka and Hemsch [50] conducted an experiment in the NASA LaRC water-tunnel to determine the effect of a circular-section forebody on the location and onset of vortex burst on a 69.3°-sweep delta wing. The variation in vortex burst location with angle of attack at zero sideslip was recorded for the wing alone, and the wing-fuselage combination. It was concluded that, adding the body to the delta wing adversely affected the onset and the chordwise progression of vortex burst on the wing.

Preliminary prediction of aircraft stall, post-stall, and spin characteristics based on classical prediction methods or systematic wind tunnel testing are limited due to the complexity of the aerodynamics. The most reliable source of information about those critical maneuvers prior to actual flight tests is the unconstrained testing of a properly dynamically-scaled model. The principal techniques were the wind-tunnel free-flight technique for stall and departure, the spin-

tunnel technique for spin and recovery, and the radio-controlled drop-model technique (RCDMT) for stall and post-stall motions. In 1987 Fratello et al [15] conducted research at NASA LaRC to study the high-AOA characteristics for a 20% dynamically-scaled X-29A model, utilizing the unconstrained RCDMT. The wind-tunnel tests had predicted a 25-degrees angle of attack for the onset of wing rock. The results obtained from the RCDMT verified an earlier onset at 20^{o}, and with further increase of angle of attack the wing rock motion grew rapidly, with the amplitude doubled in only one oscillation. At an average angle of attack of 32^{o}, the motion diverged into a violent snap roll departure of peak roll rate over (130 deg/s).

In summary, the previous experimental simulations on wing rock have been limited to a single DoF in roll. The bearing mounting and friction have affected the predicted limit cycle characteristics as was previously reported by Levin and Katz [31]. Only the *RCDMT* can provide a realistic simulation; however it is still considered expensive and technically difficult, and hence of limited use.

2.2 Computational Simulations

The rapid developments in computer speed, architecture, and memory in the early 80's had a great impact on the improvement of aerodynamic numerical solutions. The improvements in the aerodynamic numerical solutions have been complemented by parallel progress in grid generation and flow visualization techniques. The whole package, the grid generation, flow solver, and flowfield visualization utilities, have become the computational tunnel for present-day aerodynamic research. Most of the developed computational codes have been successfully validated by comparison with numerous experimental data.

Computational simulation of wing rock has been encouraged due to the difficulty of model installation for free motion in the tunnel, and for better flowfield visualization. In the following review, the computational work on wing rock simulation will be reviewed and presented.

In 1982 Levin D. and Katz J. [32] introduced a modified version of the classical *Vortex Lattice* method that is capable of solving both, the steady and unsteady aerodynamics as well, with an application for the simulation of leading edge vortices over delta wings at high AOA.

Shortly afterwards Konstadinopoulos, Mook, and Nayfeh [29] coupled the *unsteady vortex-lattice* method with the rigid body dynamics in roll to numerically simulate the previous experiments for Nguyen [42] and Levin [31]. The results showed good agreement with the corresponding experimental data.

In 1989 Katz J. [26] introduced a new application for the *Unsteady Vortex Lattice* method by computing the conical rotary loads on a standard dynamic model. The author was able to demonstrate excellent agreement with the experimental data, at low Mach number (M = .15) and moderate angles of attack (AOA < 15 degrees), with extremely low computational cost.

The limited capabilities of the early supercomputers nudged the first CFD simulations of wing rock to less-costly computational solutions such as the Conical Euler and Euler schemes. One of the earliest works utilizing these schemes was due to Lee and Batina [30] in 1991 from NASA LaRC. The simulation has been done for a slender delta-wing configuration (leading edge sweep of 75^{o}) at Mach number 1.2. The supersonic freestream Mach number allowed the implementation of the conical flow similarity, and hence reduced the problem from three dimensions to two dimensions, which considerably reduced the computational cost. The authors utilized the cell-centered finite-volume algorithm for solving on an unstructured grid made up of triangles. An explicit artificial dissipation of second and fourth order was added to prevent oscillations near shock waves and damp out high-frequency uncoupled error modes. The rigid-body roll equation has been explicitly coupled with the flow governing equations. The time derivatives in the rigid body equation were approximated by a 2^{nd}-order accurate backward finite-difference. The number of elements used in this study was 8299, which had a total of 4226 nodes, with refinement on the leeward side of the wing where the dominant flow features were

expected to occur. The wing rock was excited by an initial roll rate at angle of attack of 30°, and a limit cycle of amplitude 38° was observed, which agreed well with the earlier experiments.

In 1992, Kandil and Salman [25] took a step forward by coupling the unsteady Euler equations with the rigid body dynamics in roll. They simulated the wing rock oscillations and divergence for an 80°-sweep delta wing at 30° AOA and Mach number of 0.3. The unsteady Euler equations was used to simulate the fluid dynamics, while the four-stage Runge-Kutta scheme was used to solve the rigid-body dynamic equations. The flow governing equations were solved in the moving frame of reference, which adds an extra computational cost for the source terms. However, the use of this approach saves regenerating the grid and recalculating the values of the transformation metrics after each time step. The implicit, approximately-factored, centrally-differenced, finite-volume scheme was employed, with 2^{nd} and 4^{th}-order explicit dissipation terms. Implicit 2^{nd}-order dissipation terms were also added to enhance the scheme stability. The grid consisted of 32x32x48 grid points in the axial, normal, and wrap-around directions.

In 1993 Chaderjian and Schiff [6] presented an early application of a generalized full Navier-Stokes based-code. They conducted static tests to investigate the nonlinear variation of the rolling moment coefficient with angle of attack for a 65°-sweep delta wing at 30° AOA, 3.67×10^6 Reynolds number, and a Mach number of 0.27. The three-dimensional, Reynolds-averaged, Navier-Stokes (RANS) equations were used to model the viscous flow. The relatively high Reynolds number used in this study allowed the application of thin-layer approximation. The perfect gas law, Sutherland's viscosity law, and a turbulence model were used to complete the RANS system of equations. The governing equations were transformed to body-fitted curvilinear coordinates using general coordinate transformation. The numerical procedure comprised of the implicit Beam and Warming algorithm [3], approximately-factored, and centrally-differenced. A three-dimensional hyperbolic grid generator was used to generate

67x49x208 nodes in the axial, normal, and circumferential directions, a total of about 700,000 nodes. The run of this code for one static roll angle was reported to require 48 hours on the C-90 computer to reach a steady state.

In an effort to validate the code developed in [6] for dynamic testing, Chaderjian [5] in 1994 simulated the forced large-amplitude, high frequency roll oscillations. The RANS equations were written in the inertial frame of reference and transformed to the body-fitted curvilinear frame of reference via the generalized time-dependant coordinate transformation. The comparison of the results with the corresponding experimental data showed a very good quantitative agreement. The computational cost of the developed code to advance one time step on the Cray Y-MP is 18 μs/grid-point/time-step. One cycle of oscillations took 15,000 time steps, which requires 50 hours of CPU-time for a total of 700,000 grid points. Later in 1996, Chaderjian and Schiff [7] coupled the rigid-body dynamic equations in roll with the RANS equations and simulated the free roll motion of wing rock for the same previous model. The resulted computational free roll motions were reported to damp out more rapidly compared with the experimental simulations, but the computed and experimented frequencies were in good agreement.

In 1993, Gordnier and Visbal [19] presented an application for the *fdl3di* code, which has gone through a similar validation procedure from static to forced roll tests. The code is very similar to the one developed by Chaderjian and Schiff [6], except for a few differences. Unlike the previous code, which utilizes the thin-layer version of the Navier-Stokes equations, the *fdl3di* utilizes the unsteady, three-dimensional, full mass-averaged Navier-Stokes equations, which extends its application to low Reynolds numbers as well. An additional feature in the *fdl3di* code is the implementation of the sub-iteration algorithm to reduce the various errors due to the factorization, the lag in applying the boundary conditions, and the inherent lag in the solution of the coupled equations. The sub-iteration algorithm has greatly improved the stability and accuracy of the computational scheme. The code has been validated by experimental data of two

previous experiments, for the 80° and 65° delta wing models. Both, static and forced-roll simulations, were conducted to demonstrate the variations in the vortex structure and strength due to the dynamic interaction during a constant roll rate motion. A useful discussion on the vortex dynamics has been introduced to explain the reduction in the restoring moment in the dynamic case (the presented analysis on slender wing rock in subsection 1.2.1 is mostly referred to this paper). Gordnier [16] has analyzed the effect of roll rate and initial acceleration on the vortex dynamics during a forced-roll maneuver for the 80°-sweep delta wing model. In 1997, Gordnier [18] presented static roll tests for the same model used by Chaderjian [5,6,7] but at lower Reynolds and Mach numbers to demonstrate the ability of the code to simulate complex viscous flows. Also, Gordnier [17] has demonstrated the ability of the *fdl3di*-code to simulate the spiral vortex breakdown and the transition from spiral to bubble-type breakdown with very good qualitative agreement with the experimental data.

In an effort to model the nonlinear, unsteady aerodynamics for the rolling 65° delta wing, Tromp [52] has simulated the constant-rate conical motion, constant-roll rate, and the barrel-roll maneuver. The numerical simulation has been done using the *fdl3di*-code for zero and 30 degrees AOA. The numerically computed loads have shown an excellent agreement with the experimental data.

In summary, it has been shown in the previous review that the computational wing rock simulations were commonly conducted for a single DoF in roll and applied to either flying delta wing or blended wing-body (without fore-body) configurations.

Chapter 3 - Computational Model

3.1 Flow Aerodynamics

All the computational experiments in this study are conducted at a Mach number of 0.4 and pressure altitude of 2000 meters. The corresponding Reynolds number for this flight regime, based on the root chord length, is significantly high ($Re_\infty = 2.472 \times 10^9$), which motivated the use of the Euler equations to reduce the computational cost. The Euler equations have been used widely to simulate vortical flow aerodynamics on highly swept-back or delta-wing configurations at moderate-to-high values of Reynolds number [1,25,30,38,47]. The Advisory Group for Aerospace Research & Development (AGARD) [1:162] in its review on computational aerodynamics based on the Euler equations has reported that the Euler solutions have the ability to adequately simulate vortical flow aerodynamics and leading edge vortex breakdown on delta-wing configurations. Also, Yu et al [55] have reported excellent agreement with experimental data for the Euler solution of a complete commercial transporter in transonic flow conditions and sideslip. A modified version of the *fdl3di* code, provided by the Air Force Research Laboratory (*AFRL*), Wright-Patterson Air Force Base, Ohio, has been utilized to provide the finite difference modeling and solution of the Euler flow governing equations.

3.1.1 Flow Governing Equations. The unsteady three-dimensional compressible Euler equations in strong conservation form have been used. The equations have been written in a fixed inertial frame of reference and transformed to the computational domain using a generalized time-dependant transformation (ξ, η, ζ, t). The flow variables are nondimensionalized as follows:

$u^* = u/U_\infty$

$v^* = v/U_\infty$

$w^* = w/U_\infty$

$P^* = P/(\rho_\infty U_\infty^2)$

$\rho^* = \rho/\rho_\infty$

$T^* = T/T_\infty$

$e^* = e/U_\infty^2$

All coordinate lengths have been normalized by the root chord-length of the delta wing, C_r.

$x^* = x/C_r$

$y^* = y/C_r$

$z^* = z/C_r$

Where $x = y = z = 0$ is at the nose.

The final form of the transformed nondimensionalized equations in strong conservation form can be written as follows:

$$\frac{\partial Q}{\partial t} + \frac{\partial F}{\partial \xi} + \frac{\partial G}{\partial \eta} + \frac{\partial H}{\partial \zeta} = 0 \qquad (3\text{-}1)$$

Where:

The vector of dependent variables is given by:

$$Q = \frac{1}{J}\begin{bmatrix} \rho^* \\ \rho^* u^* \\ \rho^* v^* \\ \rho^* w^* \\ \rho^* e_t^* \end{bmatrix}$$

The vector fluxes are given by:

$$F = \frac{1}{J}\begin{bmatrix} \rho^* u^* \\ \rho^* u^* \overline{U} + \xi_x P^* \\ \rho^* v^* \overline{U} + \xi_y P^* \\ \rho^* w^* \overline{U} + \xi_z P^* \\ \rho^* e_t^* \overline{U} + P^* U` \end{bmatrix} \quad G = \frac{1}{J}\begin{bmatrix} \rho^* v^* \\ \rho^* u^* \overline{V} + \eta_x P^* \\ \rho^* v^* \overline{V} + \eta_y P^* \\ \rho^* w^* \overline{V} + \eta_z P^* \\ \rho^* e_t^* \overline{V} + P^* V` \end{bmatrix} \quad H = \frac{1}{J}\begin{bmatrix} \rho^* w^* \\ \rho^* u^* \overline{W} + \zeta_x P^* \\ \rho^* v^* \overline{W} + \zeta_y P^* \\ \rho^* w^* \overline{W} + \zeta_z P^* \\ \rho^* e_t^* \overline{W} + P^* W` \end{bmatrix}$$

$$\overline{U} = \xi_t + \xi_x u^* + \xi_y v^* + \xi_z w^*$$

$$= \xi_t + U`$$

$$\overline{V} = \eta_t + \eta_x u^* + \eta_y v^* + \eta_z w^*$$

$$= \eta_t + V`$$

$$\overline{W} = \zeta_t + \zeta_x u^* + \zeta_y v^* + \zeta_z w^*$$

$$= \zeta_t + W`$$

$$e^*_t = e^* + \frac{1}{2}\left(u^{*2} + v^{*2} + w^{*2}\right)$$

The *Jacobian* of the transformation, J, is given by:

$$J = \frac{\partial(\xi,\eta,\zeta)}{\partial(x^*, y^*, z^*)} = \frac{1}{x^*_\xi\left(y^*_\eta z^*_\zeta - y^*_\zeta z^*_\eta\right) - x^*_\eta\left(y^*_\xi z^*_\zeta - y^*_\zeta z^*_\xi\right) + x^*_\zeta\left(y^*_\xi z^*_\eta - y^*_\eta z^*_\xi\right)}$$

The perfect gas equation closes the system of equations (3-1) as follows:

$$P^* = \frac{\rho^* T^*}{\gamma M^2_\infty} \qquad (3\text{-}2)$$

3.1.2 Boundary Conditions. The following boundary conditions are applied to the flow governing equations:

- Characteristic boundary conditions [54] are applied at the far-field and upstream boundaries.
- The values of the flow variables at the exit boundary are extrapolated from the interior by first-order extrapolation.
- Periodic boundary conditions have been applied for the points of symmetry in the wrap-around direction.
- On the body surface the classical Euler boundary conditions have been applied:

$$U_n = \vec{U}_b \cdot \vec{n}$$

$$\frac{\partial P}{\partial n} = -\rho\, \vec{a}_b \cdot \vec{n}$$

Where U_n is the flow velocity component in the direction normal to the body surface. $\vec{U}_b$ and $\vec{a}_b$ are the velocity and acceleration at the surface grid point location $\vec{r}_b$, given by:

$$\vec{U}_b = \vec{U}_{cg} + \vec{\omega} \times \left(\vec{r}_b - \vec{r}_{cg} \right)$$

$$\vec{a}_b = \vec{a}_{cg} + \frac{\partial \vec{\omega}}{\partial t} \times \left(\vec{r}_b - \vec{r}_{cg} \right) + \vec{\omega} \times \left[\vec{\omega} \times \left(\vec{r}_b - \vec{r}_{cg} \right) \right]$$

3.1.3 Numerical Solution of the Flow Governing Equations. The governing equations are solved numerically using the implicit, approximately-factorized finite difference scheme of Beam and Warming [3] in the diagonalized form of Pulliam and Chaussee [46]. The equations are differenced using second-order accurate differencing for temporal and spatial derivatives. A blend of nonlinear second and fourth order spectral damping derivatives is employed. The boundary conditions are explicitly applied, and a sub-iteration algorithm is employed to reduce the effect of the inherent time lag in applying the boundary conditions and reduce the factorization error.

The numerical implementation of the boundary conditions on the body surface is derived and explained in detail in Appendix-C. Also, the numerical computation of the aerodynamics forces and moments on the body surface is presented in Appendix-D.

3.2 Rigid Body Dynamics

The relevant degrees of freedom in this study are the roll, sideslip, and vertical motion. The rolling equation is written in the body-axes frame of reference to keep the roll-axis moment of inertia constant throughout the entire motion, while the sideslip and vertical motion equations are written in the inertial frame of reference.

3.2.1 Rigid Body Dynamic Equations. The rolling equation is a second-order autonomous ordinary differential equation in time.

$$\ddot{\phi} = \frac{L_b}{I_x} \tag{3-3}$$

Where L_b is the body-axis rolling moment, and I_x is the moment of inertia about the body-fixed x-axis.

The sideslip and vertical equations are written in the inertial frame of reference since there is no need to be solved in the body-axes frame of reference. The equations are second-order autonomous ordinary differential equations in time.

$$\ddot{y}_{cg} = \frac{F_y}{m} \tag{3-4}$$

$$\ddot{z}_{cg} = \frac{F_z}{m} - g \tag{3-5}$$

Where F_y and F_z are the side and vertical force components computed in the y and z inertial directions respectively.

A first order state-space representation of (3-3), (3-4), and (3-5) is given by:

$$\dot{\phi} = p \tag{3-6-a}$$

$$\dot{p} = \frac{L_b}{I_x} \tag{3-6-b}$$

$$\dot{y}_{cg} = v_{cg} \tag{3-6-c}$$

$$\dot{v}_{cg} = \frac{F_y}{m} \tag{3-6-d}$$

$$\dot{z}_{cg} = w_{cg} \tag{3-6-e}$$

$$\dot{w}_{cg} = \frac{F_z}{m} - g \tag{3-6-f}$$

Introduce the non-dimensional forms of the roll rate, time, rolling moment of inertia, mass, and gravity acceleration respectively as follows:

$$p^* = \frac{p\,b}{U_\infty}$$

$$t^* = \frac{t\,U_\infty}{C_r}$$

$$I_x^* = \frac{2I_x}{\rho S C_r b^2}$$

$$m^* = \frac{2\,m}{\rho\,S\,C_r}$$

$$g^* = \frac{g}{\left(\frac{U_\infty^2}{C_r}\right)}$$

The first-order system (equation 3-6) is given in non-dimensional form as follows:

$$\frac{\partial \phi}{\partial t^*} = \left(\frac{C_r}{b}\right) p^* \qquad \text{(3-7-a)}$$

$$\frac{\partial p^*}{\partial t^*} = \frac{C_{l_b}}{I_x^*} \qquad \text{(3-7-b)}$$

$$\frac{\partial y_{cg}^*}{\partial t^*} = v_{cg}^* \qquad \text{(3-7-c)}$$

$$\frac{\partial v_{cg}^*}{\partial t^*} = \frac{C_y}{m^*} \qquad \text{(3-7-d)}$$

$$\frac{\partial z_{cg}^*}{\partial t^*} = w_{cg}^* \qquad \text{(3-7-e)}$$

$$\frac{\partial w_{cg}^*}{\partial t^*} = \frac{C_z}{m^*} - g^* \qquad \text{(3-7-f)}$$

3.2.2 Numerical Solution of the Rigid Body Dynamic Equations. The non-dimensional first-order system (3-7) has been differenced in time using second-order accurate backward difference. Thus, the finite difference solution at time level (n) is given as follows:

$$p^{*(n)} = \frac{1}{3}\left[\left(\frac{2C_{lb}^{(n-1)}\Delta t^*}{I_x^*}\right) - p^{*(n-2)} + 4p^{*(n-1)}\right] \tag{3-8-a}$$

$$\phi^{(n)} = \frac{1}{3}\left[2\left(\frac{C_r}{b}\right)\Delta t^*\ p^{*(n)} - \phi^{(n-2)} + 4\phi^{(n-1)}\right] \tag{3-8-b}$$

$$v_{cg}^{*(n)} = \frac{1}{3}\left[\left(\frac{2C_y^{(n-1)}\Delta t^*}{m^*}\right) - v_{cg}^{*(n-2)} + 4v_{cg}^{*(n-1)}\right] \tag{3-8-c}$$

$$y_{cg}^{*(n)} = \frac{1}{3}\left[2\Delta t^*\ v_{cg}^{*(n)} - y_{cg}^{*(n-2)} + 4y_{cg}^{*(n-1)}\right] \tag{3-8-d}$$

$$w_{cg}^{*(n)} = \frac{1}{3}\left[\left(\frac{2(C_Z^{(n-1)} - m^* g^*)\Delta t^*}{m^*}\right) - w_{cg}^{*(n-2)} + 4w_{cg}^{*(n-1)}\right] \tag{3-8-e}$$

$$z_{cg}^{*(n)} = \frac{1}{3}\left[2\Delta t^*\ w_{cg}^{*(n)} - z_{cg}^{*(n-2)} + 4z_{cg}^{*(n-1)}\right] \tag{3-8-f}$$

Where the superscripts between brackets denote the corresponding time level.

3.3 Coupling the Flow Governing Equations and the Rigid Body Dynamic Equations

The rigid body equations are coupled explicitly with the flow governing equations. As seen in equations (3-8-a, c, and e), the aerodynamic forces and moments are computed at a time level (n-1). This inherent lag in the solution of the coupled equations has been addressed through a sub-iteration algorithm. The original *fdl3di* code already employed a Newton-like sub-iteration algorithm on the flow governing equations, which was extended to operate on the coupled set of equations. Figure 3-1 depicts a simple flowchart demonstrating the application of the sub-iteration approach on the coupled set of equations.

3.4 Implementation of the Body Motion

The flowfield interactions due to the body dynamics are implemented in the modified *fdl3di-* code as follows:

- After solving the rigid-body equations the new position of the individual grids, in the inertial coordinate system, is computed by the following transformation:

$$\begin{bmatrix} x^{*(n)} \\ y^{*(n)} \\ z^{*(n)} \end{bmatrix} = \begin{bmatrix} 1 & 0 & 0 & 0 & 0 \\ 0 & \cos\phi^{(n)} & -\sin\phi^{(n)} & 1 & 0 \\ 0 & \sin\phi^{(n)} & \cos\phi^{(n)} & 0 & 1 \end{bmatrix} \begin{bmatrix} x^{*(0)} \\ y^{*(0)} \\ z^{*(0)} \\ y_{cg}^{*(n)} \\ z_{cg}^{*(n)} \end{bmatrix}$$

  Where, the superscript (0) denotes the initial grid position at time level (n = 0), which corresponds to the initial states ($\phi^{(0)} = 0$, $y_{cg}{}^{*(0)} = 0$, and $z_{cg}{}^{*(0)} = 0$).

- Compute the new values of the space and time metrics of the generalized coordinate transformation.

- Compute the velocities and accelerations on the body surface grid points, which are needed for the application of boundary conditions.

3.5 Computer Resources

All the computational simulations presented in this study has been run on the *CRAY T-94* supercomputer at the Ohio Supercomputer Center (OSC), Columbus, Ohio, as part of the granted CPU-Hours for project number *PIS198.*

The *CRAY T-94* computer system at the OSC is a powerful general-purpose supercomputer that features 4 high-speed (450 MHz) processors, each with a peak performance of approximately 2 billion floating point operations per second (2 GFLOPS).

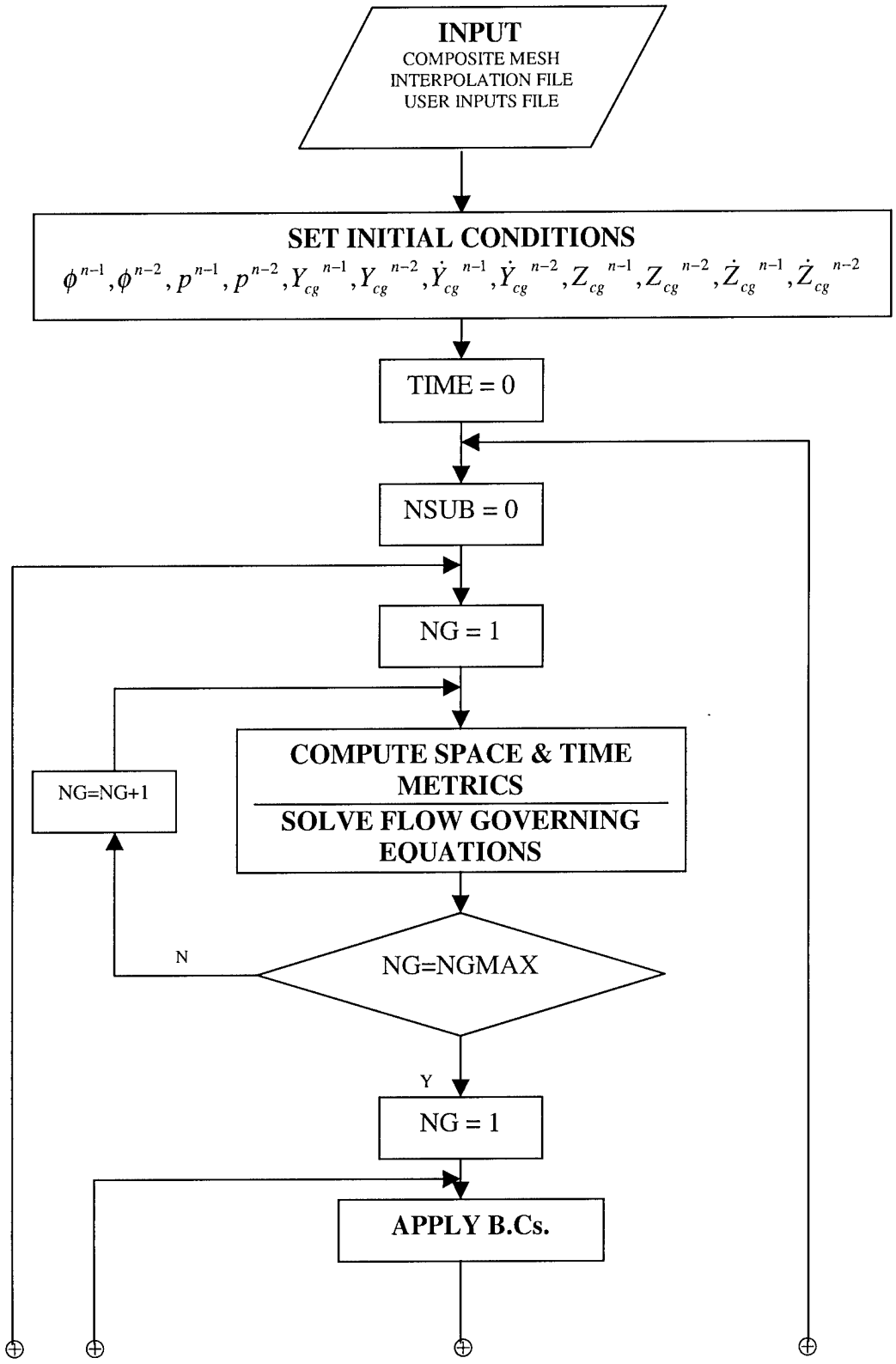
INPUT
COMPOSITE MESH
INTERPOLATION FILE
USER INPUTS FILE
SET INITIAL CONDITIONS
$\phi^{n-1}, \phi^{n-2}, p^{n-1}, p^{n-2}, Y_{cg}^{n-1}, Y_{cg}^{n-2}, \dot{Y}_{cg}^{n-1}, \dot{Y}_{cg}^{n-2}, Z_{cg}^{n-1}, Z_{cg}^{n-2}, \dot{Z}_{cg}^{n-1}, \dot{Z}_{cg}^{n-2}$
TIME = 0
NSUB = 0
NG = 1
COMPUTE SPACE & TIME METRICS
SOLVE FLOW GOVERNING EQUATIONS
NG=NG+1
N
NG=NGMAX
Y
NG = 1
APPLY B.Cs.

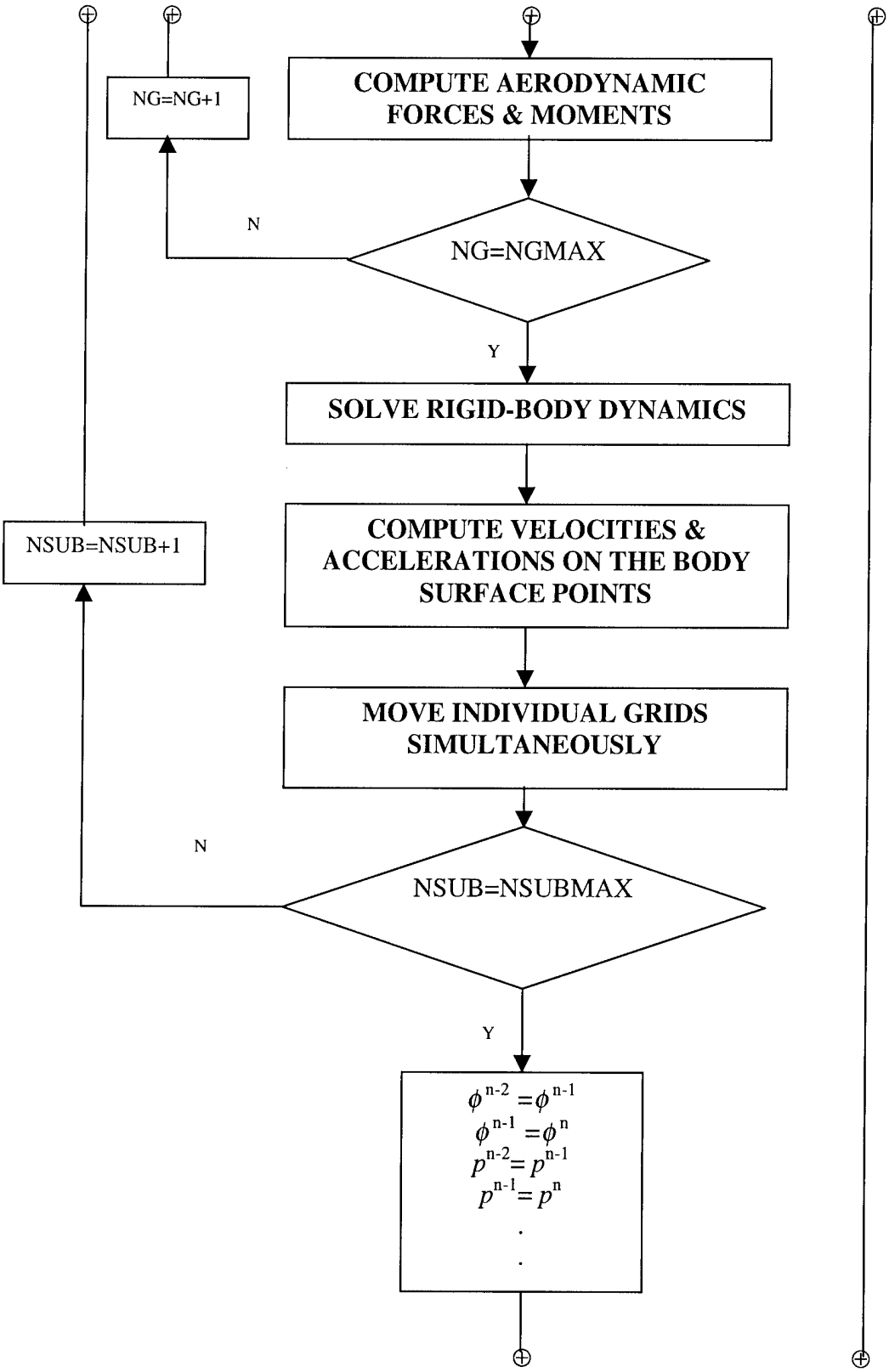
NG=NG+1
COMPUTE AERODYNAMIC FORCES & MOMENTS
N
NG=NGMAX
Y
SOLVE RIGID-BODY DYNAMICS
NSUB=NSUB+1
COMPUTE VELOCITIES & ACCELERATIONS ON THE BODY SURFACE POINTS
MOVE INDIVIDUAL GRIDS SIMULTANEOUSLY
N
NSUB=NSUBMAX
Y
$\phi^{n-2} = \phi^{n-1}$
$\phi^{n-1} = \phi^{n}$
$p^{n-2} = p^{n-1}$
$p^{n-1} = p^{n}$

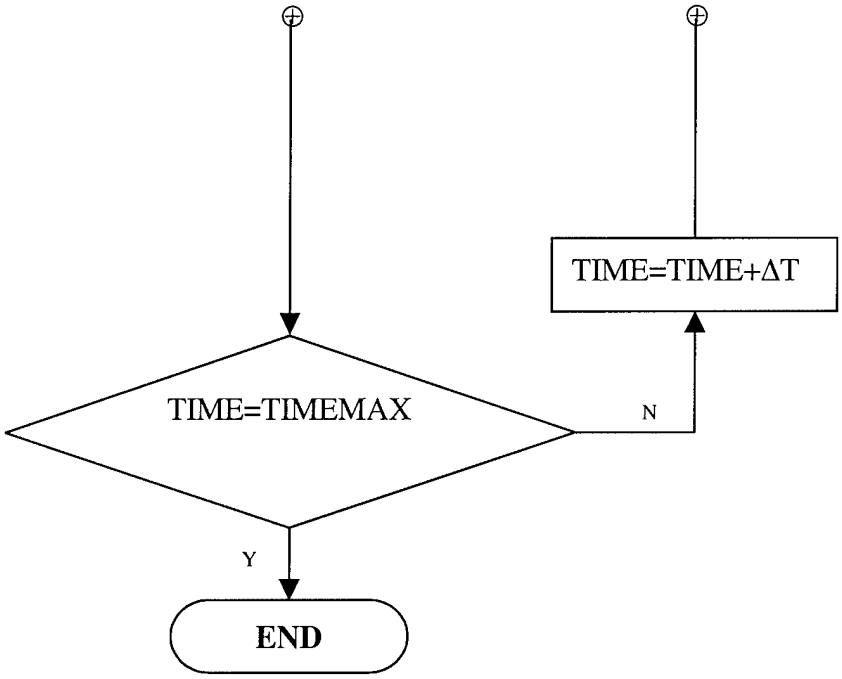

Figure 3-1. Flowchart demonstrating the sub-iteration process.

Chapter 4 - Grid Generation

4.1 The Model

The tested model in this study is a 5% dynamically-scaled model for a generic fighter consisting of fore-body, blended wing-body, and vertical tail (see figures 4-1 and 4-2). The fore-body cross section is a chine of 90°-included angle with a sharp nose of 15° apex-half angle. The wing is a thin flat plate cropped delta wing of 65° sweep with the leading and trailing edges beveled at 45°. The vertical tail has a trapezoidal plane-form with beveled edges, and a finite thickness. The geometry of the body, wing, and tail is chosen for simplicity, but in fact is adopted from realistic present-day fighters such as the Dassault-Breguet Mirage [23].

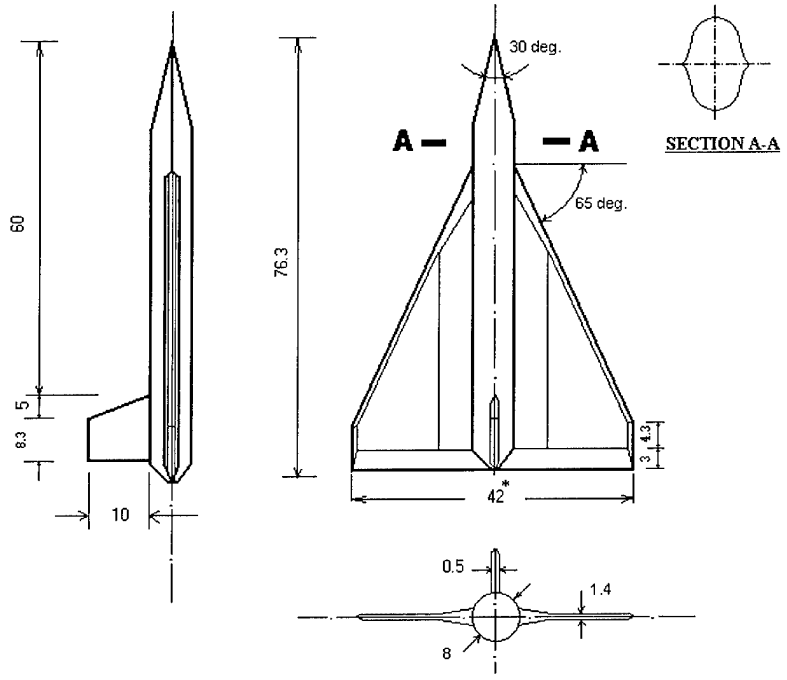

* All dimensions are in cm, unless otherwise stated.

Figure 4-1. Three-view drawing of the generic fighter model.

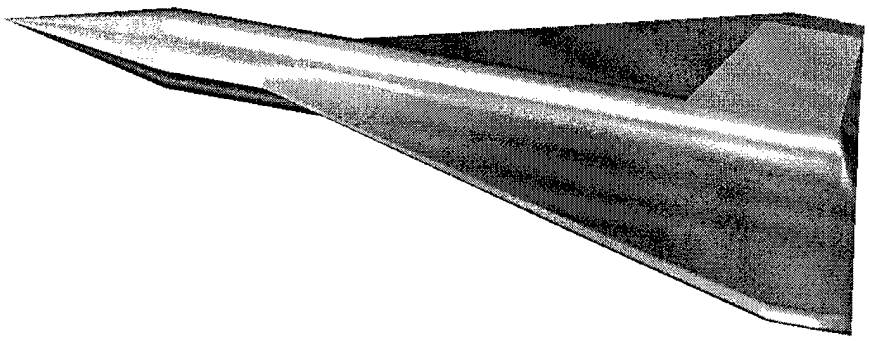

Figure 4-2. Three-dimensional view of the model.

Originally, the model mass was to be estimated from the mass of the Mirage 2000 [23], (7440.3 Kg, empty). Due to the unavailability of the values of the moment of inertia for the Mirage, the mass and longitudinal moment of inertia for the model were estimated instead from that of the A-4 fighter, which has a similar size and shape to the Mirage. The inertia properties of the A-4 fighter [40:405] are given by:

m = 7910 [Kg], and I_x = 10968 [kg-m^2].

So, the non-dimensional inertia parameters of the model (refer to subsection 3.2.1) are given as follows:

m^* = 35.3, and I_x^* = 0.684

4.2 Meshing the Model

The accuracy of a *CFD*-simulation is in general governed by both, the quality of the mesh that resolves the relevant model geometry and physics, and the time/spatial accuracy of the computational scheme. This emphasizes the role of the grid generation process in order to get high quality simulations. Before starting the grid generation process, four key elements should be carefully selected:

- The grid structure (structured vs. unstructured).
- The grid generation technique (Single vs. Multi-overset mesh techniques).
- The grid topology for each individual mesh (H-O, H-H, or C-O...).
- The domain dimensions.

In the remaining part of this section, the author's choice for these elements is discussed and justified.

The utilized code in this study to solve the flow governing equations is the *fdl3di*-code, which is written for structured grids, leaving no choice for grid structure.

In order to justify the selection for the meshing technique, one needs to differentiate among the available alternatives. Three alternatives are possible: either a single O or H-grid, or multi-overset grids. Two factors were taken into consideration in this investigation, the total number of grid points, and the quality of the generated mesh. In the case of a single O-grid, the number of grid points must be increased in the wrap-around direction at the location of the vertical fin to resolve its geometry. This increase of grid points must be made all the way along the axial direction, resulting in unnecessary augmentation of the total number of grid points. Moreover, the generation of a single O-structured grid for the whole model including the tail was found to be difficult if not impossible. For the case of a single H-grid, the clustering of grid lines to resolve the model geometry will propagate all over the computational domain, resulting in a significant increase in the total number of grid points (possibly greater than that for the case of a single O-grid). The quality of the resulting mesh in the case of a single H-grid may exceed the one obtained by the O-grid. However, the cut in the H-grid made by the solid body surface requires modifying the computational stencils at these points to be one-sided everywhere in the code. On the other hand, the utilization of the multi-overset mesh technique allows independent meshing of the sub-domains of interest, which are overset and mutually communicate across the boundaries. In addition to the flexibility obtained by the utilization of the multi-overset technique, the overall

number of grid points is highly reduced compared with that for the case of a single mesh. For all the previous reasons, the multi-overset mesh technique was found to be best suited for our particular model. The model is subdivided into two meshes, one for the wing-body and the other for the vertical fin. The fin mesh is embedded in the wing-body mesh, and a final composite mesh is created.

4.2.1 The Wing-Body Mesh. The axi-symmetric geometry of the wing-body and the conical shape of the fore-body motivate the utilization of a C-O topology for this mesh. Also, it becomes relatively easier to apply the boundary conditions on the body surface in case of a C-O grid. The C-O topology has been extensively used in the literature to mesh blended wing-body configurations [5,6,7,18,25,52]. A structured mesh has been generated using *Gridgen ver. 13* [44]; an initial grid is generated for a quarter of the domain using polar transfinite interpolation.

An elliptic partial differential equation (*EPDE*) solver was run to improve the quality of the grid, and control the grid lines near/on the body surface. A *Thomas-Middlecoff* control function [44] was applied to map the clustering of the grid points on the boundary to the interior domain. A *Steger-Sorenson* control function [44] was applied on the body surface to keep the orthogonality, and hence simplifies the application of boundary conditions. Due to the axi-symmetric geometry of the wing-body section, only a quarter of the domain is generated by *Gridgen*, and the other three quarters are generated by reflection using a FORTRAN routine. The advantage of doing this is to enforce an exact symmetry on the distribution of mesh points, which may be slightly violated if the *PDE* solver has been run for the whole domain. Three grids of different dimensions have been generated (Table 4-1).

The domain consists of a circular cylinder connected to a hemisphere (figure 4-4). The length of the circular cylinder is three characteristic lengths (wing root chord length C_r), and has a radius of 1.5 characteristic lengths (figure 4-4). The domain shape and dimensions have been previously utilized in most meshes of C-O topology [18,25].

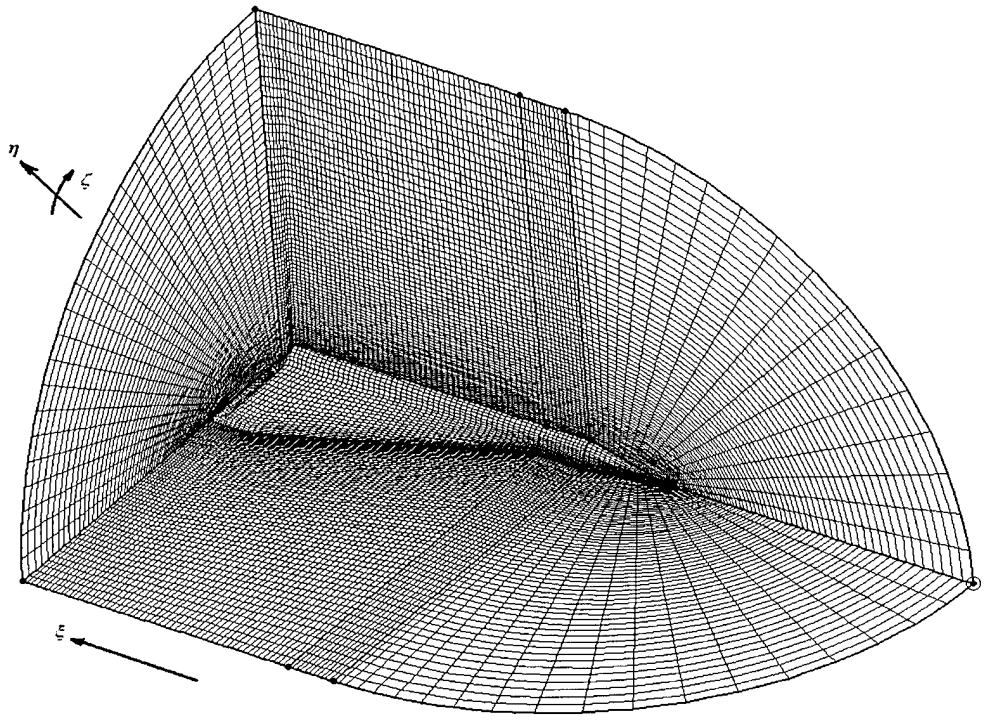

Figure 4-3. Section in the wing-body mesh (coarse) demonstrates the topology.

Table 4-1. Dimensions of the grids.

Grid Type	Dimensions			Total No. of Points
	ξ (axial)	η (normal)	ζ (wrap-around)	
Coarse	79	35	65	179,725
Medium	117	53	97	601,497
Fine	120	70	105	882,000

4.2.2 The Vertical Fin Mesh. The vertical fin mesh consists of the fin and part of the fuselage in order to resolve the area at the fin-fuselage connection (see figure 4-5). An H-H grid is applied for the fin mesh to avoid the inherent singularities of the O-topology. One-half of the domain is meshed using *Gridgen*, and the other half was generated using a FORTRAN routine by reflection along the x-z plane. In the same manner discussed for the wing-body mesh, the *EPDE* solver has been run, applying the same control functions on the interior and the fin/body surfaces. A base line grid of dimensions 43x36x34, in the axial, normal, and bi-normal directions respectively is generated.

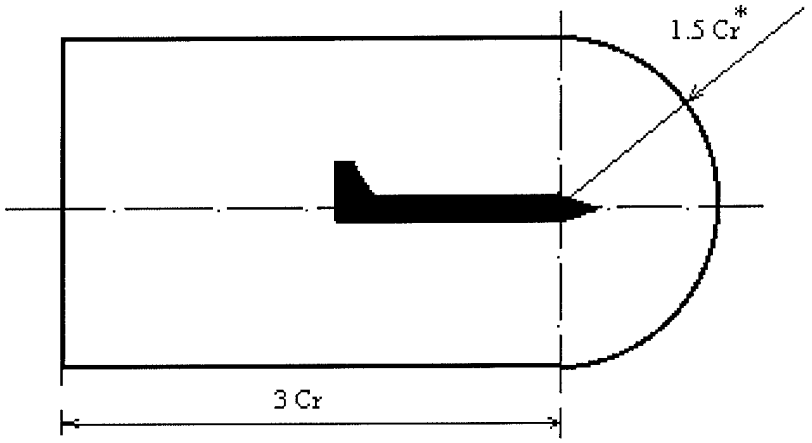

*Cr is the Root Wing-Chord Length.

Figure 4-4. Outer domain dimensions

4.2.3 The Composite Mesh. In this subsection *PEGSUS* [51], the code which implements the *Chimera* (Overset) technique [49], is briefly discussed, then the process of the creation of the composite mesh will be presented. Figure 4-6 depicts a block diagram for the grid generation process, starting from the model geometry and ending up with the composite mesh. For more information on *PEGSUS* and the nomenclature used throughout the rest of this subsection, the

reader may refer to [49,51]. The utilized flow solver in this study (the *fdl3di*-code) implements the multi-overset grid technique, and has been successfully utilized in other applications [38,47] and validated [36]. Interpolation of conservative variables was adopted as recommended in the literature [53].

PEGSUS is designed to perform the following tasks for each individual mesh:

- Establish the communication boundaries (outer, hole or interior boundaries).
- Search for the interpolating stencil points in the donor or recipient meshes according to the established hierarchical level.

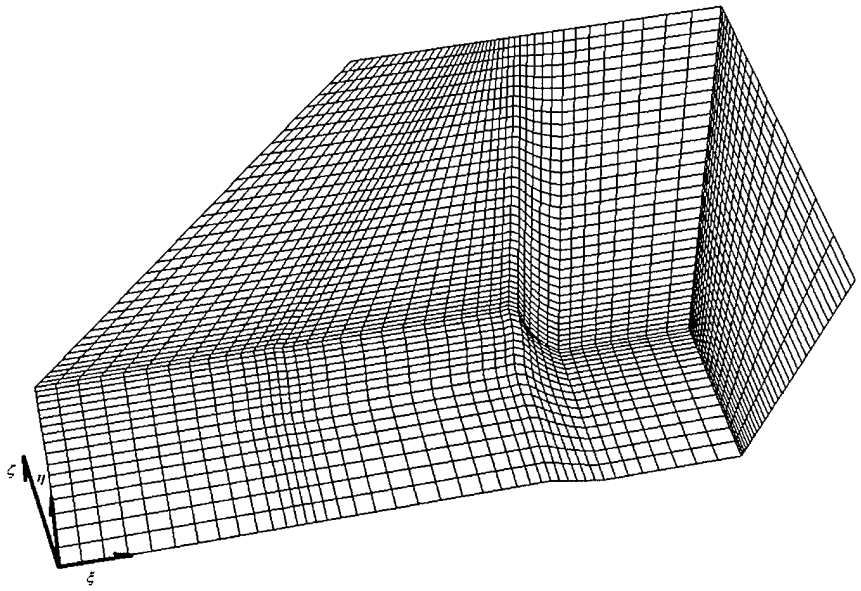

Figure 4-5. Section in the vertical fin mesh demonstrates the topology.

- Mark other special points to be excluded from the computational domain (interior, or orphan points).

At the end of this process, each point in the mesh will be assigned the appropriate status:

- Field point.
- Hole point.
- Boundary (interpolation) point.

- Orphan point.
- Interpolating point.
- Interior point.

The embedding process of the fin mesh into the wing-body mesh requires the creation of a hole in the wing-body mesh to exclude the fin solid volume from the computational domain of the wing-body mesh. A hole-creation boundary defined in the fin mesh cannot be completely closed; a gap must exist at the intersection of the fin surface and the hole-creation boundary (figure 4-7). As a result, some points close to the fuselage surface will be considered unblanked by the *PEGSUS* hole location algorithm (see figure 4-7). This problem can be solved by utilizing the so called *Phantom* mesh, which is a dummy mesh – in the sense that it does not communicate with the other meshes in any way – used only for the hole creation. The hole-creation boundary, shown in figure 4-6, has been used to define the outer boundary of the phantom mesh. However, the lower face of the phantom mesh is extended into the fuselage interior. The geometry of the outer boundaries of the fin and phantom meshes is designed to help capture the interpolating points in the wing-body O-grid. Since the fin mesh is an H-H grid, the fin solid surface should be marked as an interior region in the fin mesh to be excluded from the computational domain with boundary conditions being applied here. The hole in the wing-body mesh is designed in a way to be interpolated on five faces, leaving the lower face for the application of boundary conditions. The same procedure is done for the fin mesh outer boundary, where the boundary conditions are applied on the lower face. A double-fringe is globally applied for the two meshes for better results [51], and to provide the required interpolating stencil points for the 4^{th}-order derivatives of the damping terms in the flow solver. An overlap of approximately five points is kept in the three coordinate directions to satisfy the double–fringe requirement. It is recommended to pick the ζ-coordinate (or K) in the axial direction, since *PEGSUS* is designed to print the MAPS file at constant ζ-planes. Also, it is strongly recommended to do domain inclusion, either globally or

locally, in order to avoid any fault marking of orphan points in the neighborhood of mirror planes (the $z=0$ plane in our case). The user input file, the input mesh format, and the parameter values required to run *PEGSUS 4.0* can be found in Appendix-A. A summary of the *PEGSUS* output is found in Appendix-B, showing no orphan points in the two meshes. Also, the summary of the output contains the parameter values required to run the *fdl3di*-flow solver (Namely IGRID, IIDIM, and IBDIM). A sample of the output maps, showing the layout of some cross-sectional planes in the two meshes, is found in Appendix-B under *Diagnostic Maps.*

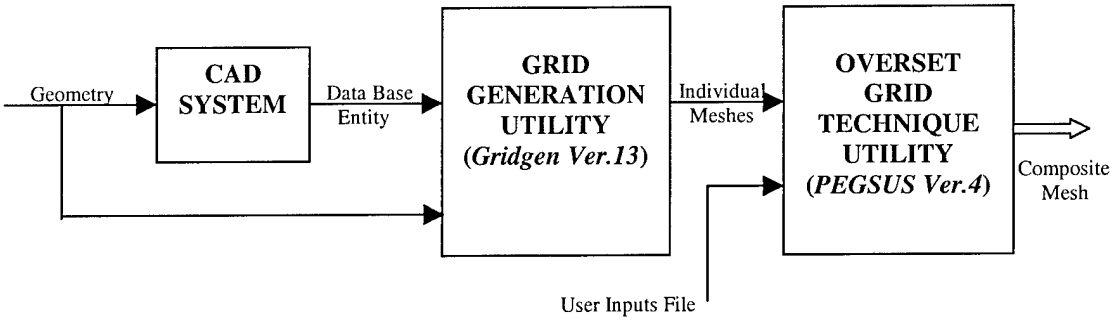

Figure 4-6. Block diagram illustrates the different phases of the grid generation process.

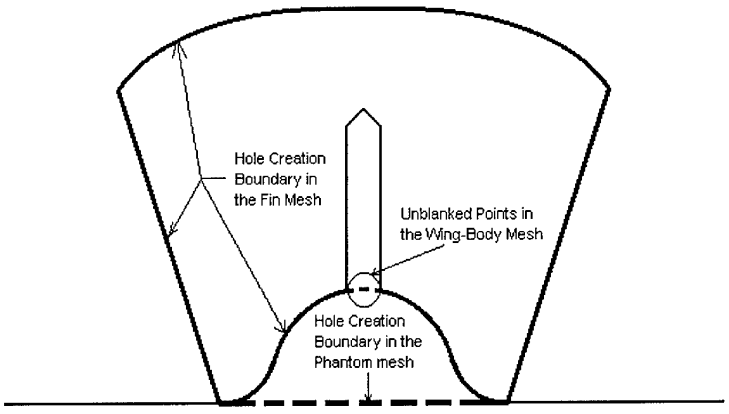

Figure 4-7. The hole-creation boundary.

Chapter-5 Analysis and Results

5.1 Introduction

The main emphasis of this research is to study the effect of adding the sideslip degree-of-freedom (DoF) to the analysis of wing rock onset and characteristics. Since the actual wing rock motion is a combination of roll, sideslip, and vertical descent (much like Dutch-Roll motion, see figure 5-1), all three of these DoF will be included and these three DoF solutions will be compared and contrasted with the single DoF roll-only solutions. Since the vertical fin can produce a considerable amount of the sideslip force, the simulations are conducted for the wing-body configuration with and without the fin to study its effect. All the simulations are conducted for the same initial flight condition (Mach number of 0.4 and pressure altitude of 2000 meters). In all simulations, the wing rock oscillations are triggered from an initial steady level flight due to an initial perturbation in roll rate (p^0) of 0.01 (non-dimensional value).

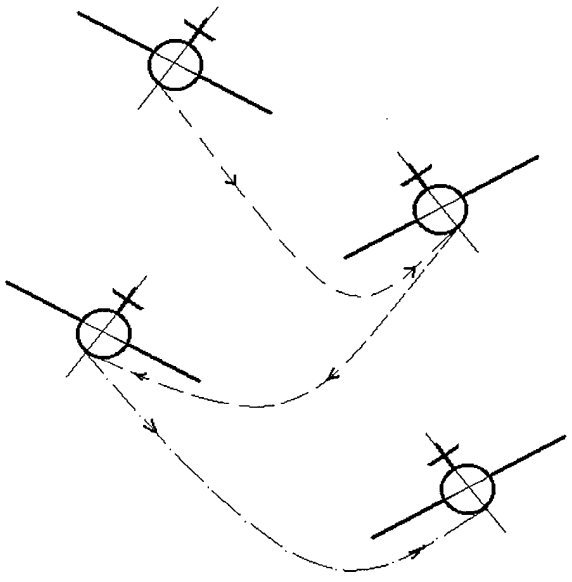

Figure 5-1. Schematic drawing for the wing rock motion.

In the remainder of this Chapter, some interesting phenomenon will be discussed at particular cross-planes. For illustration the axial location of these cross-planes is depicted in figure 5-2.

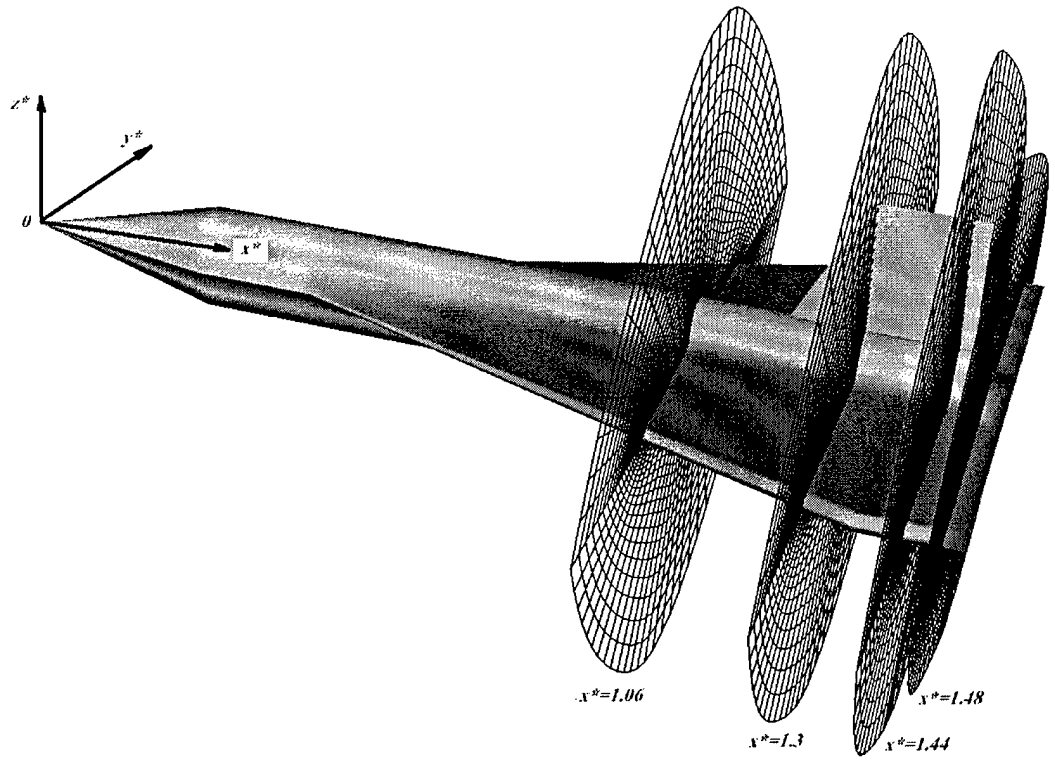

Figure 5-2. Axial location of particular cross-planes.

5.2 Grid Sensitivity Analysis

Three meshes of different dimensions (Table 4-1) were developed to analyze the grid dimension effects on the solution. The developed solutions for the three meshes are compared and analyzed for a sample run. The selected sample was chosen for the three DoF motion, where the dynamics of the motion depends on the computed aerodynamic loads in the three DoF, to maximize the differences in solutions. The simulations were done for an angle of attack ($\alpha = 25^{\circ}$), slightly lower than the expected wing rock onset ($\alpha = 35^{\circ}$). The expected response at $\alpha = 25^{\circ}$ should dampen more rapidly, and hence reduces the cost of the simulation for the three meshes.

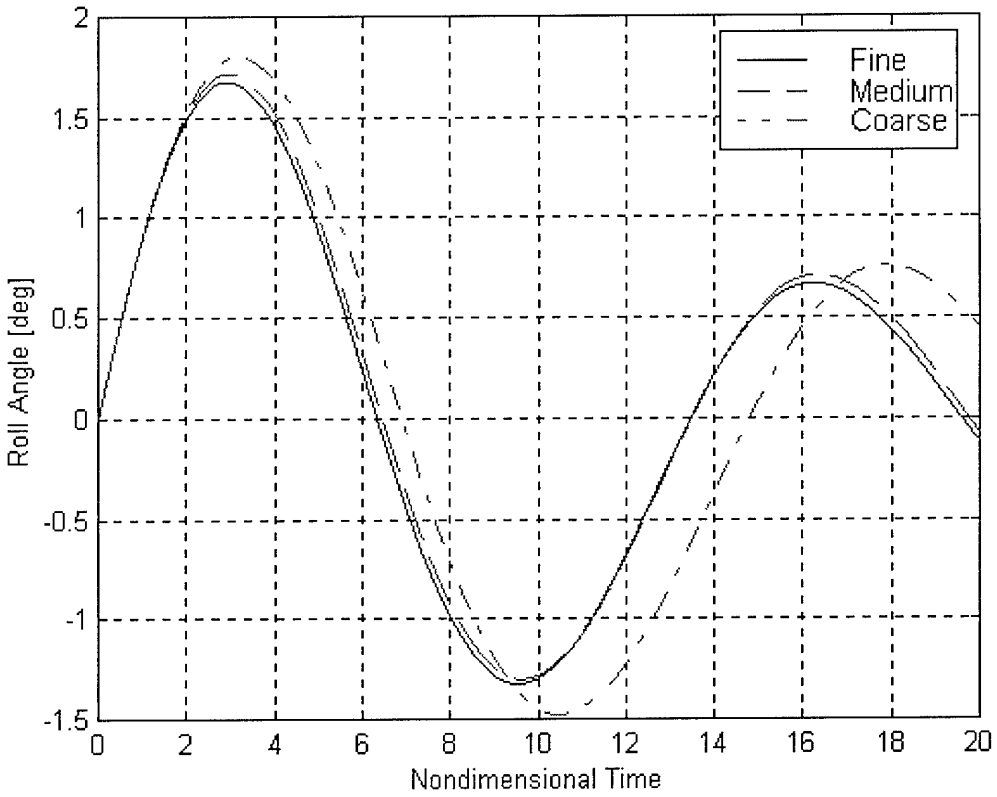

Figure 5-3. Roll angle response for the three meshes at $\alpha = 25^{\circ}$ due to an initial perturbation in roll rate of 0.01.

Figure 5-3 depicts the time-history for the roll angle in response to an initial perturbation in roll rate for the three meshes. The results show a convergence toward the fine mesh solution, with the solution of the medium mesh very close (even identical in some regions) to the fine mesh solution. This supports that the fine mesh is approximately representing a grid-independent solution. The comparison of the solutions developed by the coarse and fine meshes shows similar qualitative behavior for the coarse mesh with a 7% increase in amplitude on average, and a reduction in frequency of 8% on average over the fine mesh. The reason for these differences is the slightly stronger leading edge vortex, which was observed for the fine mesh (figure 5-4) at the initial flight condition (25° angle of attack and zero roll angle). This stronger vortex increases the damping slightly in the solution of the fine mesh over that of the coarse one. Since this research is

primarily concerned with the incremental effects due to adding sideslip and vertical DoF, it was decided that the coarse mesh accuracy was adequate for this purpose. Consequently, to save computational cost the majority of the simulations were conducted on the coarsest mesh.

5.3 Simulations of Wing Rock for the Wing-Body Configuration

The geometry of the wing-body configuration is demonstrated in detail in section 4.1, which represents the generic fighter model without a fin.

5.3.1 Single Degree-of-Freedom in Roll. To begin the research, an initial guess for the onset angle of attack was determined from a previously published wing rock boundary versus aspect ratio [27:733]. The boundary in figure 5-5 was established from the observations for a delta wing undergoing wing rock in roll only. Although the model in this case is a blended wing-body configuration, the predicted onset based on this curve should be in the neighborhood of the actual onset value. The model aspect ratio is 1.29, which from figure 5-5 corresponds to an onset of 33 degrees in angle of attack. Also the observations in [27] indicate that the wing rock is likely to be triggered and driven by asymmetric vortex bursting, and not by asymmetric vortex shedding. The 33-degrees angle of attack was run for a couple of cycles, and didn't lead to a limit cycle oscillation. Next a 35- degrees angle of attack was tried and successfully led to a limit cycle oscillation in roll (figure 5-6). Approximately 16 degrees peak-to-peak amplitude in roll angle is observed with an interesting limit cycle phase-plane portrait (figure 5-7).

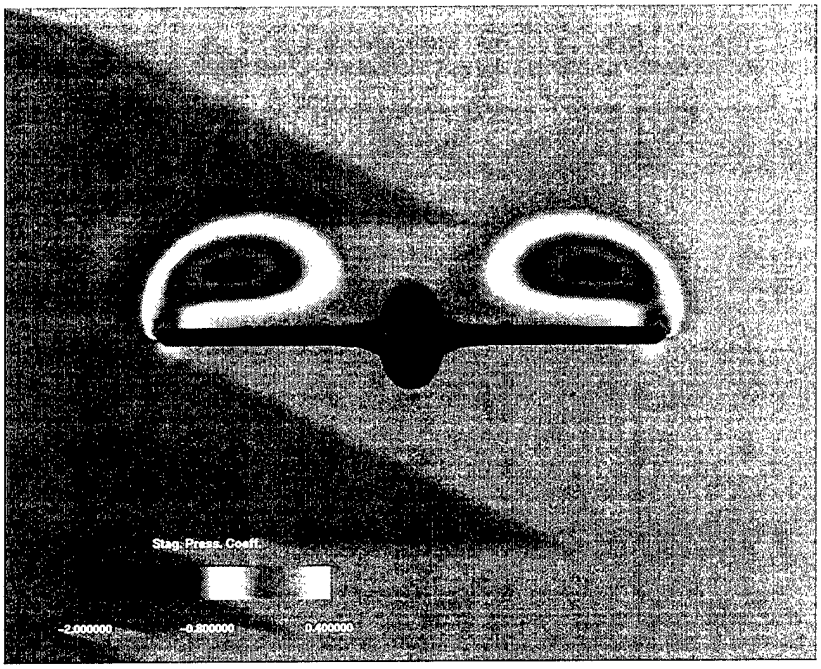

(a) Coarse Mesh

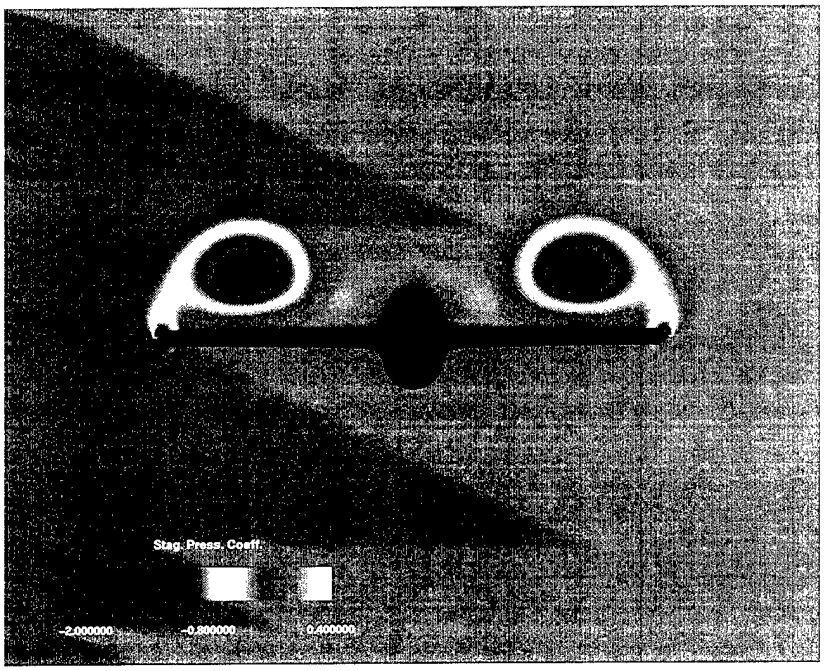

(b) Fine Mesh

Figure 5-4. Stagnation pressure distribution at $\alpha = 25^{\circ}$ for a cross-plane at x^{*}=1.3.

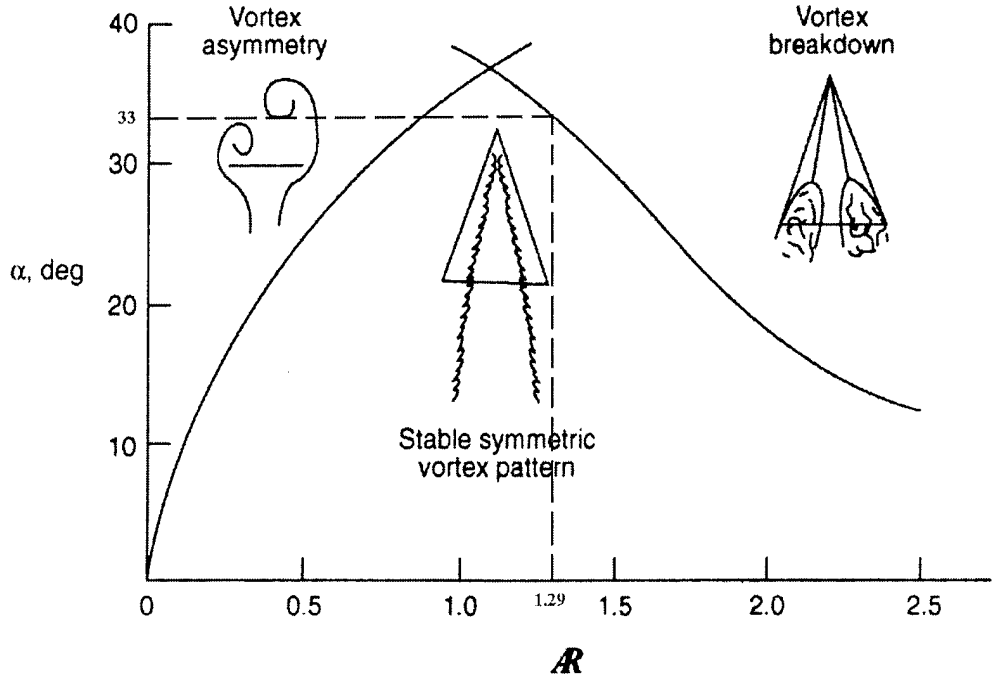

Figure 5-5. Wing rock boundary versus aspect ratio [27:733].

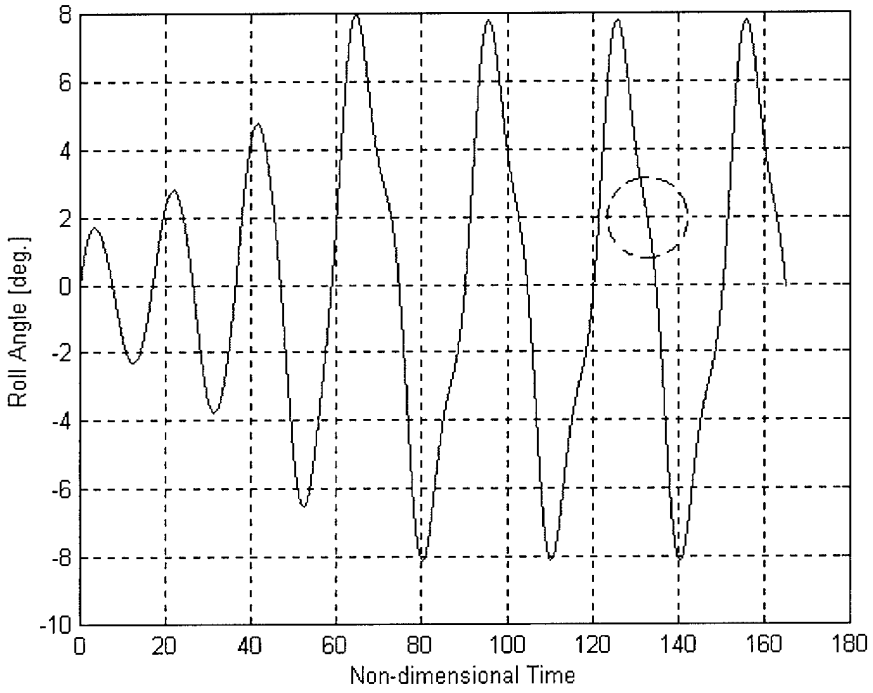

Figure 5-6. Limit cycle oscillations in roll for the wing-body configuration at $\alpha = 35^{\circ}$.

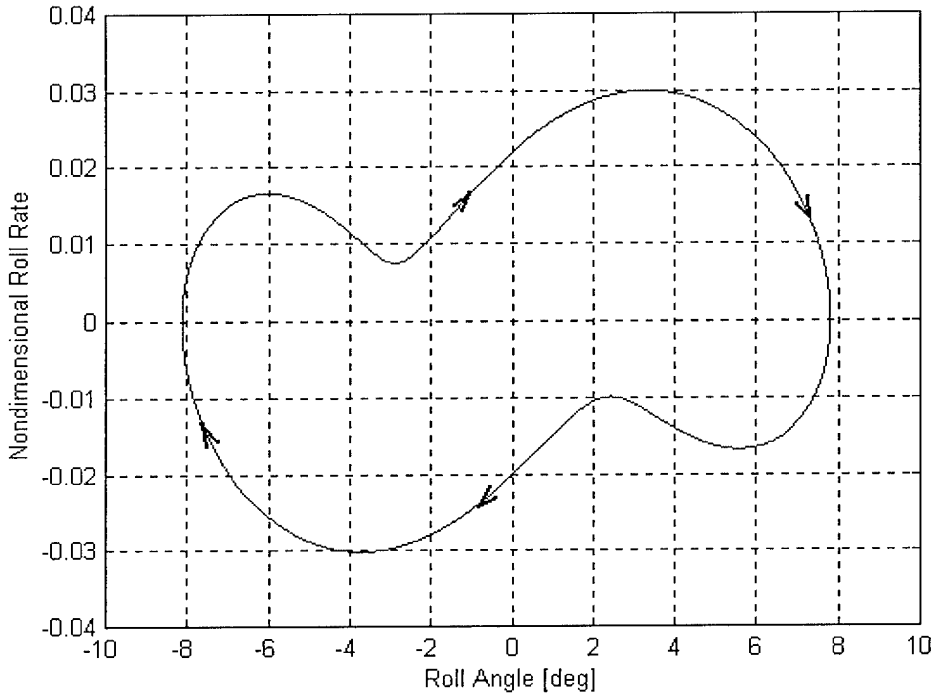

Figure 5-7. The phase-plane portrait for a full limit cycle in roll.

The relatively low-amplitude of the wing rock oscillation was actually not surprising, the previous work of Brandon and Nguyen [4:3] on a chine fore-body mounted on a 26°-sweep trapezoidal wing found oscillations of approximately 12° amplitude (see figure 1-3). A rapid rolling rate was observed in the neighborhood of the zero-roll angle position (look at the little circled kink in figure 5-6). Surprisingly, this little kink in the roll angle response has been observed in the flight test data of wing rock for realistic fighters. The closest configuration to the generic fighter model geometry, for which wing rock flight test data is available, is the F-4 fighter aircraft [23] (figure 5-8). The recorded flight test data for the F-4 wing rock [43:6-13], shows a similar roll angle response (figure 5-9) to that of the generic fighter model (figure 5-6).

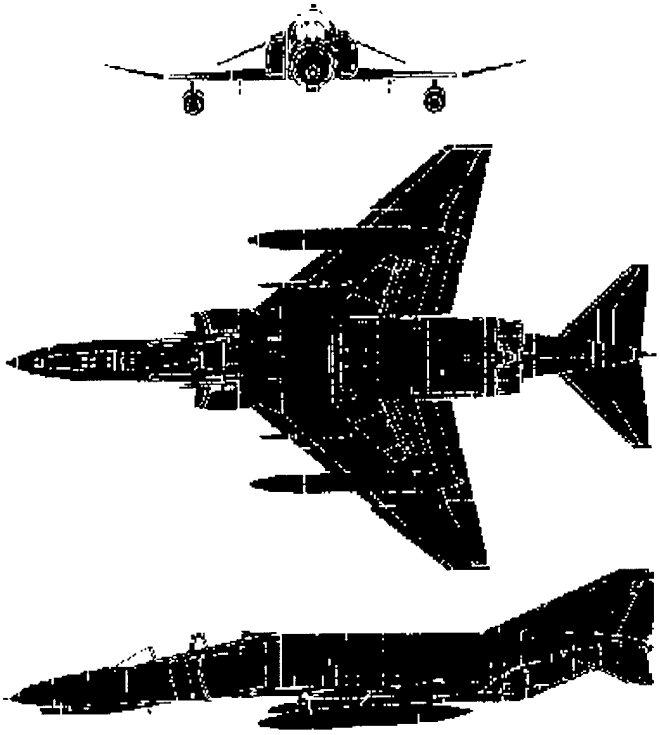

Figure 5-8 Three-view drawing for the F-4 [23].

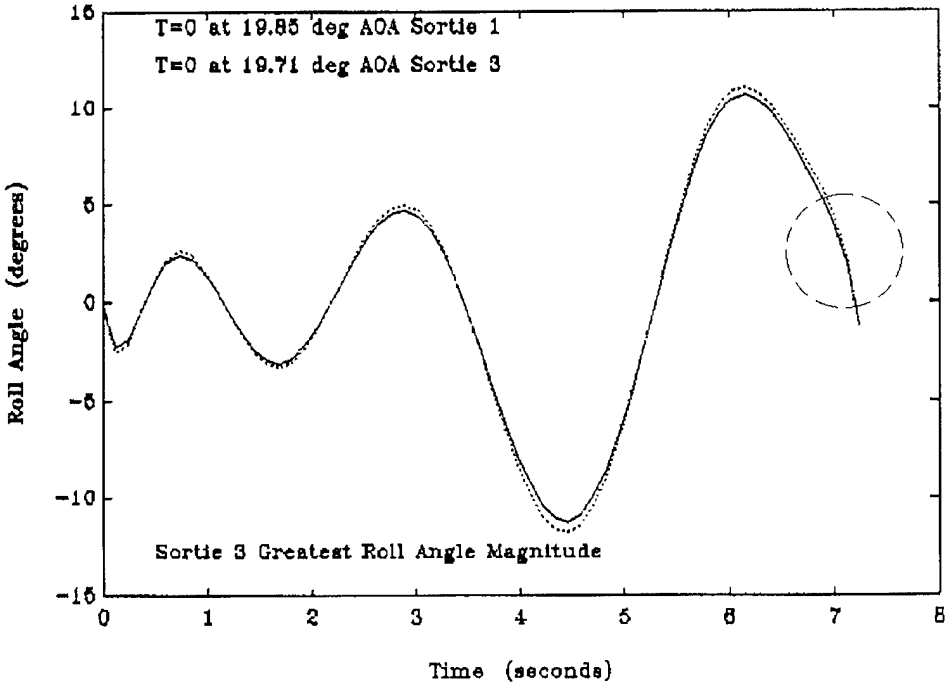

Figure 5-9 Roll angle response following the onset of wing rock for the F-4 [43:6-13].

In order to explain the fluid mechanism that drives the observed wing-body rock in this study, two main phenomena, the vortex burst and vortex dynamics, should be investigated throughout a full cycle of wing rock.

The instantaneous axial location of vortex burst was traced by searching the first occurrence of a negative axial velocity on the upper surface of the two wing halves. The instantaneous axial locations of vortex burst captured by the searching algorithm within an entire cycle of wing rock are depicted in figure 5-10. In order to verify the instantaneous axial locations of vortex burst captured by the searching algorithm, mass-less particles were injected near the tips of the leeward side of the body. The traced trajectories of the particles at the initial conditions ($\alpha = 35^{o}$, $\varphi = 0^{o}$) showed a flow reversal (see figure 5-11) at approximately the same predicted location from the numerical algorithm (x^{*}=1.032).

In order to explain the vortex burst dynamics depicted in figure 5-10, let us assume the model is rolling in the positive direction. Then at a positive roll angle, the axial location of vortex burst on the left wing (which moves upward) moves downstream, while that on the right wing (which moves downward) is moving upstream. In the light of this behavior of the asymmetric vortex burst location, one can explain its role in driving the oscillations. Once the model is initially perturbed in roll rate, it starts to oscillate around the zero-roll angle position. The upward-moving wing is exposed to a down wash, which reduces the instantaneous value of angle of attack on this wing and hence delays vortex burst (i.e. the first occurrence of vortex burst moves downstream). On the other hand, the downward-moving wing is exposed to an up wash, which increases the instantaneous value of angle of attack on this wing, and hence promotes vortex burst on this wing (i.e. the first occurrence of vortex burst moves upstream). As a result, the lift is increased on the upward-moving wing and reduced on the downward-moving wing. So far, this model should go into a divergent rolling motion in the absence of a restoring moment. However, the effect of the variation of vortex structure and location (vortex dynamics) still need to be investigated to reach a complete understanding of the physics of the motion. The vortex

dynamics was visualized in this study through snap shots of the instantaneous stagnation pressure coefficient distribution for a cross-plane at $x^* = 1.06$ (see figure 5-12). As shown in figure 5-12, the vortex on the upward-moving wing becomes more coherent and moves slightly away of the surface, so its footprint on the surface is reduced (see figure 5-13 (b)). While the vortex on the downward moving wing is diffused and slightly moves toward the surface, so its footprint on the surface is increased (see figure 5-13 (b)). As a result, the lift is reduced on the upward-moving wing and increased on the downward-moving wing, which establishes the restoring moment. Figure 5-13 (a) shows the symmetric suction on the wing upper surface at the initial conditions ($\alpha = 35^\circ$, $\varphi = 0^\circ$), while figure 5-13 (b) shows an asymmetric suction on the wing upper surface at a roll angle of 8° due to vortex dynamics. The effect of vortex dynamics during wing-body rock is counter-balancing the effect of the asymmetric vortex burst location, which sustains the wing rock oscillation.

In summary, the vortex burst dynamics is found to produce the driving moment of the motion for small roll angles, where the asymmetry in vortex structure and location is not significant. As the rolling continues, the rolling angle increases and the asymmetries in vortex structure and location becomes significant, and hence the restoring moment increases. At a finite roll angle, the restoring moment becomes sufficiently strong to stop rolling and even reverses the direction of roll afterwards.

Based on the previous explanation of the fluid mechanism that drives wing rock, tangential blowing on the upper surface to enhance vortex burst is suggested for wing rock delay or suppression. Forebody vortex control has been studied for a similar model consisting of: forebody of circular cross-section, sharp delta wing of 78°-sweep, and vertical fin [41]. The reported results showed that steady tangential blowing from leeward nozzles near the forebody tips was capable of suppressing wing rock [41:303].

The previous discussion explains the interesting shape of the limit cycle (figure 5-7) due to the rapid increase in roll rate in the neighborhood of the zero-roll angle position. Since the asymmetries in vortex structure and location in the neighborhood of the zero-roll angle position are not significant, the asymmetric vortex burst location is dominantly driving the motion. This also explains the switch in the sign of the roll stiffness derivative $C_{l\varphi}$ from negative to positive as the model passes points (A) and (B) (see figure 5-14).

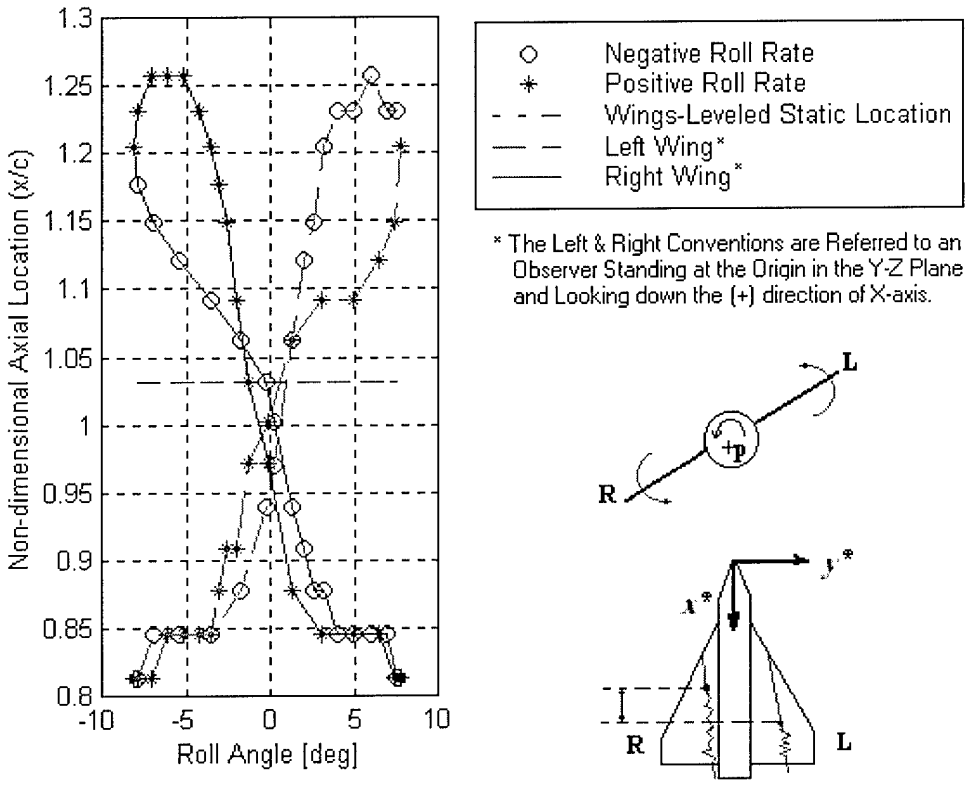

Figure 5-10. Instantaneous vortex burst locations during an entire cycle of roll oscillations at $\alpha = 35^{\circ}$.

Figure 5-10 shows large hysteresis associated with the vortex burst location on both wing halves. This hysteresis is observed on the wing-half only if it is in the leeward side of the wind. Even though the model discussed here does not have sideslipping body motion, there is still a kinematically induced sideslip. Since the model is rolling about the body-fixed x-axis, the angle of attack and sideslip are mutually interchanging during rolling as follows:

$$\tan \beta = \tan \alpha_o \sin \varphi \qquad (5\text{-}1)$$

Where:

β = Sideslip angle due to kinematic-coupling.

α_o = Angle of attack (wings-leveled).

φ = Roll angle.

At a positive roll angle the sideslip is positive and hence the left wing is in the leeward side of wind. Similarly at a negative roll angle, the sideslip is negative and hence the right wing is in the leeward side of wind. The hysteresis associated with the instantaneous vortex burst location (figure 5-10) is only observed on the upward-moving wing due to the time-lag of the vortex motion.

5.3.2 Three Degrees-of-Freedom Wing Rock. The previous simulation of wing rock for the wing-body configuration with a single DoF in roll at $\alpha = 35^\circ$ is next repeated for the three DoF: roll, sideslip, and vertical descent. The simulation shows the response starts divergent, and damps out nicely after the first cycle (see figure 5-15). This result indicates that adding the sideslip DoF increases the damping of the motion in general and hence delays the onset. However, the simulation should be conducted to a higher value of angle of attack to confirm whether the system would go into a limit cycle or not at all. Raising the angle of attack above the onset ($\alpha = 35^\circ$) one degree at a time is computationally costly (at least 3-4 cycles are needed to capture a limit cycle), so the angle of attack was raised by 5°. The simulation was repeated for $\alpha = 40^\circ$ for the same initial conditions ($p^0 = .01$), and now achieves a limit cycle (figure 5-16). This result concludes that adding the sideslip DoF delays the onset of wing rock in general, however this doesn't mean that the onset was delayed by 5°, since the angles between 35° and 40° have not been tested. Comparing figures 5-6 and 5-16 one can see that the amplitude of the oscillations was reduced by approximately 50% over the single DoF case.

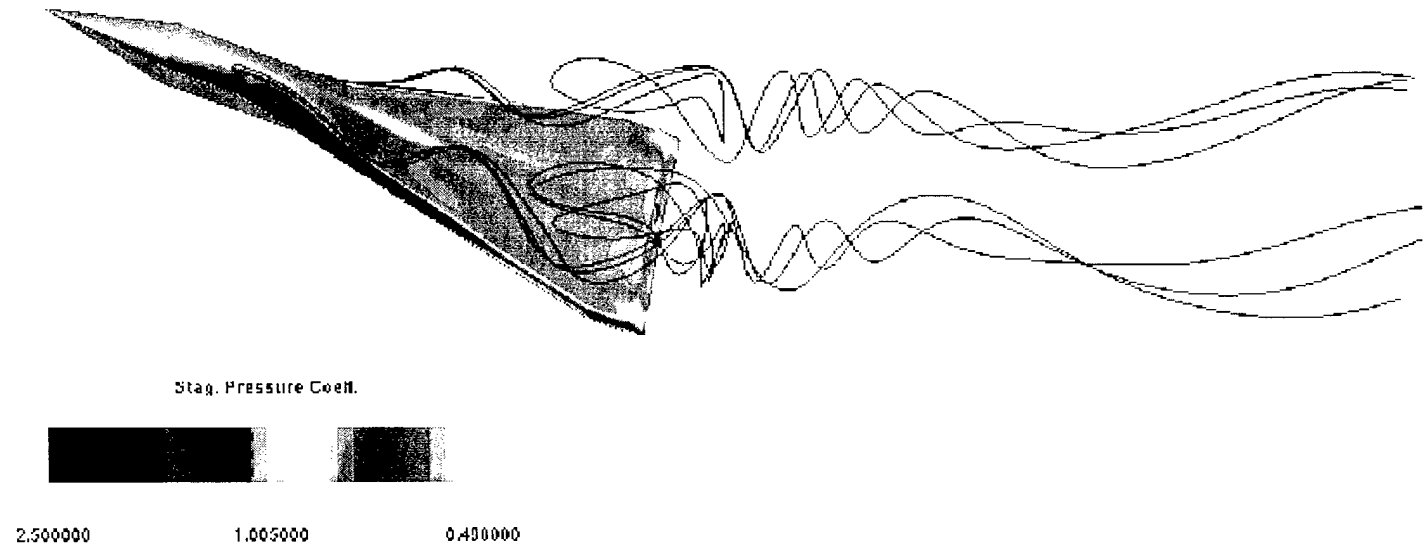

Figure 5-11 Particle path trajectories at 35 degree AoA. and zero roll angle

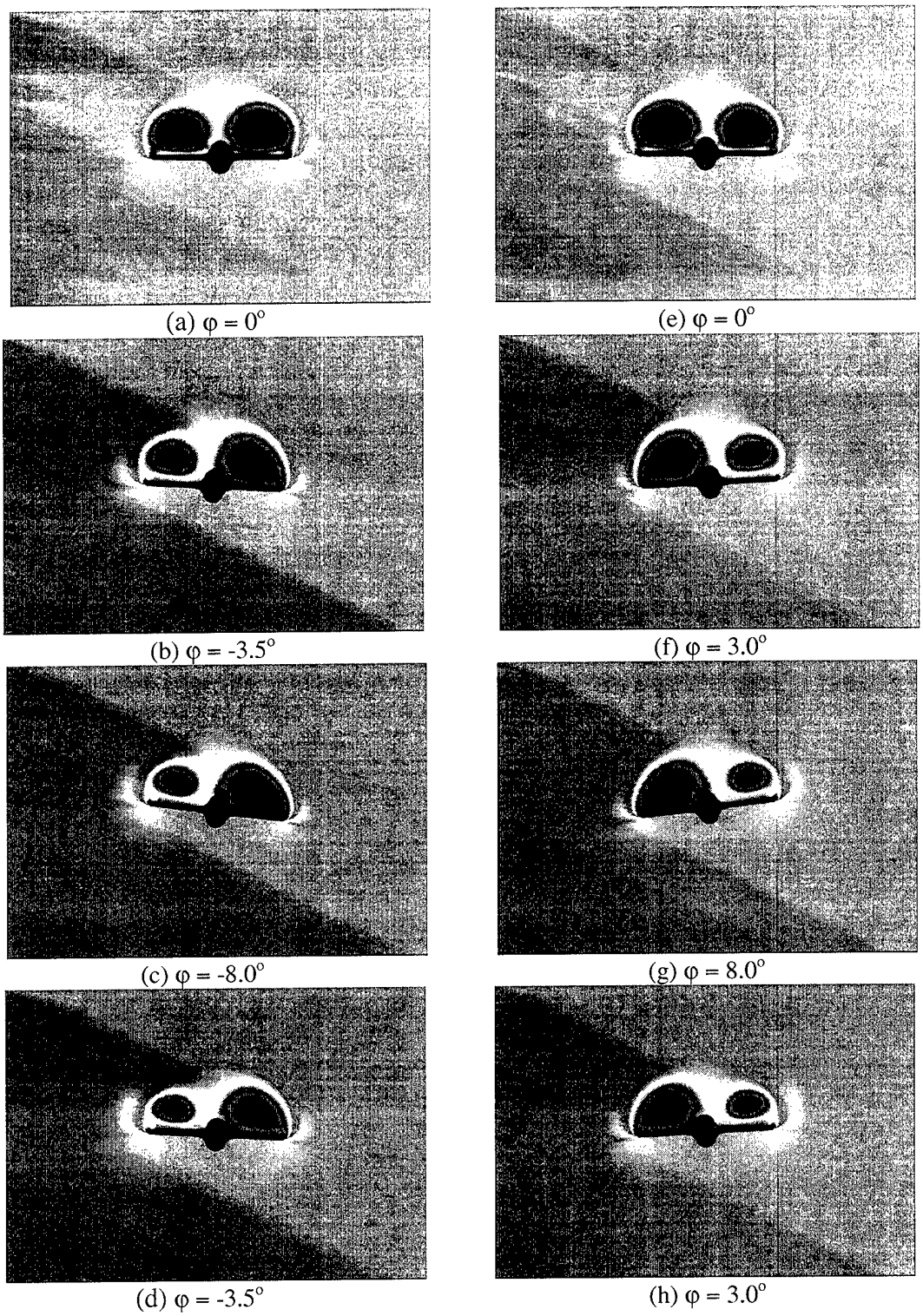

Figure 5-12. Vortex dynamics during a full limit cycle in roll at $\alpha = 35^{\circ}$.

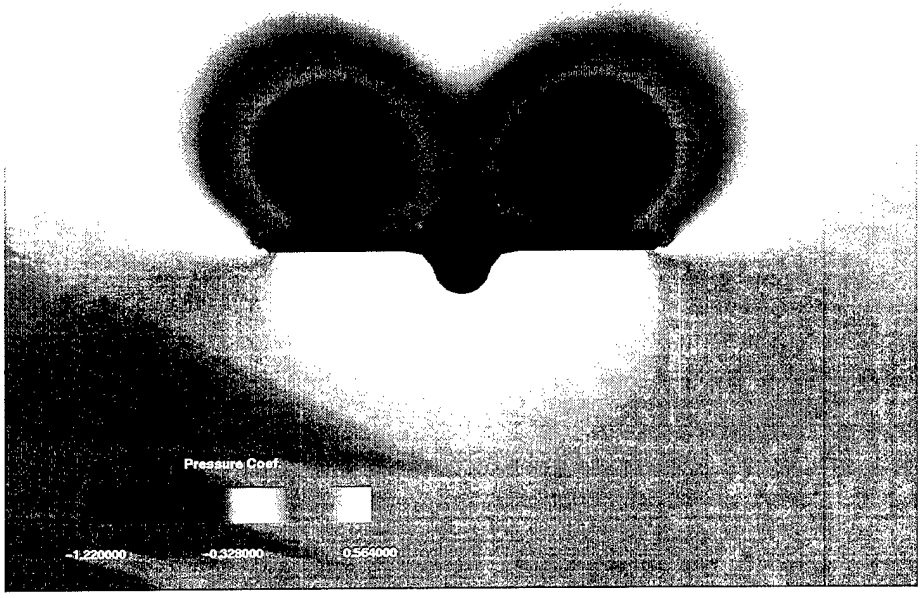

(a) $\varphi = 0^{o}$

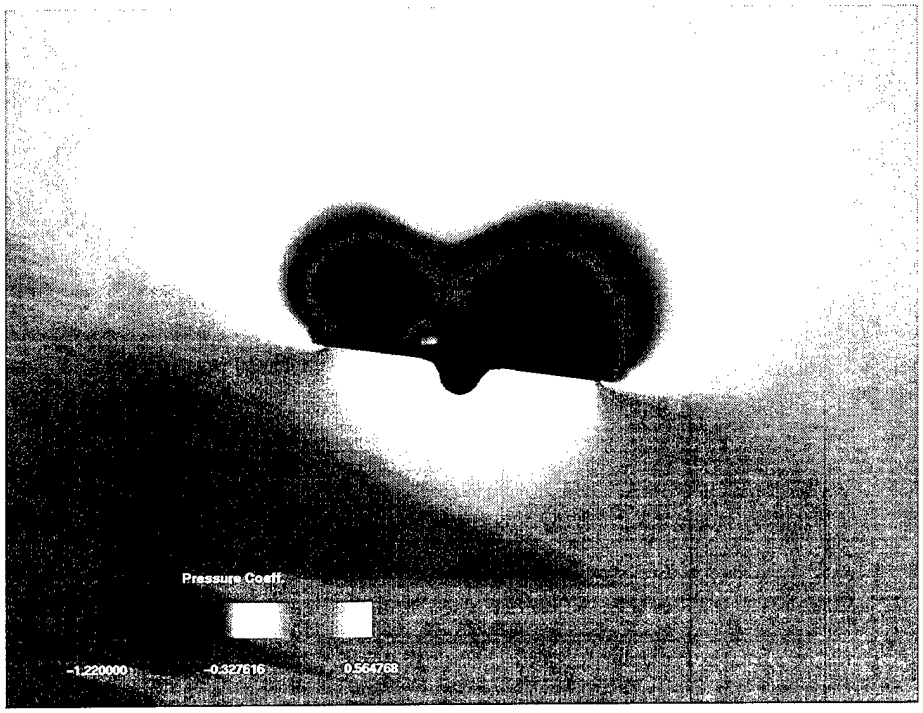

(b) $\varphi = 8^{o}$

Figure 5-13. Pressure coefficient distribution at $\alpha = 35^{o}$ for a cross-section at x^{*}=1.06.

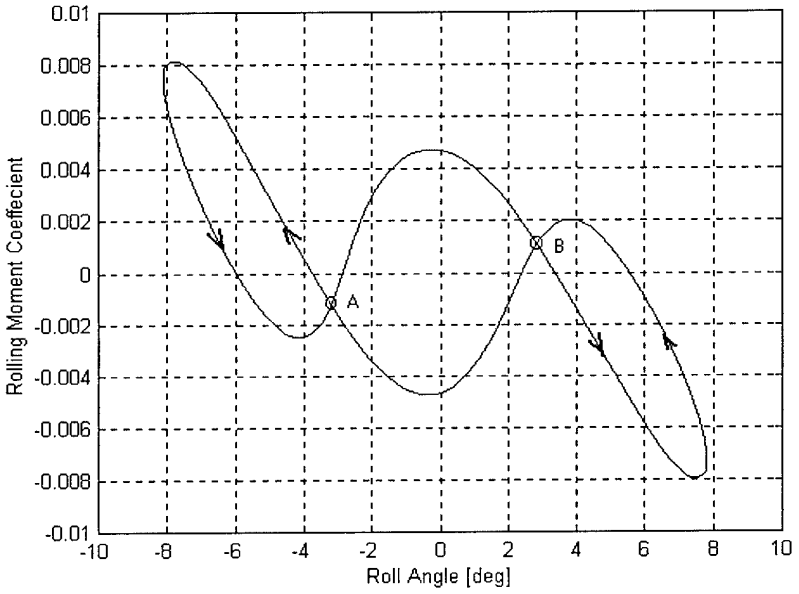

Figure 5-14. Variations of rolling moment coefficient versus roll angle for a full limit cycle in roll.

An aircraft in a rolling motion about its body-fixed longitudinal axis is subjected to sideslip due to two different sources, one from the kinematic-coupling of the angle of attack and sideslip (equation 5-1) and the other from the dynamics of the body's sideward motion (i.e. kinetics). The sideslip due to the kinematic-coupling is in phase with the motion as shown in figure 5-17, while the sideslip due to kinetics lags the motion. Figure 5-17 shows an approximately 90° phase-lag between the rolling and sideslip due to kinetics. This 90° phase-lag is a source of adverse sideslip motion during rolling, which has the effect of reducing the vortex lift-off distance on the upward-moving wing and hence reducing the amplitude of the oscillations. In addition, this adverse sideslip has the effect of reducing the hysteresis associated with the instantaneous vortex burst location (figure 5-18) compared with the case for the single DoF (figure 5-10).

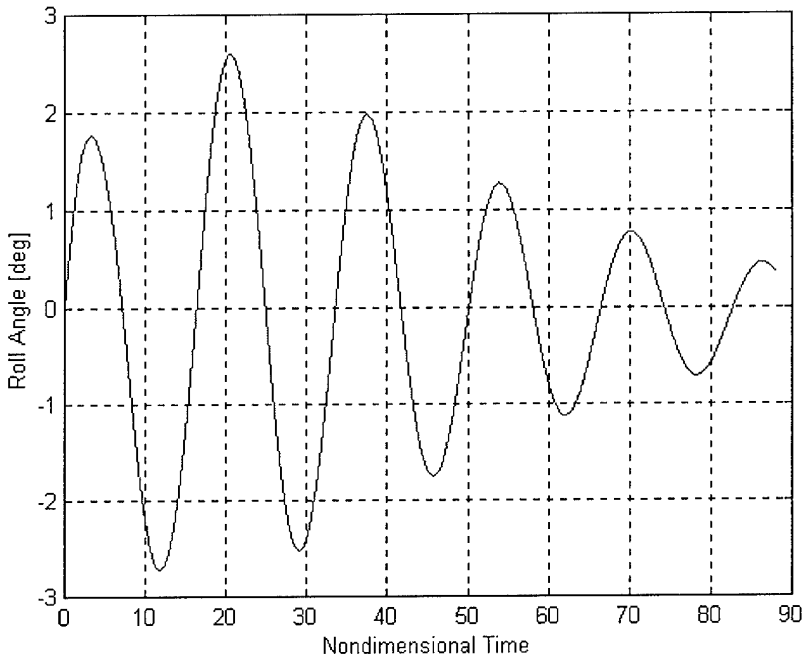

Figure 5-15. Roll angle response to an initial roll rate of 0.01 at $\alpha = 35^{\circ}$ for the case of three DoF motion.

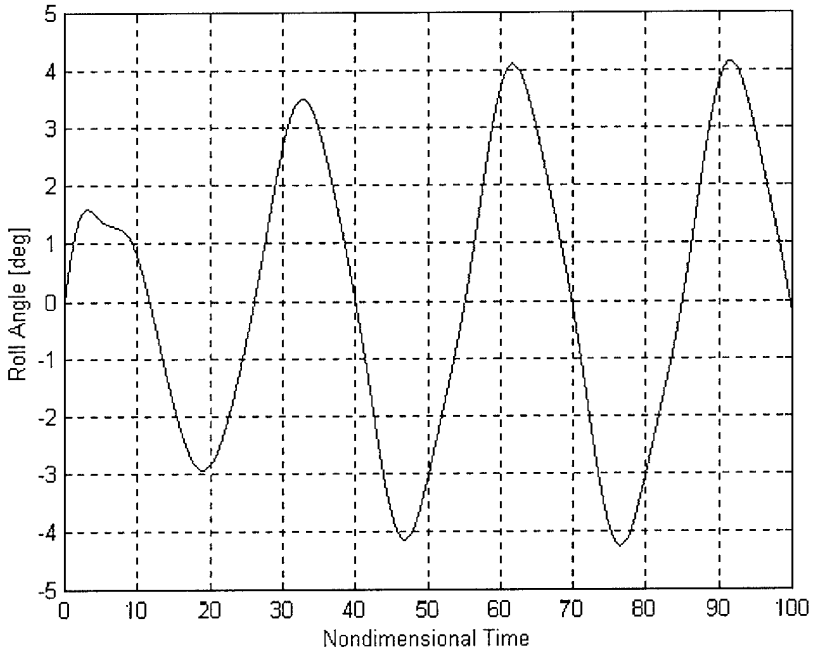

Figure 5-16. Roll angle response to an initial roll rate of 0.01 at $\alpha = 40^{\circ}$ for the case of three DoF motion.

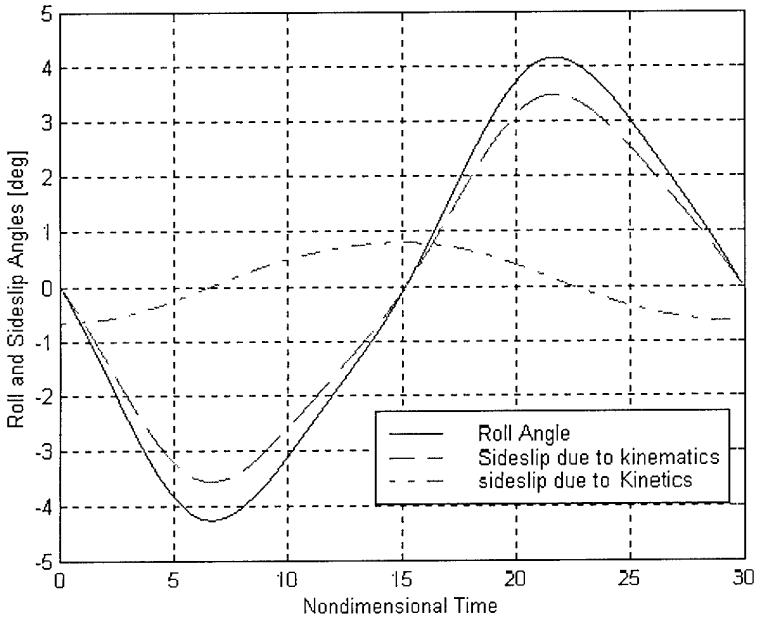

Figure 5-17. Roll and sideslip angles time-histories for an entire cycle of wing rock at $\alpha = 40^{\circ}$ for the case of three DoF motion.

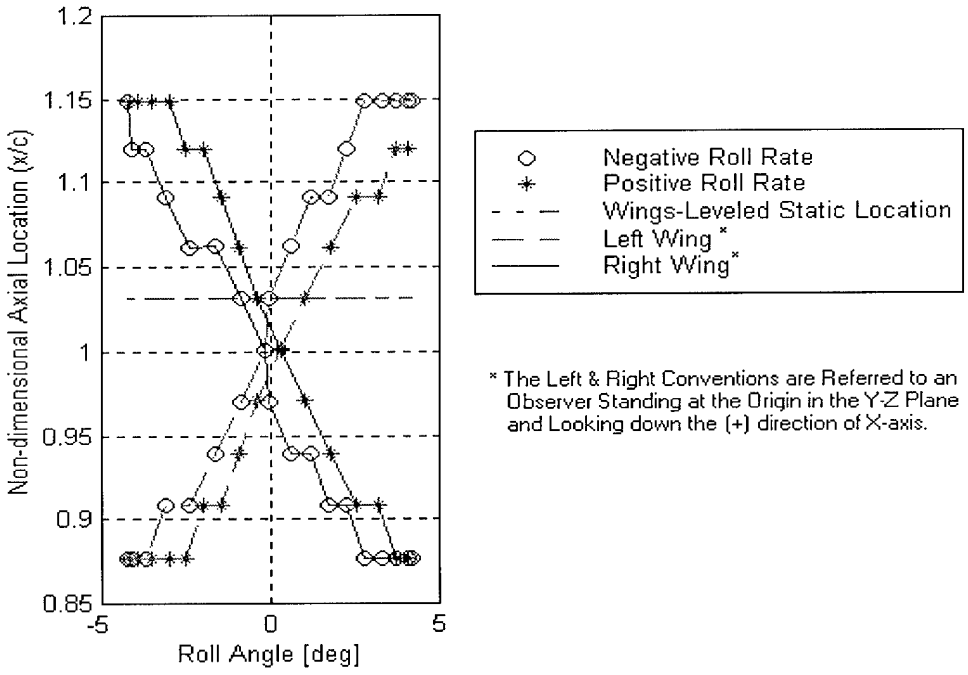

Figure 5-18. Instantaneous vortex burst locations during an entire cycle of the three DoF oscillations at $\alpha = 40^{\circ}$.

Previously, it has been shown that the static lateral stability derivative C_{l_β} (known as the dihedral derivative) can significantly influence the onset of wing rock [33,34,35,48]. The dihedral derivative (as are all stability derivatives) is determined at a certain angle of attack by measuring the value of the rolling moment coefficient for several static sideslip angles and then computing the derivative from this data. Due to computational costs, only dynamic simulations were performed for the present research. However, one can look at a pseudo stability derivative for the dynamic case from:

$$C_{l_\beta} = \frac{\partial C_l}{\partial \beta}$$

$$= \frac{\frac{\partial C_l}{\partial t}}{\frac{\partial \beta}{\partial t}}$$

Where:

C_l = Rolling moment coefficient.

β = Sideslip angle (sum of kinematic-coupling plus kinetic motion) [rad].

The derivative was numerically computed by a second order accurate central difference scheme from the recorded data for a full cycle of wing rock in three DoF. The computed C_{l_β} was then filtered through a low-pass filter to suppress the high frequency noise associated with the numerical scheme. Figure 5-19 shows the raw and filtered data. The mean value of C_{l_β} over a full cycle was calculated to be -0.0591 [rad^{-1}]. This concludes that during a fully developed wing rock oscillations, the mean value of the dihedral derivative is strongly stable. This contradicts the results of reference [48], where it was shown for the F-15 that C_{l_β} is approximately zero at the onset of wing rock. It remains to be seen whether this pseudo stability derivative is an accurate reflection of the true static definition. Further numerical static simulations would have to be performed.

5.4 Simulations of Wing Rock for the Full Generic Fighter Model

The fin can produce a considerable amount of the side force, so its effect on the three DoF simulations needs to be examined. A finite-thickness trapezoidal fin of moderate fin-to-wing area ratio of 0.08 was used. The simulation of wing rock at $\alpha = 35^{o}$ was repeated for the generic fighter model including the fin. The results show an increase in the damping and frequency of the oscillations (figure 5-20). However, this result is limited to the fin geometry used in this study, since the effect of a fin is greatly dependent upon its geometry and its area ratio [37:500]. The analysis reported in [41:301,4:3], for the case of single DoF in roll, shows that fins of relatively small area ratios have the effect of delaying the onset and reducing the amplitude of wing rock. Also it has been reported that fins of large area ratios are likely to get separated and produce an opposite effect [41:301]. The three DoF simulation of wing rock including the fin shows a significant increase in frequency (figure 5-20). This has not been reported for most of the fin configurations in literature for the case of single DoF roll only wing rock. Only one double fin configuration has shown a similar effect for the single DoF in roll [37:500]. A trapezoidal plane-form of area ratio .005 led to an increase in frequency of 36%, and significant reduction in wing rock amplitude [37:500].

The fin has two main contributions, one due to the aerodynamic interaction between the fin surface and the flow over the wing-body, and the other due to the side force produced by the fin. The main observed aerodynamic effect of the fin was the significant delay of vortex burst. The instantaneous location of vortex burst was determined using the same criterion that was previously explained in subsection 5.3.1. Figure 5-21 shows that the vortex burst location at $\alpha = 35^{o}$ for the model with fin was first observed at $x^{*} = 1.48$, just downstream of the fin trailing edge compared with $x^{*} = 1.03$ for the model without fin. Figure 5-22 shows the non-dimensional axial velocity distribution at $x^{*} = 1.44$ (slightly before the fin trailing edge), which shows a positive minimum axial velocity. So vortex bursting has not been observed upstream of the trailing edge

of the fin at $\alpha = 35^{\circ}$. Since vortex burst dynamics produces the driving moment for the oscillations, the oscillations damped out more rapidly with the addition of the fin.

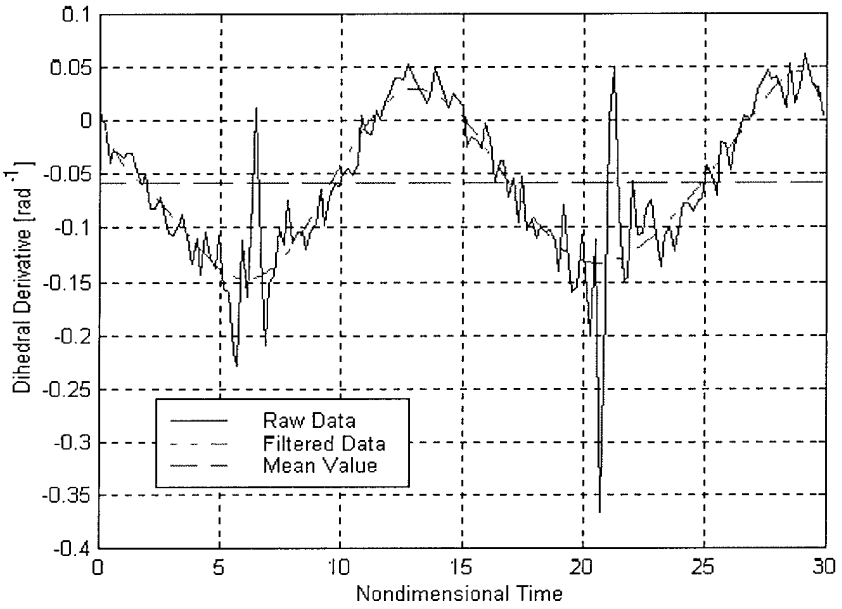

Figure 5-19. Time variation of the dihedral derivative during a three DoF wing rock.

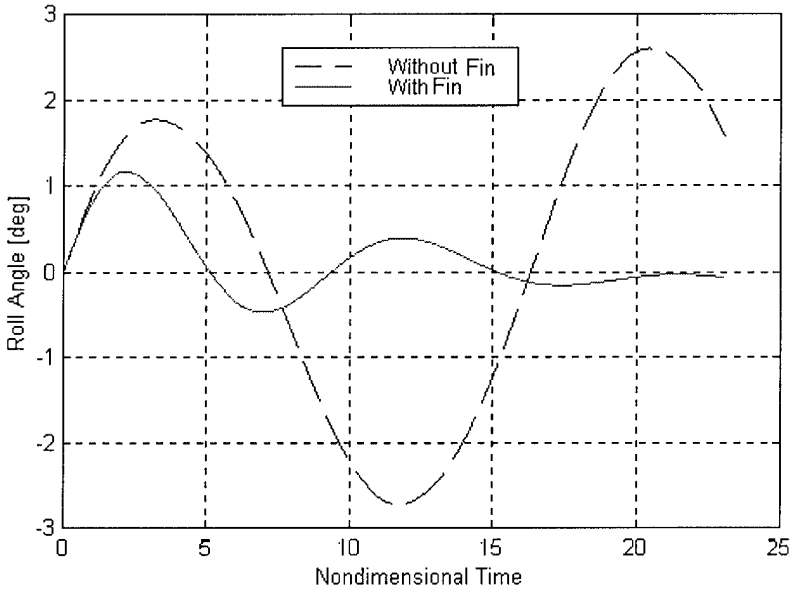

Figure 5-20. Roll angle response to an initial roll rate of 0.01 at $\alpha = 35^{\circ}$ in three DoF for the model with and without vertical fin.

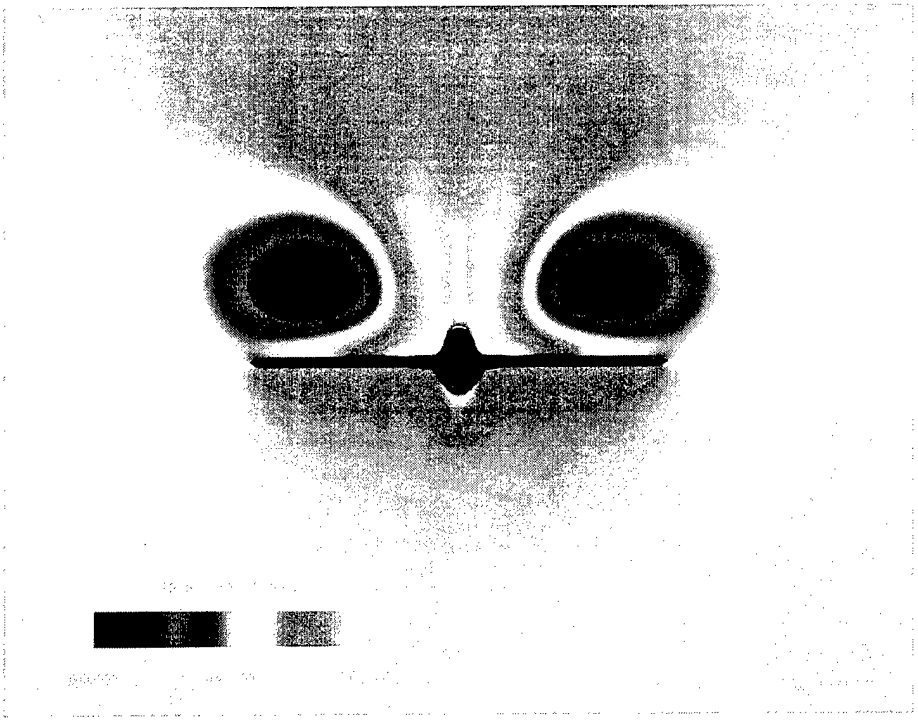

Figure 5.21 Cross-plane axial velocity distribution at $x^* = 1.48$ for the generic fighter at $\alpha = 35^\circ$.

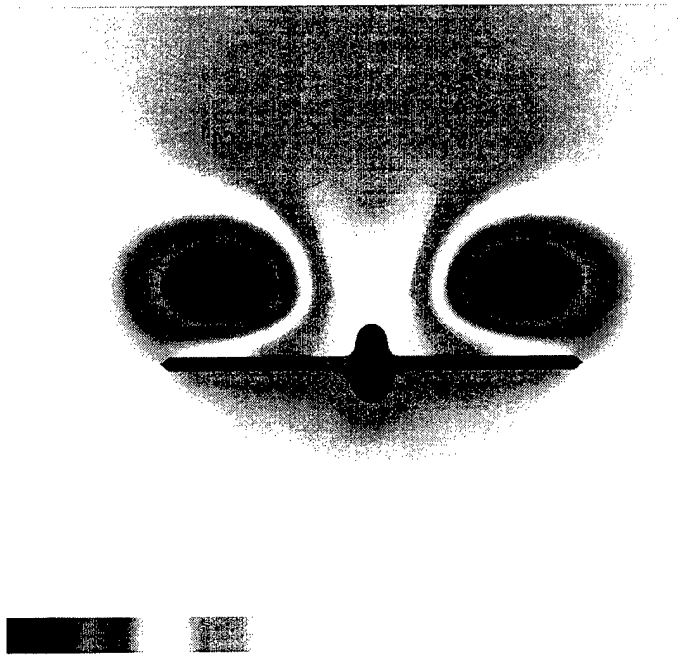

Figure 5.22 Cross-plane axial velocity distribution at $x^* = 1.44$ for the generic fighter at $\alpha = 35^\circ$.

5.5 Computational Cost

The *CPU*-time for the diagonalized-Euler version of the modified *fdl3di*-code for the case of three DoF is approximately 2.51 μs/grid-point/sub-iteration on the *CRAY-T94* supercomputer. Negligible difference was observed between the computational cost for the case of single DoF in roll and that for the case of three DoF. The reason is that the computational cost of solving the rigid-body dynamics equations is negligible compared with the cost of solving the flow governing equations. This fact motivates conducting the computational simulations of wing rock in three DoF rather than single DoF for better accuracy.

Chapter-6 Conclusions and Recommendations

In the present study, the lateral limit cycle oscillation phenomenon known as wing rock has been analyzed in single and three degrees-of-freedom (DoF) for a generic fighter model with and without a vertical fin.

The results for the model without fin in single DoF in roll showed a wing rock onset at $\alpha = 35^{\circ}$ with several interesting phenomena. A roll amplitude of 16° (peak-to-peak) was observed, which confirms the early results [4] on a similar model. The dynamic-aerodynamic interactions during the motion were thoroughly investigated by analyzing the snap shots taken for the flowfield at specific time intervals and tracing the instantaneous location of vortex burst on both wing halves for an entire cycle. The vortex burst dynamics during the motion was found to produce the driving moment, while the vortex dynamics (lift-off) near the peaks of the oscillations on the upward-moving wing half restores the motion.

For comparison with the single DoF in roll simulations, simulations were conducted in three DoF: roll, sideslip, and vertical motion. The purpose of the three DoF simulations was to study the effect of the sideslip dynamics on the onset and limit cycle characteristics of wing rock. The results on the model without fin demonstrated a delay in the onset and a high reduction (approximately 50%) in the amplitude of the oscillations with surprisingly no change in frequency. The associated sideslip kinetics was found to lag the rolling motion by 90° during the fully developed wing rock oscillations. This adverse sideslip motion was found to be the source of this augmentation in damping and delay in onset. Also, the mean value of a pseudo dihedral derivative during a full cycle of oscillation was found to be clearly stable (-.0591), which contradicts previously reported F-15 results [48].

The effect of the vertical fin on the onset and characteristics of wing rock in three degrees-of-freedom was found similar to the results reported in [4,37,41] for the case of single degree-of-

freedom in roll. The vertical fin was observed to greatly affect the frequency for the case of three DoF wing rock, while no appreciable change in frequency was observed for the case of single DoF roll only wing rock. The present research shows that the vertical fin enhances the vortex burst on the wing by delaying its location downstream of the fin trailing edge and hence preserves the flow energy on the wing.

In summary, the following conclusions can be drawn concerning wing rock for the generic fighter model described earlier:

- The analysis of the wing rock motion for a full cycle showed that the vortex burst dynamics is the source of the driving moment that sustains the motion, while the vortex lift-off on the up-ward moving wing creates the restoring moment.
- In computational simulations, the sideward and vertical DoF should be included to get an accurate prediction of the wing rock onset and limit cycle characteristics. Especially, as previously mentioned in section 5.5, the computational cost of including the other two DoF is negligible. However, the predicted values for the single DoF in roll only were found to be conservative (i.e. earlier onset prediction and larger amplitude limit cycle characteristics).
- The computed value of the mean pseudo dihedral derivative for a full cycle of the fully developed three DoF simulations of wing rock was found clearly stable.
- Discarding the vertical fin in the prediction of the wing rock onset and characteristics was found to lead to different results. Unlike the effect of including the three DoF in wing rock simulations, which is approximately model-independent, the effect of vertical fin is greatly depending on its geometry and can't be generalized.

The author recommends performing the following utilizing the CFD-code developed for this effort:

- Computing the static lateral stability derivatives at the predicted onset to correlate with the pseudo derivative that was computed from the recorded data during the motion.
- Studying the effect of fore-body vortex control by tangential blowing for the case of three DoF wing rock oscillations.
- Obtain more accurate results for the onset point by repeating the simulations for 1^{o} increments in angle of attack rather than the 5^{o} increment used in the present study.
- Perform more fine mesh runs to validate the coarse mesh results.
- Extending the present work for flexible-body dynamics.

Bibliography

1. AGARD *"Computation Aerodynamics Based on Euler Equations,"* Technical Report, AGARD-AG-325 (1991).

2. Anderson, S. B. "Handling Qualities Related to Stall/Spin Accidents of Supersonic Fighter Aircraft," *J. Aircraft, 22 (10)*: 875-880 (Oct. 1985).

3. Beam, R. M. and Warming R. F. "An Implicit Factored Scheme for the Compressible Navier-Stokes Equations," *AIAA Journal, 16 (4)*: 393-402 (April 1978).

4. Brandon, J. M. and Nguyen L. T. "Experimental Study of Effects of Forebody Geometry on High Angle of Attack Static and Dynamic Stability," *AIAA Paper 86-0331* (January 1986).

5. Chaderjian, N. M. "Navier-Stokes Prediction of Large-Amplitude Delta-Wing Roll Oscillations," *J. Aircraft, 31 (6)*: 1333-1340 (Nov.-Dec. 1994).

6. Chaderjian, N. M. and Schiff B. Lewis. "Navier-Stokes Prediction of a Delta Wing in Roll with Vortex Breakdown," *AIAA Paper 93-3495* (1993).

7. Chaderjian, N. M. and Schiff L. B. "Numerical Simulation of Forced and Free-to-Roll Delta-Wing Motions," *J. Aircraft, 33 (1)*: 93-100 (Jan.-Feb. 1996).

8. Elzedbda, J. M., Nayfeh A. H., and Mook D. T. "Development of an Analytical Model of Wing Rock for Slender Delta Wings," *J. Aircraft, 26 (8)*: 737-743 (August 1989).

9. Ericson, L. E. "The Fluid Mechanics of Slender Wing Rock," *J. Aircraft, 21 (5)*: 322-328 (May 1984).

10. Ericson, L. E. "Slender Wing Rock Revisited," *AIAA Paper 91-0417* (January 1991).

11. Ericson, L. E. "The Various Sources of Wing Rock," *AIAA Paper 88-4370* (August 1988).

12. Ericson, L. E. "Wing Rock Analysis of Slender Delta Wings, Review and Extension," *J. Aircraft, 32 (6)*: 1221-1226 (Nov.-Dec. 1995).

13. Ericson, L. E. "Wing Rock Generated By Forebody Vortices," *AIAA Paper 87-0268* (January 1987).

14. Ericsson, L. E. and Reding J. P. "Stall Flutter Analysis," *J. Aircraft, 10 (1)*: 5-13 (January 1973).

15. Fratello, D. J., Croom M. A., Nguyen L. T., and Domack C. S. "Use of the Updated NASA Langley Radio-Controlled Drop Model Technique for High-Alpha Studies of the X-29A Configuration," *AIAA Paper 87-2559* (August 1987).

16. Gordnier, R. E. "Computation of Delta-Wing Roll Maneuvers," *J. Aircraft, 32 (3)*: 486-492 (May-June 1995).

17. Gordnier, R. E. "Computation of Vortex Breakdown on a Rolling Delta Wing," *J. Aircraft, 32 (3)*: 686-688 (May-June 1995).

18. Gordnier, R. E. "Numerical Simulation of a 65-Degree Delta-Wing Flowfield," *J. Aircraft, 33 (4)*: 492-499 (July-Aug. 1997).

19. Gordnier, R. E. and Visbal M. R. "Numerical Simulation of Delta-Wing Roll," *AIAA Paper 93-0554* (January 1993).

20. Gordnier, R. E. and Visbal M. R. "Numerical Simulation of Delta-Wing Roll," *Aerospace Science and Technology, (6)*: 347-357 (1998).

21. Hall, R. M. and Del Frate J. H. *"Interaction Between Forebody and Wing Vortices- A Water-Tunnel Study,"* Air Force Wright Aeronautical Lab., Wright-Patterson AFB, OH, January 1986 (AFWAL-TM-85-252).

22. Hsu, C. H. and Lan C. E. "Theory of Wing Rock," *J. Aircraft, 22 (10)*: 920-924 (October 1985).

23. Jackson, P. J. (Ed.) *Jane's All the World's Aircraft (1999-2000)*. New York: Franklin Watts (1999).

24. Jun, Y. W. and Nelson R. C. "Leading Edge Vortex Dynamics on a Delta Wing Undergoing a Wing Rock Motion," *AIAA Paper 87-0332* (1987).

25. Kandil, O. A. and Salman A. A. "Three-Dimensional Simulation of Slender Delta Wing Rock and Divergence," *AIAA Paper 92-0280* (1992).

26. Katz, J. "Numerical Simulation of Aircraft Rotary Aerodynamics," *J. Aircraft, 26 (7)*: 692-693 (July 1989).

27. Katz, J. "Wing/Vortex Interactions and Wing Rock," *Progress in Aerospace Sciences, 35 (7)*: 727-750 (October 1999).

28. Konstadinopoulos, P., Thrasher D. F., and Mook D. T. "A Vortex-Lattice Method for General, Unsteady Aerodynamics," *J. Aircraft, 22 (1)*: 43-50 (January 1985).

29. Konstadinopoulus, P., Mook D. T., and Nayfeh A. H. "Subsonic Wing Rock of Slender Delta Wings," *J. Aircraft, 22 (3)*: 223-228 (March 1985).

30. Lee, E. M. and Batina, J. T. "Conical Euler Simulations of Wing Rock for a Delta Wing Planform," *J. Aircraft, 28 (1)*: 94-96 (January 1991).

31. Levin, D. and Katz J. "Dynamic Load Measurements with Delta Wings Undergoing Self-Induced Roll-Oscillations," *J. Aircraft, 21 (1)*: 30-36 (January 1984).

32. Levin, D. and Katz J. "Vortex-lattice Method for the Calculation of the Nonsteady Separated Flow over Delta Wings," *J. Aircraft, 18 (12)*: 1032-1037 (December 1981).

33. Liebst, B. S. "The Dynamics, Prediction, and Control of Wing Rock in High Performance Aircraft," *the Royal Society Philosophical Transactions: Mathematical, Physical, and Engineering Sciences, London 356*: 2257-2276 (August 1998).

34. Liebst, B. S. and DeWitt B. R. "Wing Rock Suppression in the F-15 Aircraft," *AIAA Paper 97-3719* (August 1997).

35. Liebst, B. S. and Nolan R. C. "Method for the Prediction of the Onset of Wing Rock," *J. Aircraft, 31 (6)*: 1419-1421 (1994).

36. Lutton, M.J., and Visbal M.R. "Time-Accurate Validation of the Chimera Method for Unsteady Vortical Flows," *AIAA Paper 96-2077* (1996).

37. Mabey, D. G. "Similitude Relations for Buffet and Wing Rock on Delta Wings," *Progress in Aerospace Sciences, 33 (7/8)*: 481-511 (1997).

38. Morton, S. A., Rizzetta D.P., and Melville R. B. "Numerical Simulation of the Interaction between a Leading-Edge Vortex and a Flexible Vertical Tail," *AIAA Paper 98-1957* (1998).

39. Nayfeh, A. H., Elzedbda J. M., and Mook D. T. "Analytical Study of the Subsonic Wing-Rock Phenomenon for Slender Delta Wings," *J. Aircraft, 26 (9)*: 805-809 (September 1989).

40. Nelson, Robert C. *Flight Stability and Automatic Control.* Boston, Mass.: WCB/McGraw Hill, 1998.

41. Ng, T. T., Suarez C. J., Kramer D. T., Ong L. Y., Ayers B., and Malcom G. N. "Forebody Vortex Control for the Wing Rock Suppression," *J. Aircraft, 31 (2)*: 298-305 (March 1994).

42. Nguyen, L. T., Yip L. P., and Chambers J. R. "Self-induced Wing Rock of Slender Delta Wings," *AIAA Paper 81-1883* (August 1981).

43. Nolan, Robert C. *Wing Rock Prediction Method for a High Performance Fighter Aircraft.* MS thesis, AFIT/GAE/ENY/92J-02. School of Engineering, Air Force Institute of Technology (AU), Wright-Patterson AFB OH, June 1992 (AD-A256 438).

44. Pointwise Company, "*Gridgen User Manual Version 13, A Grid Generation Software,*" Pointwise Inc., Bedford-Texas (1998).

45. Pulliam T. H. and Stager J. L. "Implicit Finite-Difference Simulations of Three-Dimensional Compressible Flow," *AIAA Journal, 18 (2)*: 159-167 (February 1980).

46. Pulliam, T. H. and Chaussee D. S. "A Diagonal Form of an Implicit Approximate-Factorization Algorithm," *Journal of Computational Physics, 39 (2)*: 347-363 (1981).

47. Rizzetta, D.P. "Numerical Simulation of the Interaction between a Leading-Edge Vortex and a Vertical Tail," *AIAA Paper 96-2012* (1996).

48. Saad, Ahmed A. and Liebst Brad S. "An Analytical Criterion for the Prediction and Analysis of Wing Rock Onset," *AIAA Paper 99-4099* (Aug. 1999).

49. Steger, J.L., Benek J.A., and Dougherty F.C. " A Flexible Grid Embedding Technique with Application to the Euler Equations," *AIAA Paper 83-1944* (1983).

50. Straka, W. A., and Hemsh M. J. "Effect of Fuselage on Delta Wing Vortex Breakdown," *J. Aircraft, 30 (4)*: 1003-1005 (1994).

51. Suhs, N. E., and Tramel R. W. "*PEGSUS 4.0 User's Manual,*" Technical Report, AEDC-TR-91-8, (November 1991).

52. Tromp, J. C. "Flowfield Simulation about a 65-Degree Delta Wing During Constant Roll-Rate Motions," *J. Aircraft, 36 (2)*: 486-489 (1998).

53. Wang, Z.J. "A Fully Conservative Structured/Unstructured Chimera Grid Scheme," *AIAA Paper 95-0671* (1996).

54. Whitfield, David L. "Three-Dimensional Unsteady Euler Equation Solutions Using Flux Vector Splitting," *Printed Notes for a Short Course on Numerical Grid Generation, Mississippi State University, Mississippi State, MS,* (June 1984).

55. Yu, N. J., Kusunose K., and Chen, H. C. "Flow Simulation for a Complex Airplane Configuration Using Euler Equations," *AIAA Paper 87-0454* (1987).

Appendix A – *PEGSUS* Inputs

A.1 PEGSUS User Inputs File

```
C     PEGSUS 4.0 INPUT FILE (Coarse Mesh Version)
C     DEFINE GLOBAL PARAMETERS
      $GLOBAL
       FRINGE = 2,
      $END

C     DEFINE MESHES

      $MESH NAME = 'CWBGRID',
       LINK = 'CFINGRID',
      JINCLUDE = 31,68,
       KINCLUDE = 2,28,
       LINCLUDE = 19,47,
       QUALITY = 1.0,0.3,-0.1,
      $END

      $MESH NAME = 'CFINGRID',
       LINK = 'CWBGRID',
      JINCLUDE = 1,43,
       KINCLUDE = 1,36,
       LINCLUDE = 1,34,
       QUALITY = 1.0,0.3,-0.1,
      $END

      $MESH NAME = 'PHANTGRID'
      $END

C     DEFINE BOUNDARIES

      $BOUNDARY NAME = 'PHANT HOLE BOUND',
       ISPARTOF = 'PHANTGRID',
       MHOLEIN = 'CWBGRID',
      $END

      $BOUNDARY NAME = 'FIN OUTER BOUND',
       ISPARTOF = 'CFINGRID',
       CLOSED =.FALSE.,
      $END

C     DEFINE THE SURFACES THAT CONNECTED TO THE PHANT HOLE BOUND
C     THE BOUNDARY IN GENERAL IS A BOX-LIKE SHAPE COMPRISES OF 4
C     SURFACES TO AVOID CONCAVITIES AT THE BOX CORNERS

      $SURFACE ISPARTOF = 'PHANT HOLE BOUND',
      JRANGE = 1,40,
       KRANGE = 1,10,
```

```
 LRANGE = 30,30,
 NVOUT = '+L',
$END
$SURFACE ISPARTOF = 'PHANT HOLE BOUND',
 JRANGE = 1,40,
 KRANGE = 1,10,
 LRANGE = 1,1,
 NVOUT = '-L',
$END
$SURFACE ISPARTOF = 'PHANT HOLE BOUND',
 JRANGE = 1,1,
 KRANGE = 1,10,
 LRANGE = 1,30,
 NVOUT = '-J',
$END
$SURFACE ISPARTOF = 'PHANT HOLE BOUND',
 JRANGE = 40,40,
 KRANGE = 1,10,
 LRANGE = 1,30,
 NVOUT = '+J',
$END
$SURFACE ISPARTOF = 'PHANT HOLE BOUND',
 JRANGE = 1,40,
 KRANGE = 1,1,
 LRANGE = 1,30,
 NVOUT = '-K',
$END
$SURFACE ISPARTOF = 'PHANT HOLE BOUND',
 JRANGE = 1,40,
 KRANGE = 10,10,
 LRANGE = 1,30,
 NVOUT = '+K',
$END

C     DEFINE THE OUTER BOUNDARY OF THE FIN MESH

$SURFACE ISPARTOF = 'FIN OUTER BOUND',
 JRANGE = 1,43,
 KRANGE = 1,36,
 LRANGE = 33,34,
$END
$SURFACE ISPARTOF = 'FIN OUTER BOUND',
 JRANGE = 1,2,
 KRANGE = 1,36,
 LRANGE = 2,32,
$END
$SURFACE ISPARTOF = 'FIN OUTER BOUND',
 JRANGE = 42,43,
 KRANGE = 1,36,
 LRANGE = 2,32,
$END
```

```
      $SURFACE ISPARTOF = 'FIN OUTER BOUND',
       JRANGE = 3,41,
        KRANGE = 1,2,
        LRANGE = 2,32,
      $END
      $SURFACE ISPARTOF = 'FIN OUTER BOUND',
       JRANGE = 3,41,
        KRANGE = 35,36,
        LRANGE = 2,32,
      $END
C   Define the Fin surface and the fuselage part in the Fin mesh
C   as interior banked points to be excluded from the flow field
      $REGION NAME = 'FIN REGION',
       TYPE = 'INTR',
       ISPARTOF = 'CFINGRID',
      $END
C     DEFINE FIN SURFACE
      $VOLUME ISPARTOF = 'FIN REGION',
       JRANGE = 14,29,
        KRANGE = 18,19,
        LRANGE = 2,20,
      $END
```

A.2 PEGSUS Parameters

```
MDIM=3
LNDIM=3
ICHAR=40
NBDIM=3
MHDIM=2
NSDIM=14
MSLEN=25000
NXDIM=1
NRDIM=2
NVDIM=3
INCORE=0
MLEN=999999
MLEMAX=999999
MILEN=250000
NBYTEI=8
NBYTER=8
MSSMAX = MSLEN*(INCORE*NSDIM+1-INCORE),
MIMAX1 = MILEN*(INCORE*MDIM+1-INCORE),
MIMAX2 = MILEN*(INCORE*MDIM*MDIM+1-INCORE)
```

A.3 Input Mesh Format

The individual meshes are input to the *PEGSUS* via the input file INGRID, which has the following format for each individual mesh:

RECORD	VARIABLES
1	Mesh Name
2	JMAX, KMAX, LMAX
3	(((X(J,K,L),J=1,JMAX),K=1,KMAX),L=1,LMAX), (((Y(J,K,L),J=1,JMAX),K=1,KMAX),L=1,LMAX), (((Z(J,K,L),J=1,JMAX),K=1,KMAX),L=1,LMAX)

Where JMAX, KMAX, and LMAX are the maximum mesh indices in the J, K, and L directions respectively.

Appendix B – *PEGSUS* Output

B.1 PEGSUS Output Summary

```
          PPPPPPPPP  EEEEEEEEE  GGGGGGGGG  SSSSSSSSS  UUU   UUU  SSSSSSSSS
        PPPPPPPPP  EEEEEEEEE  GGGGGGGGG  SSSSSSSSS  UUU   UUU  SSSSSSSSS
       PPP   PPP  EEE        GGG        SSS        UUU   UUU  SSS
      PPP   PPP  EEE        GGG        SSS        UUU   UUU  SSS
     PPPPPPPPP  EEEEEEEEE  GGG        SSSSSSSSS  UUU   UUU  SSSSSSSSS
    PPPPPPPPP  EEEEEEEEE  GGG        SSSSSSSSS  UUU   UUU  SSSSSSSSS
   PPP        EEE        GGG  GGGG        SSS  UUU   UUU        SSS
  PPP        EEE        GGG    GG        SSS  UUU   UUU        SSS
 PPP        EEEEEEEEE  GGGGGGGGG  SSSSSSSSS  UUUUUUUUU  SSSSSSSSS
PPP        EEEEEEEEE  GGGGGGGGG  SSSSSSSSS  UUUUUUUUU  SSSSSSSSS

                              VERSION  4.x


      PARAMETERS

       MDIM=     3
       LNDIM=    3
       ICHAR=   40
       NBDIM=    3
       MHDIM=    2
       NSDIM=   14
       MSLEN=  25000
       NXDIM=    1
       NRDIM=    2
       NVDIM=    3
       INCORE= 0
       MLEN=   999999
       MLEMAX=   999999
       MILEN=   250000



                  GLOBAL DESCRIPTION READ
                 3 MESH DESCRIPTIONS READ
                 2 BOUNDARY DESCRIPTIONS READ
                11 SURFACE DESCRIPTIONS READ
                 0 BOX DESCRIPTIONS READ
                 1 REGION DESCRIPTIONS READ
                 1 VOLUME DESCRIPTIONS READ


    READING MESH: CWBGRID
    READING MESH: CFINGRID
    READING MESH: PHANTGRID
```

```
 ***** GLOBAL PARAMETER SUMMARY *****

MIN/MAX OF DOMAIN
MIN X =  -0.1200E+01     MAX X =   0.3000E+01
MIN Y =  -0.1500E+01     MAX Y =   0.1500E+01
MIN Z =  -0.1500E+01     MAX Z =   0.1500E+01

NO INCLUDE RANGES SPECIFIED

NO. OF FRINGE POINTS = 2
QUALITY(1)           =   1.0000
QUALITY(2)           =   1.0000
QUALITY(3)           =   1.0000
EPS                  =   0.1000E-02


GLOBAL ROTATION SEQUENCE =

1    ***** MESH PARAMETER SUMMARY *****


MESH NAME: CWBGRID

PEGSUS MESH NO.=    1
COMPOSITE MESH NO.=    1

INDEX RANGES:  JMAX =    79  KMAX =    35  LMAX =    65

TRANSLATION: X0    =   0.0000E+00  Y0   =   0.0000E+00  Z0  =   0.0000E+00
ROTATION:    XR    =   0.0000E+00  YR   =   0.0000E+00  ZR  =   0.0000E+00
             ALPHA =   0.0000E+00  BETA =   0.0000E+00  GAM =   0.0000E+00
SCALING:     SCALE =   0.1000E+01
ROTATION SEQUENCE =

NO. OF FRINGE POINTS = 2
QUALITY(1)           =   1.0000
QUALITY(2)           =   0.3000
QUALITY(3)           =  -0.1000
EPS                  =   0.1000E-02

MIN/MAX OF MESH
MIN X =  -0.1200E+01     MAX X =   0.3000E+01
MIN Y =  -0.1500E+01     MAX Y =   0.1500E+01
MIN Z =  -0.1500E+01     MAX Z =   0.1500E+01

INCLUDE PARAMETERS
MIN X =  -0.1000E+31     MAX X =   0.1000E+31
MIN Y =  -0.1000E+31     MAX Y =   0.1000E+31
MIN Z =  -0.1000E+31     MAX Z =   0.1000E+31
MIN J =    31            MAX J =    68
MIN K =     2            MAX K =    28
MIN L =    19            MAX L =    47
```

```
 LINKS
 NO.     NAME
  1      CFINGRID


MESH NAME: CFINGRID

PEGSUS MESH NO.=     2
COMPOSITE MESH NO.=     2

INDEX RANGES:  JMAX =     43  KMAX =     36  LMAX =     34

TRANSLATION: X0     =   0.0000E+00  Y0    =   0.0000E+00  Z0  =   0.0000E+00
ROTATION:    XR     =   0.0000E+00  YR    =   0.0000E+00  ZR  =   0.0000E+00
             ALPHA  =   0.0000E+00  BETA  =   0.0000E+00  GAM =   0.0000E+00
SCALING:     SCALE  =   0.1000E+01
ROTATION SEQUENCE =

NO. OF FRINGE POINTS = 2
QUALITY(1)           =   1.0000
QUALITY(2)           =   0.3000
QUALITY(3)           =  -0.1000
EPS                  =   0.1000E-02

MIN/MAX OF MESH
MIN X =   0.9400E+00     MAX X =   0.1720E+01
MIN Y =  -0.4000E+00     MAX Y =   0.4000E+00
MIN Z =   0.0000E+00     MAX Z =   0.4599E+00

INCLUDE PARAMETERS
MIN X =  -0.1000E+31     MAX X =   0.1000E+31
MIN Y =  -0.1000E+31     MAX Y =   0.1000E+31
MIN Z =  -0.1000E+31     MAX Z =   0.1000E+31
MIN J =     1            MAX J =    43
MIN K =     1            MAX K =    36
MIN L =     1            MAX L =    34


LINKS
 NO.     NAME
  1      CWBGRID


MESH NAME: PHANTGRID

PEGSUS MESH NO.=     3
PHANTOM MESH

INDEX RANGES:  JMAX =     40  KMAX =     10  LMAX =     30

TRANSLATION: X0     =   0.0000E+00  Y0    =   0.0000E+00  Z0  =   0.0000E+00
ROTATION:    XR     =   0.0000E+00  YR    =   0.0000E+00  ZR  =   0.0000E+00
             ALPHA  =   0.0000E+00  BETA  =   0.0000E+00  GAM =   0.0000E+00
SCALING:     SCALE  =   0.1000E+01
```

```
ROTATION SEQUENCE =

NO. OF FRINGE POINTS = 2
QUALITY(1)           =   1.0000
QUALITY(2)           =   1.0000
QUALITY(3)           =   1.0000
EPS                  =   0.1000E-02

MIN/MAX OF MESH
MIN X =   0.1100E+01     MAX X =   0.1526E+01
MIN Y =  -0.1000E+00     MAX Y =   0.1000E+00
MIN Z =   0.0000E+00     MAX Z =   0.3400E+00

NO INCLUDE RANGES SPECIFIED


LINKS
 NO.    NAME
1

***** BOUNDARY PARAMETER SUMMARY *****


BOUNDARY NAME: PHANT HOLE BOUND

BOUNDARY TYPE   = HOLE
CLOSED          =     T
IS PART OF MESH = PHANTGRID

MIN/MAX OF HOLE BOUNDARY
MIN X =   0.1100E+01     MAX X =   0.1526E+01
MIN Y =  -0.1000E+00     MAX Y =   0.1000E+00
MIN Z =   0.0000E+00     MAX Z =   0.3400E+00

MAKE HOLE IN:
 NO.    NAME
  1     CWBGRID

BOUNDARY NAME: FIN OUTER BOUND

BOUNDARY TYPE   = OUTER
CLOSED          =     F
IS PART OF MESH = CFINGRID

SURFACE NO. =     1
ISPARTOF : PHANT HOLE BOUND
SURFACE RANGES
MIN J =     1   MAX J =    40
MIN K =     1   MAX K =    10
MIN L =    30   MAX L =    30
NVOUT = +L
CONNECTING MESH = PHANTGRID

SURFACE NO. =     2
ISPARTOF : PHANT HOLE BOUND
SURFACE RANGES
MIN J =     1   MAX J =    40
```

```
MIN K =      1    MAX K =     10
MIN L =      1    MAX L =      1
NVOUT = -L
CONNECTING MESH = PHANTGRID

SURFACE NO. =      3
ISPARTOF : PHANT HOLE BOUND
SURFACE RANGES
MIN J =      1    MAX J =      1
MIN K =      1    MAX K =     10
MIN L =      1    MAX L =     30
NVOUT = -J
CONNECTING MESH = PHANTGRID

SURFACE NO. =      4
ISPARTOF : PHANT HOLE BOUND
SURFACE RANGES
MIN J =     40    MAX J =     40
MIN K =      1    MAX K =     10
MIN L =      1    MAX L =     30
NVOUT = +J
CONNECTING MESH = PHANTGRID

SURFACE NO. =      5
ISPARTOF : PHANT HOLE BOUND
SURFACE RANGES
MIN J =      1    MAX J =     40
MIN K =      1    MAX K =      1
MIN L =      1    MAX L =     30
NVOUT = -K
CONNECTING MESH = PHANTGRID

SURFACE NO. =      6
ISPARTOF : PHANT HOLE BOUND
SURFACE RANGES
MIN J =      1    MAX J =     40
MIN K =     10    MAX K =     10
MIN L =      1    MAX L =     30
NVOUT = +K
CONNECTING MESH = PHANTGRID

SURFACE NO. =      7
ISPARTOF : FIN OUTER BOUND
SURFACE RANGES
MIN J =      1    MAX J =     43
MIN K =      1    MAX K =     36
MIN L =     33    MAX L =     34
NVOUT =
CONNECTING MESH = CFINGRID

SURFACE NO. =      8
ISPARTOF : FIN OUTER BOUND
SURFACE RANGES
MIN J =      1    MAX J =      2
MIN K =      1    MAX K =     36
MIN L =      2    MAX L =     32
NVOUT =
```

```
CONNECTING MESH = CFINGRID

SURFACE NO. =     9
ISPARTOF : FIN OUTER BOUND
SURFACE RANGES
MIN J =    42   MAX J =    43
MIN K =     1   MAX K =    36
MIN L =     2   MAX L =    32
NVOUT =
CONNECTING MESH = CFINGRID

SURFACE NO. =    10
ISPARTOF : FIN OUTER BOUND
SURFACE RANGES
MIN J =     3   MAX J =    41
MIN K =     1   MAX K =     2
MIN L =     2   MAX L =    32
NVOUT =
CONNECTING MESH = CFINGRID

SURFACE NO. =    11
ISPARTOF : FIN OUTER BOUND
SURFACE RANGES
MIN J =     3   MAX J =    41
MIN K =    35   MAX K =    36
MIN L =     2   MAX L =    32
NVOUT =
CONNECTING MESH = CFINGRID
1

***** REGION PARAMETER SUMMARY *****

REGION NAME: FIN REGION

REGION TYPE = INTR
IS PART OF MESH = CFINGRID

VOLUME NO. =     1
ISPARTOF : FIN REGION

VOLUME RANGES
MIN J =    14   MAX J =    29
MIN K =    18   MAX K =    19
MIN L =     2   MAX L =    20

INTERPOLATING BOUNDARY POINTS FOR
MESH: CWBGRID
LINK: CFINGRID
QUALITY= 1.00000     STENCILS FOUND:     1712

NO ORPHAN POINTS LEFT IN MESH - CWBGRID

INTERPOLATING BOUNDARY POINTS FOR
MESH: CFINGRID
LINK: CWBGRID
QUALITY= 1.00000     STENCILS FOUND:    12210
LINK: CWBGRID
```

```
 QUALITY= 0.90000     STENCILS FOUND:       76
 LINK: CWBGRID
 QUALITY= 0.80000     STENCILS FOUND:       76
 LINK: CWBGRID
 QUALITY= 0.70000     STENCILS FOUND:       20
 LINK: CWBGRID
 QUALITY= 0.60000     STENCILS FOUND:       12
 LINK: CWBGRID
 QUALITY= 0.50000     STENCILS FOUND:        2

 NO ORPHAN POINTS LEFT IN MESH - CFINGRID

 INTERPOLATING BOUNDARY POINTS FOR
 MESH: PHANTGRID

1     ***** QUALITY SUMMARY *****

 MINIMUM        NO. OF INTERPOLATED
 QUALITY        BOUNDARY POINTS FOUND
   =1.0                 13922
  >=0.9                    76
  >=0.8                    76
  >=0.7                    20
  >=0.6                    12
  >=0.5                     2
  >=0.4                     0
  >=0.3                     0
  >=0.2                     0
  >=0.1                     0
  >=0.0                     0

 MESH: CWBGRID
 NUMBER OF BOUNDARY POINTS:     1712
 NUMBER OF INTERPOLATION STENCILS:    12396

 MESH: CFINGRID
 NUMBER OF BOUNDARY POINTS:    12396
 NUMBER OF INTERPOLATION STENCILS:     1712

XMER3D PARAMETERS

 MINIMUM DIMENSIONS REQUIRED FOR THE FLOW SOLVER

  IWRK   =  385128     IGRD   =  179725
  JDIM   =      79     KDIM   =      36     LDIM   =      65
  IIDIM  =   12396     IBDIM  =   12396     IQBDIM =   14108

XLIM3D PARAMETERS

 MINIMUM DIMENSIONS REQUIRED FOR THE FLOW SOLVER

  IWRK   =   61992     IGRD   =  179725
  LARG   =      79     NORPH  =       0
  IIDIM  =   12396     IBDIM  =   12396     ISDIM  =  898625
```

B.2 Diagnostic Maps

```
                    DIAGNOSTIC MAPS
          LEGEND

BOUNDARY POINTS UPDATED BY :
 A  -  CWBGRID
 B  -  CFINGRID

 INTERPOLATION STENCILS UPDATING POINTS IN :
 a  -  CWBGRID
 b  -  CFINGRID

 .  -  FIELD POINT
 #  -  HOLE POINT
 ?  -  ORPHANED BOUNDARY POINT
 *  -  INTERPOLATION STENCIL UPDATING MORE THAN ONE
       INTERPOLATION BOUNDARY POINT
```

Here in the following are samples of the diagnostic maps for the two meshes:

```
MAP FOR CWBGRID

         PLANE  L =  31


    J        1         2         3         4         5         6         7         8
      12345678901234567890123456789012345678901234567890123456789012345678901234567890
  K
   1 .....................................*.......##################.....................
   2 ....................................*b....BB##################BB..**.............
   3 ....................................**....BB##################BB..**.............
   4 ....................................**....BB##################BB..**.............
   5 ....................................*....BB##################BB..**.............
   6 ....................................*.....BB##################BB..**.............
   7 ....................................**....BB##################BB..**.............
   8 ...................................b*....BB##################BB..**.............
   9 ....................................**...BB##################BB..**.............
  10 ....................................**....BB##################BB..**.............
  11 ....................................*b...BB##################BB..**.............
  12 ....................................**....BB##################BB..**.............
  13 ....................................**...BB##################BB..**.............
  14 ....................................**....BB##################BB..**.............
  15 ....................................**...BB##############BB..**.............
  16 ....................................**...BB##############BB..**.............
  17 ....................................**...BB##############BB..**.............
  18 ....................................**...BB##########BB..**.............
  19 ....................................**...BB##########BB..**.............
  20 ....................................**...BBBBBBB###BB..**.............
  21 ....................................*********bBBBBB...**.............
  22 ....................................***********B....**.............
  23 ....................................*********.............
  24 ....................................
  25 ....................................
  26 ....................................
  27 ....................................
  28 ....................................
  29 ....................................
  30 ....................................
  31 ....................................
  32 ....................................
  33 ....................................
  34 ....................................
  35 ....................................
```

MAP FOR CWBGRID

PLANE L = 32

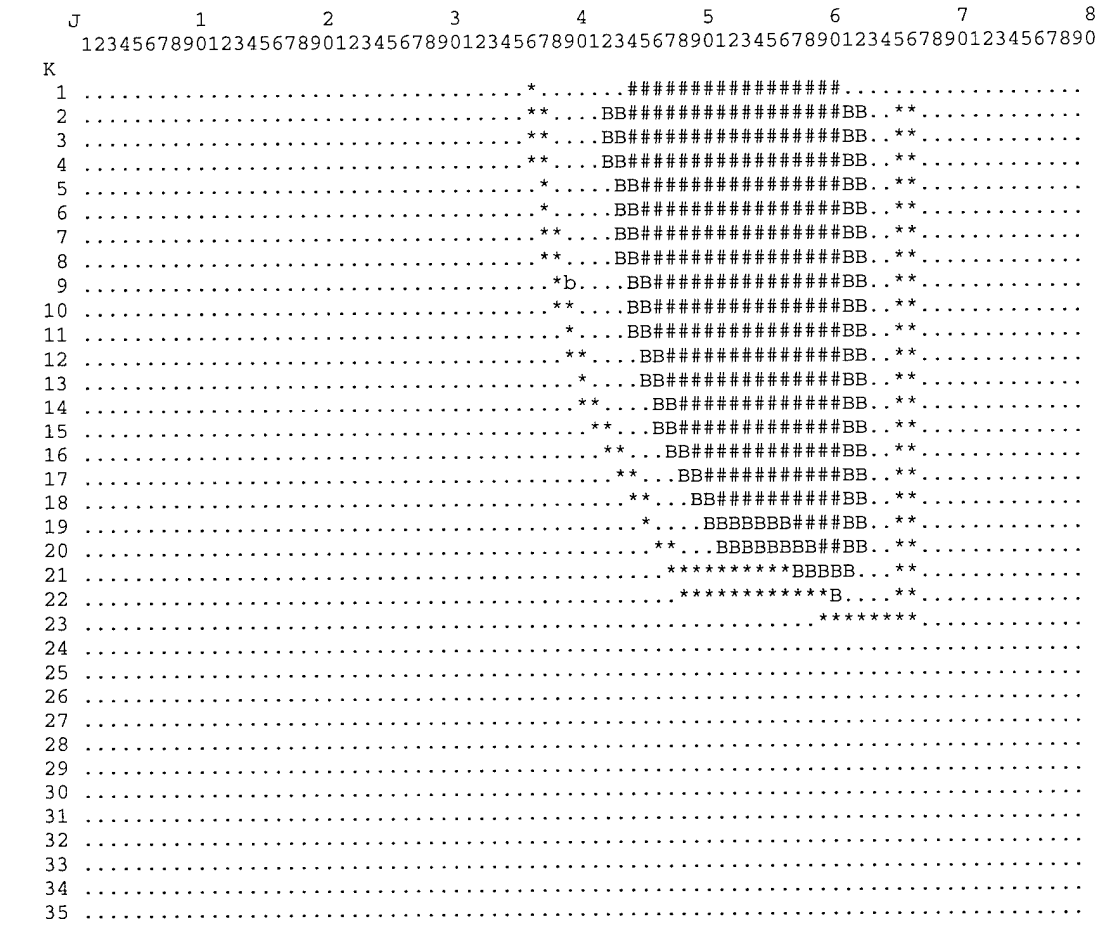

MAP FOR CWBGRID

PLANE L = 33

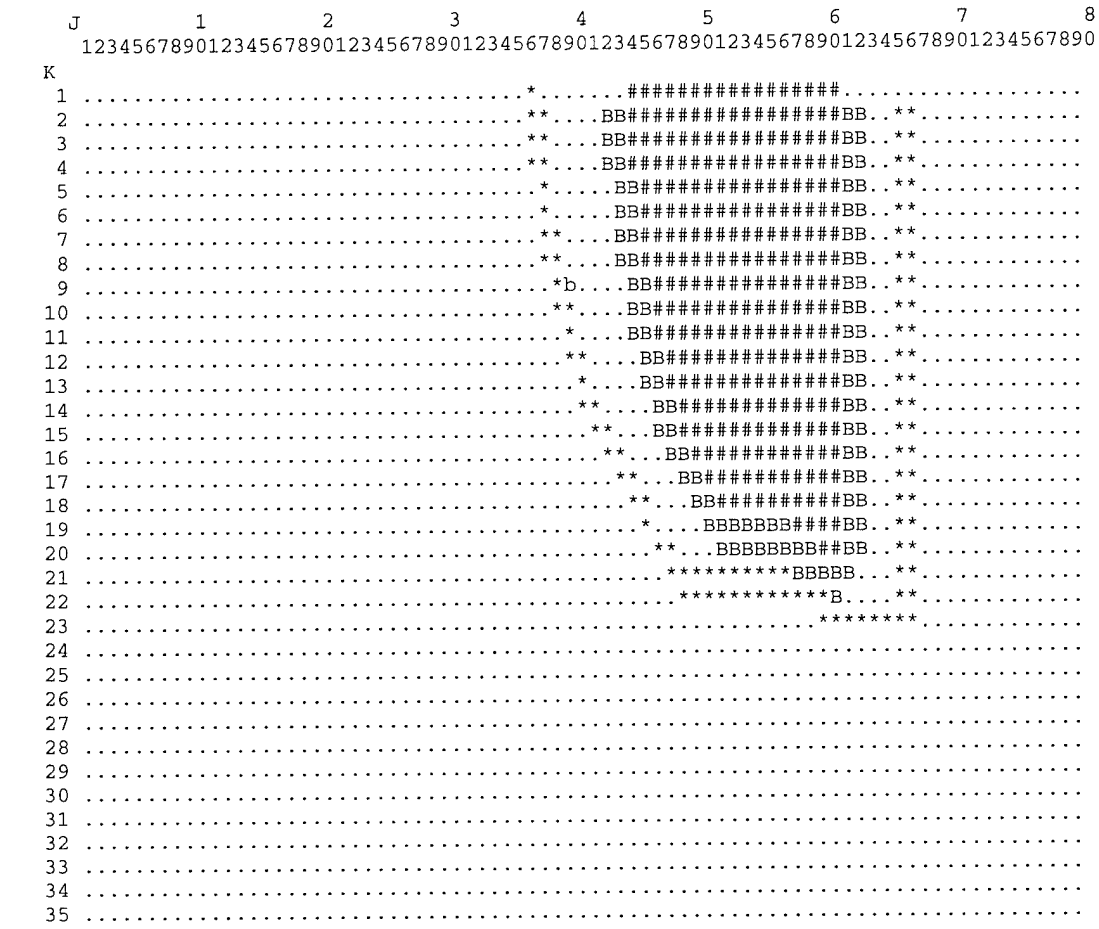

MAP FOR CWBGRID

PLANE L = 34

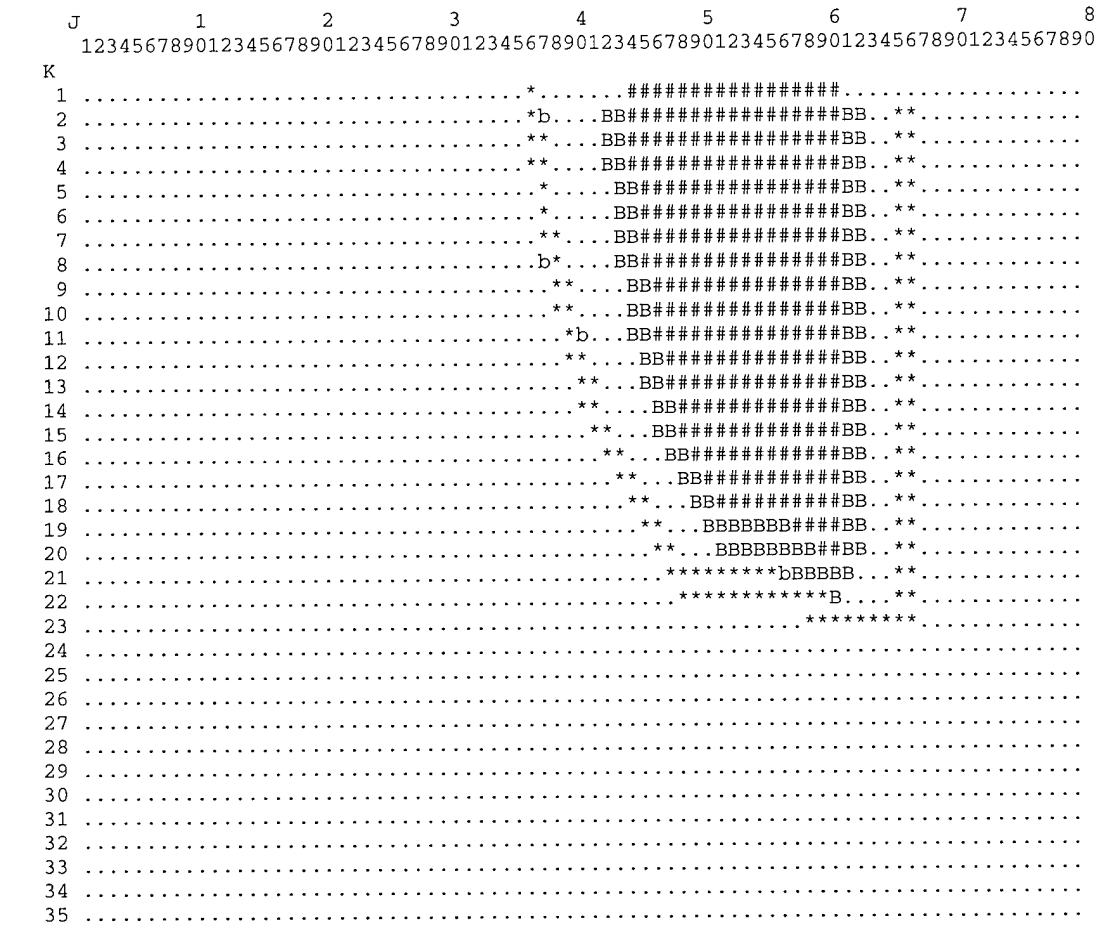

MAP FOR CWBGRID

PLANE L = 35

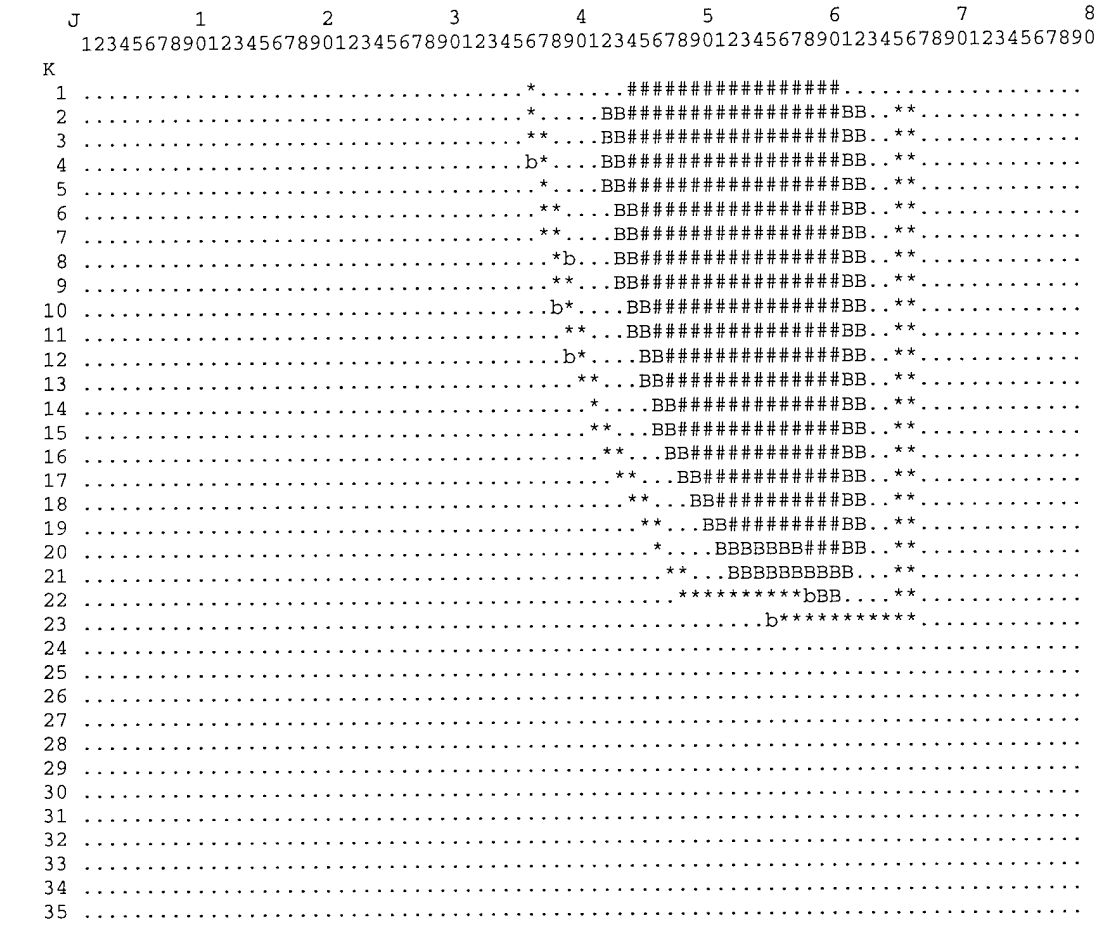

MAP FOR CFINGRID

PLANE L = 2

```
  J         1         2         3         4         5
    12345678901234567890123456789012345678901234567890
K
 1 AAAAAAAAAAAAAAAAAAAAAAAAAAAAAAAAAAAAAAAAAAAAAAAAAA
 2 AAAAAAAAAAAAAAAAAAAAAAAAAAAAAAAAAAAAAAAAAAAAAAAAAA
 3 AA....................................................AA
 4 AA....................................................AA
 5 AA.......a.....................a.......AA
 6 AA...............aaaaaaaa.a.aaa.a.....AA
 7 AA.....a.aa..a.a.....................AA
 8 AA...................aaa.....a*.aa.a.....AA
 9 AA....................................AA
10 AA....aa..............................AA
11 AA..............................aa....AA
12 AA....aa..............................AA
13 AA....................................AA
14 AA.....a.a.....................aa....AA
15 AA....................................AA
16 AA.....a.a.....................aa....AA
17 AA....................................AA
18 AA.....a.a...#################......aa....AA
19 AA...........#################.....AA
20 AA.....a.a.....................aa....AA
21 AA....................................AA
22 AA.....a.a.....................aa....AA
23 AA....................................AA
24 AA....aa..............................AA
25 AA..............................aa....AA
26 AA....aa..............................AA
27 AA....................................AA
28 AA...................aaa.....a*.aa.a.....AA
29 AA.....a.aa..a.a.....................AA
30 AA...............aaaaaaaa.a.aaa.a.....AA
31 AA.......a.....................a.......AA
32 AA....................................AA
33 AA....................................AA
34 AA....................................AA
35 AAAAAAAAAAAAAAAAAAAAAAAAAAAAAAAAAAAAAAAAAAAAAAAAAA
36 AAAAAAAAAAAAAAAAAAAAAAAAAAAAAAAAAAAAAAAAAAAAAAAAAA
```

MAP FOR CFINGRID

PLANE L = 3

```
  J        1         2         3         4         5
    12345678901234567890123456789012345678901234567890
K
 1 AAAAAAAAAAAAAAAAAAAAAAAAAAAAAAAAAAAAAAAAAAAAAAAAAA
 2 AAAAAAAAAAAAAAAAAAAAAAAAAAAAAAAAAAAAAAAAAAAAAAAAAA
 3 AA....................................................AA
 4 AA....................................................AA
 5 AA.............................a*.....................AA
 6 AA..............aaaaaa......aa.........AA
 7 AA.....a.aa..a.a.....................AA
 8 AA................aaaaaa.a.aaa.aa.a.....AA
 9 AA.....a..a..a.a.aa..................AA
10 AA....a.....................AA
11 AA.............................aa....AA
12 AA....aa.....................AA
13 AA....................................AA
14 AA.....aa.....................aa....AA
15 AA....................................AA
16 AA.....aa.....................aa....AA
17 AA....................................AA
18 AA.....aa....################......aa....AA
19 AA...........################............AA
20 AA.....aa.....................aa....AA
21 AA....................................AA
22 AA.....aa.....................aa....AA
23 AA....................................AA
24 AA....aa.....................AA
25 AA.............................aa....AA
26 AA....a.....................AA
27 AA.....a..a..a.a.aa..................AA
28 AA................aaaaaa.a.aaa.aa.a.....AA
29 AA.....a.aa..a.a.....................AA
30 AA..............aaaaaa......aa.........AA
31 AA.............................a*.....AA
32 AA....................................AA
33 AA....................................AA
34 AA....................................AA
35 AAAAAAAAAAAAAAAAAAAAAAAAAAAAAAAAAAAAAAAAAAAAAAAAAA
36 AAAAAAAAAAAAAAAAAAAAAAAAAAAAAAAAAAAAAAAAAAAAAAAAAA
```

MAP FOR CFINGRID

PLANE L = 4

```
  J        1         2         3         4         5
   12345678901234567890123456789012345678901234567890
K
 1 AAAAAAAAAAAAAAAAAAAAAAAAAAAAAAAAAAAAAAAAAAAAAAAAAA
 2 AAAAAAAAAAAAAAAAAAAAAAAAAAAAAAAAAAAAAAAAAAAAAAAAAA
 3 AA..................................................AA
 4 AA..................................................AA
 5 AA.........................a.aa.......AA
 6 AA.............a.aaaaaaaa.a.aa...........AA
 7 AA......a.a..a.................a.......AA
 8 AA.............a.aaaaaaa.a..aa.aa.a.....AA
 9 AA.....aa.a.a..a.........................AA
10 AA..................................................AA
11 AA.....aa.........................aa....AA
12 AA..................................................AA
13 AA................................a.....AA
14 AA.....aa.........................a....AA
15 AA..................................................AA
16 AA.....aa.........................aa....AA
17 AA..................................................AA
18 AA.....aa....##################......aa....AA
19 AA..........##################.............AA
20 AA.....aa.........................aa....AA
21 AA..................................................AA
22 AA.....aa.........................a....AA
23 AA................................a.....AA
24 AA..................................................AA
25 AA.....aa.........................aa....AA
26 AA..................................................AA
27 AA.....aa.a.a..a.........................AA
28 AA.............a.aaaaaaa.a..aa.aa.a.....AA
29 AA......a.a..a.................a.......AA
30 AA............a.aaaaaaaa.a.aa...........AA
31 AA.........................a.aa.......AA
32 AA..................................................AA
33 AA..................................................AA
34 AA..................................................AA
35 AAAAAAAAAAAAAAAAAAAAAAAAAAAAAAAAAAAAAAAAAAAAAAAAAA
36 AAAAAAAAAAAAAAAAAAAAAAAAAAAAAAAAAAAAAAAAAAAAAAAAAA
```

MAP FOR CFINGRID

PLANE L = 33

```
  J         1         2         3         4         5
    12345678901234567890123456789012345678901234567890
K
 1 AAAAAAAAAAAAAAAAAAAAAAAAAAAAAAAAAAAAAAAAAAAAAAAAAA
 2 AAAAAAAAAAAAAAAAAAAAAAAAAAAAAAAAAAAAAAAAAAAAAAAAAA
 3 AAAAAAAAAAAAAAAAAAAAAAAAAAAAAAAAAAAAAAAAAAAAAAAAAA
 4 AAAAAAAAAAAAAAAAAAAAAAAAAAAAAAAAAAAAAAAAAAAAAAAAAA
 5 AAAAAAAAAAAAAAAAAAAAAAAAAAAAAAAAAAAAAAAAAAAAAAAAAA
 6 AAAAAAAAAAAAAAAAAAAAAAAAAAAAAAAAAAAAAAAAAAAAAAAAAA
 7 AAAAAAAAAAAAAAAAAAAAAAAAAAAAAAAAAAAAAAAAAAAAAAAAAA
 8 AAAAAAAAAAAAAAAAAAAAAAAAAAAAAAAAAAAAAAAAAAAAAAAAAA
 9 AAAAAAAAAAAAAAAAAAAAAAAAAAAAAAAAAAAAAAAAAAAAAAAAAA
10 AAAAAAAAAAAAAAAAAAAAAAAAAAAAAAAAAAAAAAAAAAAAAAAAAA
11 AAAAAAAAAAAAAAAAAAAAAAAAAAAAAAAAAAAAAAAAAAAAAAAAAA
12 AAAAAAAAAAAAAAAAAAAAAAAAAAAAAAAAAAAAAAAAAAAAAAAAAA
13 AAAAAAAAAAAAAAAAAAAAAAAAAAAAAAAAAAAAAAAAAAAAAAAAAA
14 AAAAAAAAAAAAAAAAAAAAAAAAAAAAAAAAAAAAAAAAAAAAAAAAAA
15 AAAAAAAAAAAAAAAAAAAAAAAAAAAAAAAAAAAAAAAAAAAAAAAAAA
16 AAAAAAAAAAAAAAAAAAAAAAAAAAAAAAAAAAAAAAAAAAAAAAAAAA
17 AAAAAAAAAAAAAAAAAAAAAAAAAAAAAAAAAAAAAAAAAAAAAAAAAA
18 AAAAAAAAAAAAAAAAAAAAAAAAAAAAAAAAAAAAAAAAAAAAAAAAAA
19 AAAAAAAAAAAAAAAAAAAAAAAAAAAAAAAAAAAAAAAAAAAAAAAAAA
20 AAAAAAAAAAAAAAAAAAAAAAAAAAAAAAAAAAAAAAAAAAAAAAAAAA
21 AAAAAAAAAAAAAAAAAAAAAAAAAAAAAAAAAAAAAAAAAAAAAAAAAA
22 AAAAAAAAAAAAAAAAAAAAAAAAAAAAAAAAAAAAAAAAAAAAAAAAAA
23 AAAAAAAAAAAAAAAAAAAAAAAAAAAAAAAAAAAAAAAAAAAAAAAAAA
24 AAAAAAAAAAAAAAAAAAAAAAAAAAAAAAAAAAAAAAAAAAAAAAAAAA
25 AAAAAAAAAAAAAAAAAAAAAAAAAAAAAAAAAAAAAAAAAAAAAAAAAA
26 AAAAAAAAAAAAAAAAAAAAAAAAAAAAAAAAAAAAAAAAAAAAAAAAAA
27 AAAAAAAAAAAAAAAAAAAAAAAAAAAAAAAAAAAAAAAAAAAAAAAAAA
28 AAAAAAAAAAAAAAAAAAAAAAAAAAAAAAAAAAAAAAAAAAAAAAAAAA
29 AAAAAAAAAAAAAAAAAAAAAAAAAAAAAAAAAAAAAAAAAAAAAAAAAA
30 AAAAAAAAAAAAAAAAAAAAAAAAAAAAAAAAAAAAAAAAAAAAAAAAAA
31 AAAAAAAAAAAAAAAAAAAAAAAAAAAAAAAAAAAAAAAAAAAAAAAAAA
32 AAAAAAAAAAAAAAAAAAAAAAAAAAAAAAAAAAAAAAAAAAAAAAAAAA
33 AAAAAAAAAAAAAAAAAAAAAAAAAAAAAAAAAAAAAAAAAAAAAAAAAA
34 AAAAAAAAAAAAAAAAAAAAAAAAAAAAAAAAAAAAAAAAAAAAAAAAAA
35 AAAAAAAAAAAAAAAAAAAAAAAAAAAAAAAAAAAAAAAAAAAAAAAAAA
36 AAAAAAAAAAAAAAAAAAAAAAAAAAAAAAAAAAAAAAAAAAAAAAAAAA
```

MAP FOR CFINGRID

PLANE L = 34

```
  J         1         2         3         4         5
    12345678901234567890123456789012345678901234567890
K
 1 AAAAAAAAAAAAAAAAAAAAAAAAAAAAAAAAAAAAAAAAAAAAAAAAAA
 2 AAAAAAAAAAAAAAAAAAAAAAAAAAAAAAAAAAAAAAAAAAAAAAAAAA
 3 AAAAAAAAAAAAAAAAAAAAAAAAAAAAAAAAAAAAAAAAAAAAAAAAAA
 4 AAAAAAAAAAAAAAAAAAAAAAAAAAAAAAAAAAAAAAAAAAAAAAAAAA
 5 AAAAAAAAAAAAAAAAAAAAAAAAAAAAAAAAAAAAAAAAAAAAAAAAAA
 6 AAAAAAAAAAAAAAAAAAAAAAAAAAAAAAAAAAAAAAAAAAAAAAAAAA
 7 AAAAAAAAAAAAAAAAAAAAAAAAAAAAAAAAAAAAAAAAAAAAAAAAAA
 8 AAAAAAAAAAAAAAAAAAAAAAAAAAAAAAAAAAAAAAAAAAAAAAAAAA
 9 AAAAAAAAAAAAAAAAAAAAAAAAAAAAAAAAAAAAAAAAAAAAAAAAAA
10 AAAAAAAAAAAAAAAAAAAAAAAAAAAAAAAAAAAAAAAAAAAAAAAAAA
11 AAAAAAAAAAAAAAAAAAAAAAAAAAAAAAAAAAAAAAAAAAAAAAAAAA
12 AAAAAAAAAAAAAAAAAAAAAAAAAAAAAAAAAAAAAAAAAAAAAAAAAA
13 AAAAAAAAAAAAAAAAAAAAAAAAAAAAAAAAAAAAAAAAAAAAAAAAAA
14 AAAAAAAAAAAAAAAAAAAAAAAAAAAAAAAAAAAAAAAAAAAAAAAAAA
15 AAAAAAAAAAAAAAAAAAAAAAAAAAAAAAAAAAAAAAAAAAAAAAAAAA
16 AAAAAAAAAAAAAAAAAAAAAAAAAAAAAAAAAAAAAAAAAAAAAAAAAA
17 AAAAAAAAAAAAAAAAAAAAAAAAAAAAAAAAAAAAAAAAAAAAAAAAAA
18 AAAAAAAAAAAAAAAAAAAAAAAAAAAAAAAAAAAAAAAAAAAAAAAAAA
19 AAAAAAAAAAAAAAAAAAAAAAAAAAAAAAAAAAAAAAAAAAAAAAAAAA
20 AAAAAAAAAAAAAAAAAAAAAAAAAAAAAAAAAAAAAAAAAAAAAAAAAA
21 AAAAAAAAAAAAAAAAAAAAAAAAAAAAAAAAAAAAAAAAAAAAAAAAAA
22 AAAAAAAAAAAAAAAAAAAAAAAAAAAAAAAAAAAAAAAAAAAAAAAAAA
23 AAAAAAAAAAAAAAAAAAAAAAAAAAAAAAAAAAAAAAAAAAAAAAAAAA
24 AAAAAAAAAAAAAAAAAAAAAAAAAAAAAAAAAAAAAAAAAAAAAAAAAA
25 AAAAAAAAAAAAAAAAAAAAAAAAAAAAAAAAAAAAAAAAAAAAAAAAAA
26 AAAAAAAAAAAAAAAAAAAAAAAAAAAAAAAAAAAAAAAAAAAAAAAAAA
27 AAAAAAAAAAAAAAAAAAAAAAAAAAAAAAAAAAAAAAAAAAAAAAAAAA
28 AAAAAAAAAAAAAAAAAAAAAAAAAAAAAAAAAAAAAAAAAAAAAAAAAA
29 AAAAAAAAAAAAAAAAAAAAAAAAAAAAAAAAAAAAAAAAAAAAAAAAAA
30 AAAAAAAAAAAAAAAAAAAAAAAAAAAAAAAAAAAAAAAAAAAAAAAAAA
31 AAAAAAAAAAAAAAAAAAAAAAAAAAAAAAAAAAAAAAAAAAAAAAAAAA
32 AAAAAAAAAAAAAAAAAAAAAAAAAAAAAAAAAAAAAAAAAAAAAAAAAA
33 AAAAAAAAAAAAAAAAAAAAAAAAAAAAAAAAAAAAAAAAAAAAAAAAAA
34 AAAAAAAAAAAAAAAAAAAAAAAAAAAAAAAAAAAAAAAAAAAAAAAAAA
35 AAAAAAAAAAAAAAAAAAAAAAAAAAAAAAAAAAAAAAAAAAAAAAAAAA
36 AAAAAAAAAAAAAAAAAAAAAAAAAAAAAAAAAAAAAAAAAAAAAAAAAA
```

Appendix C - Numerical Application of the Euler Boundary Conditions

The classical Euler boundary conditions have been known for decades as "there is no penetration of the fluid medium to the solid boundary", or alternatively the normal component of the relative fluid velocity is zero on a solid boundary. Although the statement of the Euler boundary condition seems simple, its application in computational fluid dynamics is not. In the rest of this Appendix, the numerical application of the Euler boundary conditions is presented in detail. The methodology will be discussed for a general case when the grids are allowed to move, and the static case can be easily derived by assigning zero value for the grid velocity.

The following assumptions have been made in the next derivation:

- First-order approximation for the tangents at the grid points on the body surface.
- The magnitude of the velocity at a grid point on the body surface is interpolated from the next point to the surface in the direction of the outward normal.

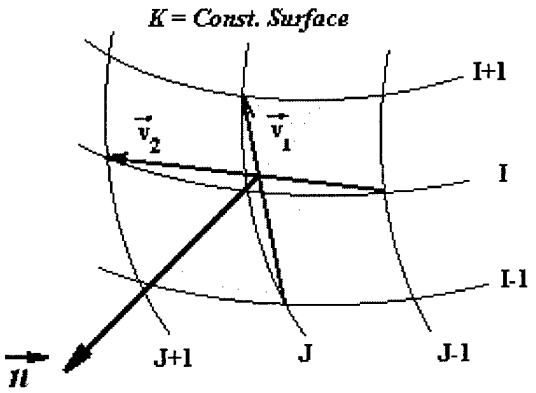

Figure C-1. Schematic drawing for the body surface.

Let $\vec{v}_1$ and $\vec{v}_2$ denote the two vectors that representing the first-order approximation of the tangents to the surface at the grid point (see figure C-1).

$$\vec{v}_1 = \big(x(i+1,j,k) - x(i-1,j,k)\big)\hat{i} + \big(y(i+1,j,k) - y(i-1,j,k)\big)\hat{j} + \big(z(i+1,j,k) - z(i-1,j,k)\big)\hat{k}$$

$$= v_{1_x}\hat{i} + v_{1_y}\hat{j} + v_{1_z}\hat{k}$$

$$\vec{v}_2 = \big(x(i,j+1,k) - x(i,j-1,k)\big)\hat{i} + \big(y(i,j+1,k) - y(i,j-1,k)\big)\hat{j} + \big(z(i,j+1,k) - z(i,j-1,k)\big)\hat{k}$$

$$= v_{2_x}\hat{i} + v_{2_y}\hat{j} + v_{2_z}\hat{k}$$

The outward normal to the surface $\vec{N}$ is determined as follows:

$$\vec{N} = \vec{v}_1 \times \vec{v}_2$$

$$= \big(v_{1_y}v_{2_z} - v_{1_z}v_{2_y}\big)\hat{i} + \big(v_{1_z}v_{2_x} - v_{1_x}v_{2_z}\big)\hat{j} + \big(v_{1_x}v_{2_y} - v_{1_y}v_{2_x}\big)\hat{k}$$

$$= N_x\hat{i} + N_y\hat{j} + N_z\hat{k}$$

Since $\vec{v}_1$ and $\vec{v}_2$ are not orthogonal in general, let $\vec{t}_1$ and $\vec{n}$ denote the unit vectors in the direction of $\vec{v}_1$ and $\vec{N}$ respectively, then use $\vec{t}_1$ and $\vec{n}$ to find the third orthogonal unit vector $\vec{t}_2$.

$$\vec{t}_2 = \vec{n} \times \vec{t}_1$$

Where:

$$\vec{t}_1 = \frac{\vec{v}_1}{|\vec{v}_1|}$$

$$= t_{1_x}\hat{i} + t_{1_y}\hat{j} + t_{1_z}\hat{k}$$

$$\vec{n} = \frac{\vec{N}}{|\vec{N}|}$$

$$= n_x\hat{i} + n_y\hat{j} + n_z\hat{k}$$

$$\Rightarrow \quad \vec{t}_2 = (n_y t_{1_z} - n_z t_{1_y})\,\hat{i} + (n_z t_{1_x} - n_x t_{1_z})\,\hat{j} + (n_x t_{1_y} - n_y t_{1_x})\hat{k}$$

$$= t_{2_x}\hat{i} + t_{2_y}\hat{j} + t_{2_z}\hat{k}$$

Assume the body is moving with a velocity $\vec{U}_b$, where:

$$\vec{U}_b = u_b\hat{i} + v_b\hat{j} + w_b\hat{k}$$

Then the body velocity in the normal direction is given by:

$$u_{b_n} = \vec{U}_b \cdot \vec{n}$$

$$= u_b n_x + v_b n_y + w_b n_z$$

Projecting the fluid velocity $\vec{U}$ on the body surface along the three orthogonal directions $\vec{n}$, $\vec{t}_1$, and $\vec{t}_2$ yields:

$$u_n = \vec{U} \cdot \vec{n}$$

$$= u n_x + v n_y + w n_z$$

$$u_{t_1} = \vec{V} \cdot \vec{t}_1$$

$$= u t_{1_x} + v t_{1_y} + w t_{1_z}$$

$$u_{t_2} = \vec{V} \cdot \vec{t}_2$$

$$= u t_{2_x} + v t_{2_y} + w t_{2_z}$$

Now, apply the Euler boundary condition:

$$u_n = u_{b_n} \qquad \text{(C-1)}$$

Interpolate the value of the velocity components in the other two directions from that of the next layer in the direction of the outward normal:

$$u_{t_1} = u_{t_1}\,|_{\pm} \qquad \text{(C-2)}$$

$$u_{t_2} = u_{t_2}\,|_{\pm} \qquad \text{(C-3)}$$

The ± sign indicates that, the interpolation will be done from either the next or previous layer according to the direction of the outward normal. For the directions posted in figure C-1, the

outward normal is running in the direction of increasing K, so the interpolation will be done from the surface $(K+1)$ and vice-versa.

Equations (C-1 to C-3) could be written in matrix form as follows:

$$\begin{bmatrix} n_x & n_y & n_z \\ t_{1_x} & t_{1_y} & t_{1_z} \\ t_{2_x} & t_{2_y} & t_{2_z} \end{bmatrix} \begin{pmatrix} u \\ v \\ w \end{pmatrix} = \begin{bmatrix} u_b n_x + v_b n_y + w_b n_z \\ t_{1_x} u_\pm + t_{1_y} v_\pm + t_{1_z} w_\pm \\ t_{2_x} u_\pm + t_{2_y} v_\pm + t_{2_z} w_\pm \end{bmatrix} \tag{C-4}$$

Equation (C-4) is a system of three linear determined algebraic equations, which can be easily solved by *Kramer's Rule*. Finally, the solution is given by:

$$u = u_{b_n}(t_{1_y} t_{2_z} - t_{1_z} t_{2_y}) - n_y(u_{t_{1\pm}} t_{2_z} - t_{1_z} u_{t_{2\pm}}) + n_z(u_{t_{1\pm}} t_{2_y} - t_{1_y} u_{t_{2\pm}})$$

$$v = n_x(u_{t_{1\pm}} t_{2_z} - t_{1_z} u_{t_{2\pm}}) - u_{b_n}(t_{1_x} t_{2_z} - t_{1_z} t_{2_x}) + n_z(u_{t_{2\pm}} t_{1_x} - t_{2_x} u_{t_{1\pm}})$$

$$w = n_x(u_{t_{2\pm}} t_{1_y} - t_{2_y} u_{t_{1\pm}}) - n_y(t_{1_x} u_{t_{z\pm}} - u_{t_{1\pm}} t_{2_x}) + u_{b_n}(t_{1_x} t_{2_y} - t_{1_y} t_{2_x})$$

Appendix D – Numerical Computation of the Aerodynamic Forces and Moments

Given an arbitrary body immersed in a fluid medium (figure D-1), the elementary force $d\vec{F}$ exerted on an element of the surface area $d\sigma$ is given by:

$$d\vec{F} = (\vec{n} \cdot \vec{\tau})\, d\sigma$$

Where:

$\vec{n}$ Denotes the outward normal to the surface.

$\vec{\tau}$ Denotes the stress tensor.

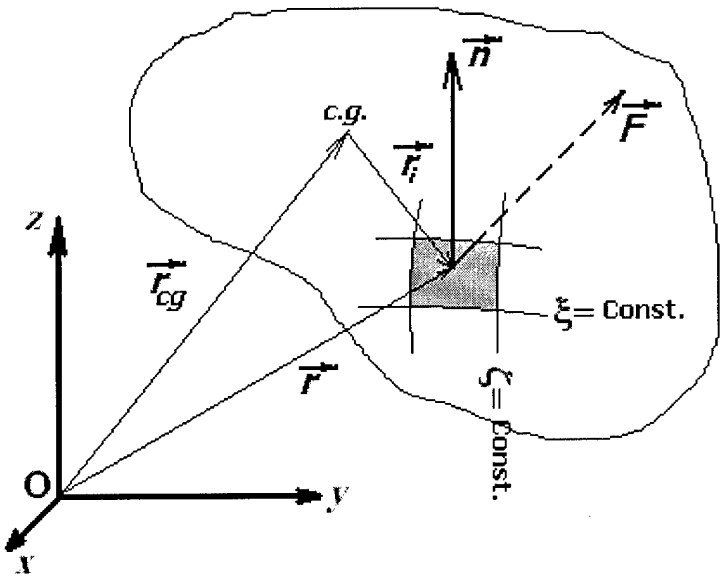

Figure D-1. Schematic drawing shows the nomenclature used.

Let the equation of the surface be given by:

$$f(x,y,z) = \eta(x,y,z) = c \qquad c \in I$$

Then by definition the normal vector $\vec{n}$ is given by:

$$\vec{n} = \frac{\nabla f}{|\nabla f|}$$

$$= \frac{\eta_x \hat{i} + \eta_y \hat{j} + \eta_z \hat{k}}{\sqrt{\eta_x^2 + \eta_y^2 + \eta_z^2}}$$

$$= \overline{\eta}_x \hat{i} + \overline{\eta}_y \hat{j} + \overline{\eta}_z \hat{k}$$

Where: $\hat{i}, \hat{j}, \textit{and } \hat{k}$ are unit vectors in the inertial frame of reference, and

$$\overline{\eta}_x = \frac{\eta_x}{\sqrt{\eta_x{}^2 + \eta_y{}^2 + \eta_z{}^2}}$$

$$\overline{\eta}_y = \frac{\eta_y}{\sqrt{\eta_x{}^2 + \eta_y{}^2 + \eta_z{}^2}}$$

$$\overline{\eta}_z = \frac{\eta_z}{\sqrt{\eta_x{}^2 + \eta_y{}^2 + \eta_z{}^2}}$$

Hence:

$$\vec{n} \cdot \vec{\tau} = \begin{bmatrix} \overline{\eta}_x & \overline{\eta}_y & \overline{\eta}_z \end{bmatrix} \begin{bmatrix} \tau_{xx} & \tau_{xy} & \tau_{xz} \\ \tau_{yx} & \tau_{yy} & \tau_{yz} \\ \tau_{zx} & \tau_{zy} & \tau_{zz} \end{bmatrix}$$

For the case of an inviscid fluid (Euler equations), all the off-diagonal elements of the stress tensor are zeros, leaving the diagonal elements, which are given as follows:

$$\tau_{xx} = \tau_{yy} = \tau_{zz} = -P$$

Hence:

$$d\vec{F} = -P \nabla \overline{\eta} \, d\sigma \qquad \text{(D-1)}$$

$$dF_x = -P \, \overline{\eta}_x \, d\sigma$$

$$dF_y = -P \, \overline{\eta}_y \, d\sigma$$

$$dF_z = -P \, \overline{\eta}_z \, d\sigma$$

Assume $d\vec{S}_1$ and $d\vec{S}_2$ are two arbitrary orthogonal curvilinear elements of arc length that bound the element of area $d\sigma$. For simplicity, let us pick $d\vec{S}_1$ along the line $\xi = \text{const.}$ and $d\vec{S}_2$ along the line $\zeta = \text{const.}$

In general, $$\left|d\vec{S}\right| = \sqrt{dx^2 + dy^2 + dz^2}$$

Also *dx, dy,* and *dz* could be written as:

$$dx = x_\xi d\xi + x_\eta d\eta + x_\zeta d\zeta$$

$$dy = y_\xi d\xi + y_\eta d\eta + y_\zeta d\zeta$$

$$dz = z_\xi d\xi + z_\eta d\eta + z_\zeta d\zeta$$

Substitute by $d\xi = 0$ on $d\vec{S}_1$ and $d\zeta = 0$ on $d\vec{S}_2$. Since $d\vec{S}_1$ and $d\vec{S}_2$ are bounding the element of area $d\sigma$, then $d\eta$ is also zero on $d\vec{S}_1$ and $d\vec{S}_2$.

$\Rightarrow$ $$\left|d\vec{S}_1\right| = \sqrt{\left(x_\zeta d\zeta\right)^2 + \left(y_\zeta d\zeta\right)^2 + \left(z_\zeta d\zeta\right)^2}$$

$$\left|d\vec{S}_2\right| = \sqrt{\left(x_\xi d\xi\right)^2 + \left(y_\xi d\xi\right)^2 + \left(z_\xi d\xi\right)^2}$$

By definition, $d\sigma$ is given by:

$$d\sigma = \left|d\vec{S}_1 \times d\vec{S}_2\right|$$

$$= \left\{\left|d\vec{S}_1\right|^2 \left|d\vec{S}_2\right|^2 - \left(d\vec{S}_1 \cdot d\vec{S}_2\right)^2\right\}^{\frac{1}{2}}$$

Factoring out the previous equation, and inserting the expressions for $d\vec{S}_1$ and $d\vec{S}_2$.

$\Rightarrow$ $$d\sigma = \left\{\left(x_\zeta y_\xi - x_\xi y_\zeta\right)^2 + \left(x_\zeta z_\xi - x_\xi z_\zeta\right)^2 + \left(y_\zeta z_\xi - y_\xi z_\zeta\right)^2\right\}^{\frac{1}{2}} d\xi d\zeta \qquad \text{(D-2)}$$

Recall the following metric relations:

$$\eta_x = J\left(y_\zeta z_\xi - y_\xi z_\zeta\right)$$

$$\eta_y = J\left(x_\xi z_\zeta - x_\zeta z_\xi\right)$$

$$\eta_z = J\left(x_\zeta y_\xi - x_\xi y_\zeta\right)$$

Where J is the Jacobian of the coordinate transformation at the grid point (ξ,η,ζ).

Insert the metric relations into (D-2), finally, $d\sigma$ is given by:

$$d\sigma = \sqrt{\eta_x^2 + \eta_y^2 + \eta_z^2}\ \frac{d\xi d\zeta}{J} \tag{D-3}$$

Inserting (D-3) into (D-1) yields:

$$d\vec{F} = -P\frac{\nabla\eta}{J}d\xi d\zeta$$

$\Rightarrow$

$$dF_x = -P\frac{\eta_x}{J}\,d\xi\,d\zeta$$

$$dF_y = -P\frac{\eta_y}{J}\,d\xi\,d\zeta$$

$$dF_z = -P\frac{\eta_z}{J}\,d\xi\,d\zeta$$

The differential force $d\vec{F}$ exerts a moment $d\vec{M}$ about the center of gravity, which is given by:

$$d\vec{M} = \vec{r}_i \times d\vec{F} \tag{D-4}$$

Where:

$\vec{r}_i$ Denotes the displacement vector from the c.g. to the surface area $d\sigma$.

$$\vec{r}_i = (x - x_{cg})\hat{i} + (y - y_{cg})\hat{j} + (z - z_{cg})\hat{k}$$

Inserting the expression for $\vec{r}_i$ in (D-4) and applying the cross product yields:

$$dM_x = (y - y_{cg})\,dF_z - (z - z_{cg})dF_y$$

$$dM_y = (z - z_{cg})\,dF_x - (x - x_{cg})dF_z$$

$$dM_z = (x - x_{cg})\,dF_y - (y - y_{cg})dF_x$$

Inserting the expressions for dF_x, dF_y, and dF_z yields:

$$dM_x = -\frac{P}{J}\left[(y - y_{cg})\eta_z - (z - z_{cg})\eta_y\right]d\xi\, d\zeta$$

$$dM_y = -\frac{P}{J}\left[(z - z_{cg})\eta_x - (x - x_{cg})\eta_z\right]d\xi\, d\zeta$$

$$dM_z = -\frac{P}{J}\left[(x - x_{cg})\eta_y - (y - y_{cg})\eta_x\right]d\xi\, d\zeta$$

Integrating over the whole surface yields the total forces and moments components, which are given respectively as follows:

$$F_x = -\iint P\frac{\eta_x}{J}\, d\xi\, d\zeta$$

$$F_y = -\iint P\frac{\eta_y}{J}\, d\xi\, d\zeta$$

$$F_z = -\iint P\frac{\eta_z}{J}\, d\xi\, d\zeta$$

$$M_x = -\iint \frac{P}{J}\left[(y - y_{cg})\eta_z - (z - z_{cg})\eta_y\right]d\xi\, d\zeta$$

$$M_y = -\iint \frac{P}{J}\left[(z - z_{cg})\eta_x - (x - x_{cg})\eta_z\right]d\xi\, d\zeta$$

$$M_z = -\iint \frac{P}{J}\left[(x - x_{cg})\eta_y - (y - y_{cg})\eta_x\right]d\xi\, d\zeta$$

Since the body-fixed x-axis is only translating (not rotating), then the rolling moment about the body-fixed x-axis (L_b) in equation (3-3) equals M_x.

REPORT DOCUMENTATION PAGE	Form Approved OMB No. 0704-0188

1. AGENCY USE ONLY *(Leave blank)*	2. REPORT DATE	3. REPORT TYPE AND DATES COVERED
	Aug. 2000	Doctoral Dissertation, Sep. 1996 - Aug. 2000

4. TITLE AND SUBTITLE
SIMULATION AND ANALYSIS OF WING ROCK PHYSICS FOR A GENERIC FIGHTER MODEL WITH THREE DEGREES-OF-FREEDOM

5. FUNDING NUMBERS

6. AUTHOR(S)
Ahmed A. Saad
Major, Egyptian Air Force

7. PERFORMING ORGANIZATION NAME(S) AND ADDRESS(ES)
Air Force Institute of Technology, Graduate School of Engineering and Mangement
2950 P Street, Building 640, WPAFB OH 45433-7765

8. PERFORMING ORGANIZATION REPORT NUMBER
AFIT/DS/ENY/00-01

9. SPONSORING/MONITORING AGENCY NAME(S) AND ADDRESS(ES)
N/A

10. SPONSORING/MONITORING AGENCY REPORT NUMBER

11. SUPPLEMENTARY NOTES
Prof. Brad S. Liebst
Head of the Department of Aeronautics and Astronautics
(937) 255-3636 ext. 4636

12a. DISTRIBUTION AVAILABILITY STATEMENT
APPROVED FOR PUBLIC RELEASE; DISTRIBUTION UNLIMITTED

12b. DISTRIBUTION CODE

13. ABSTRACT *(Maximum 200 words)*

Modern fighter designs have been associated with lateral self-excited oscillations known as "Wing Rock". Simulations of wing rock by flow visualization utilities have been encouraged to develop a complete understanding of the fluid mechanism that drives the motion as well as for prediction purposes. Previous wind/water tunnel simulations have been limited to a single degree-of-freedom (DoF) in roll. In this study, for the first time, wing rock is computationally simulated in three DoF: roll, sideslip, and vertical motion to study the effect of adding the sideslip and vertical motion. The results are for a generic fighter model consisting of a fore-body, a cropped delta wing, and a vertical fin. The effect of including the vertical fin is also studied. The interaction of aerodynamics and rigid-body dynamics during a single DoF wing rock for the wing-body configuration has been studied via snap shots of a cross-plane stagnation pressure distribution and tracing the instantaneous locations of vortex burst for an entire cycle of wing rock. The effect of adding the sideslip and vertical motion DoF to the simulations of the wing-body configuration was found to delay the onset and to reduce the amplitude of wing rock by about 50% with surprisingly no change in frequency. The wing rock simulation in three DoF was repeated for the full generic fighter model with the fin included. The aerodynamic effect of the fin was found to significantly delay the vortex burst on the upper surface of the wing. The net effect of the fin was found to augment the damping of the oscillations with significant increase in frequency.

14. SUBJECT TERMS
Aircraft Dynamics, Computational Fluid Dynamics, Fluid Dynamics, Angle of Attack
Aerodynamic Stability

15. NUMBER OF PAGES
115

16. PRICE CODE

17. SECURITY CLASSIFICATION OF REPORT	18. SECURITY CLASSIFICATION OF THIS PAGE	19. SECURITY CLASSIFICATION OF ABSTRACT	20. LIMITATION OF ABSTRACT
Unclassified	Unclassified	Unclassified	UL